UNIVERSITY MOHAMED BOUDIAF-M'SILA
FACULTY OF TECHNOLOGY
DEPARTMENT OF ELECTRONICS

1985
جامعة محمد بوضياف - المسيلة
Université Mohamed Boudiaf - M'sila

Serial number ………………..….

Registration number…. D.E/3C/03/15

THESIS

A dissertation Submitted for the degree of

DOCTORAT

Specialty: Electronics
Option: Microwaves and Telecommunications

THEME:

Modeling, Estimation and CFAR Detection in non-Gaussian Clutter

Modélisation, Estimation et Détection CFAR dans un Milieu de Clutter non-Gaussien

Presented by

Mrs: Gouri Amel

Supported **…/…/…**

Examining Committee Members:

President:	**Hocini Abdesslam**	**Professor**	**Univ. M'sila**
Supervisor:	**Mezache Amar**	**Professor**	**Univ. M'sila**
Co-supervisor:	**Oudira Houcine**	**Professor**	**Univ. M'sila**
Examiner:	**Khedrouche Djamel**	**Professor**	**Univ. M'sila**
Examiner:	**Atia Salim**	**Associate Professor**	**Univ. Bordj-Bou Arréridj**

- 2019/2020 -

Acknowledgments

Firstly, I thank Allah, the most high, for the opportunity he gave me to study, to research and to write this dissertation. Thank Allah, my outmost thanks, for giving me the ability, the strength, attitude and motivation through this research to complete this thesis.

I am very pleased to express my special gratitude and indebtedness to my supervisor, ***Prof. Amar Mezache*** *for accepting me as a doctorate student at the department of Electronics. I am sincerely grateful for his valuable guidance, genial criticism, wisdom and special endless patients in dealing with me throughout all these years. It is difficult to overstate my gratitude to him with his enthusiasm; his inspiration and his great effort make this approach easier. I have benefited greatly from his extensive technical knowledge and fatherly advices.*

I would like to thank and express my special gratitude to my Co-supervisor **Prof. Houcine Oudira** *for working with me and giving me the focus and the motivation to accomplish this work. I am grateful for his discussions of interest, his heartening words and his participation which has encouraged me and strengthened my spirit throughout this endeavor.*

I would like to thank **Prof . Abdesslam Hocini** *for being president of the examination committee. I also would like to thank my oral thesis committee members Prof.* **Djamel Khedrouche,** *Universsity of M'sila and* **Dr. Salim Atia** *from the University of Bordj-Bou Arréridj for accepting the examination of this thesis.*

I would like to extend my sincere thanks to all my colleagues, friends and the staff at the department of Electronics, university of M'sila for their help to accomplish this work, especially the LASS (Laboratoire Analyse des Signaux et des Systèmes) laboratory staff members .

I would like to thank the family **Zerougui** *for helping me all the years' student, thanks very much*

I am extremely grateful to my parents and my brothers and sisters whose their support and encouragement have been invaluable. I feel very lucky to be their daughter.

Finally and most importantly, I wish to express my deepest gratitude to my husband, **Abderrazak** *without whose support this work would not have been possible.*

AMEL

الملخص

في هذا العمل. تم استخدام نماذج غاوسي المركبة التي أنشئت بواسطة مكونات نسيج مختلفة لتمثيل زاوية حدوث فوضى البحر المنخفضة , يتم دمج النماذج المعروفة باسم **CGIG** و**K** و **pareto** type II لتكوين توزيعات مختلطة. بافتراض وجود ضوضاء حرارية ، يتم فحص تقريبي للنماذج المقترحة باستخدام بيانات **IPIX** الحقيقية التي يتم من خلالها استخدام خوارزمية نيلدر ميد للحصول على المعلمات غير المعروفة. يحتوي إجراء التقدير هذا على وقت حساب طويل، وقد أظهر ملائمة النتائج للبيانات التجريبية فعالية النماذج المركبة المقترحة مقارنة بالتوزيعات القياسية في معظم الحالات.

العمل الثاني الذي أنجز في هذه الأطروحة هو تطوير إجراءات تقدير جديدة ، وهي **HOME** و**CMLE** و **CNIOME**. لتقدير فوضى **CGIG** بالإضافة إلى معلمات الضوضاء. بالنسبة لـ **CNR** معروف وغير معروف ، تم استخدام طريقة **HOME** نظرًا لأنه يتم تقديم المقدرين الأخيرين كتكامل، يتم استخدام طريقة غوس التربيعية على أساس متعدد الحدود **Laguerre** و **Legendre** بعد تقسيم التكاملات إلى جزأين. من البيانات الحقيقية والمحاكاة ، يتم تقييم أداء التقدير للطرق المقترحة من حيث **CNR** . في حالة **CNR** معروف، فقد تبين أن طرق **HOME** و**CMLE** يمكن أن تنتج تقديرات معلمة الشكل مماثلة لعدد كبير من العينات(**M**). بالنسبة لـ **CNR** غير معروف, تقدم أساليب **CMLE** و **CNIOME** نتائج تقريبية. تعرض طريقة **HOME** نتائج سيئة لجميع قيم معلمة الشكل. عندما يكون عدد النبضات و **CNR** مرتفع، تقدم طريقة **CMLE** نتائج أفضل مقارنة بالنهج الأخرى

تم استخدام كاشفات **CFAR** حدودي وغير حدودي لفوضى توزيع ويبل. يتم قياس أداء خوارزميات **CFAR** هذه في البيئات المتجانسة وغير المتجانسة. تحسين أداء الكشف من حيث استهلاك الوقت المنخفض هو أمر مهم جدًا في تطبيقات الوقت الفعلي. لهذا الغرض ، يتم استخدام المقدر بناءً على إحصاء **ZLog(z)** لاكتشاف **CFAR** في حالة فوضى ويبل، يتم الحصول على طريقة التقدير هذه كدالة لوظيفة **digamma** .مقدر لحظة الترتيب غير الصحيح، يتم أيضًا تقديمه ويتزامن مع نتائج التقدير **ZLog(z)** للقيم المنخفضة للترتيب الكسر للحظة. باستخدام اختبار نيمان بيرسون، تم إجراء مقارنات للكشف عن **CFAR** بناءً على المقدر المقترح وكاشفات **Logt-CFAR** و **ML-CFAR** الحالية.

Abstract

Compound Gaussian (CG) models with different texture components have been utilized to describe sea clutter statistics at low grazing angles. In the first work, the well-known *K*, Pareto type II and compound Gaussian inverse Gaussian (CGIG) models are combined firstly to produce mixture distributions with thermal noise. Using Intelligent Pixel Processing (IPIX) real data, the fitting of the proposed models are investigated where a simplex algorithm based on the Nelder-Mead algorithm is used to achieve the unknown parameters from the data. Regardless of heavy computation time, fitting results to empirical data showed the efficiency of the proposed mixtures models against the standard distributions in several cases.

The second work considered in this thesis is the development of new estimation procedures labeled higher order moments estimator (HOME), constrained non-integer order moments estimator (CNIOME) and constrained maximum likelihood estimation (CMLE) for parameter estimation of CGIC clutter plus noise. The HOME method is given in a closed-form for both known and unknown clutter-to-noise ratio (CNR). As the last two estimators are given in integral forms, the Gauss quadrature method based on Legendre and Laguerre polynomials is used after splitting the underlying integrals into two parts. Using simulated and real data, estimation performances of the proposed methods are assessed in terms of known and unknown clutter to noise ratio. In the case of known *CNR*, it is shown that the HOME and the CMLE methods can produce similar estimates of the shape parameter at high sample sizes. For unknown *CNR*, both CNIOME and CMLE methods present approximate results. Moreover, the HOME exhibits poor estimation results for all values of the shape parameter. When the number of integrated pulses and *CNR* values are high, the CMLE method outperforms always the CNIOME and the HOME methods.

In radar target detection, parametric and non-parametric Constant False Alarm Rate (CFAR) detectors for Weibull distributed clutter have been suggested achieving the full CFAR property. The performances of these CFAR algorithms are measured by CFAR loss in homogeneous and heterogeneous environments. The improvement of detection performances in terms of low time-consuming which is very important in real time applications is also considered. To this effect, the zlog(z) based estimator for CFAR detection in homogeneous Weibull clutter is used. This estimation method is obtained in terms of the digamma function where the estimates of the shape parameter are determined by the interpolation tool. The non-integer order moments estimator (NIOME) is also given and coincides the zlog(z) estimation results for low values of the moment's fractional order. Based on the Neyman-Pearson type test, CFAR detection comparisons, based on the proposed estimator and the existing logt-CFAR and maximum likelihood CFAR (ML-CFAR) detectors, are conducted.

Résumé

Les modèles Gaussiens composés construits par diverses composantes de texture ont été utilisés pour représenter les statistiques du clutter de mer à faibles angles d'incidence. Dans ce cas, les modèles connus sous les noms *K*, Pareto type II et CGIG sont combinés pour former des distributions mélangées. En supposant la présence du bruit thermique, l'approximation des modèles proposés est examinée à l'aide des données réelles IPIX où l'algorithme de Nelder-Mead est utilisé pour obtenir les paramètres inconnus. Cette procédure d'estimation possède un temps de calcul important et l'ajustement des résultats aux données empiriques a montré l'efficacité des modèles composés proposés par rapport aux distributions standards dans la plupart des cas.

Le deuxième travail considéré dans cette thèse est le développement de nouvelles procédures d'estimation, à savoir HOME, CNIOME et CMLE, pour l'estimation des paramètres du clutter CGIC plus bruit. Pour un CNR connu et inconnu, l'expression compacte de la méthode HOME a été trouvée. Comme les deux derniers estimateurs sont présentés sous forme d'intégrales, la méthode de Gauss quadratique basée sur les polynômes de Legendre et Laguerre est utilisée après la division des intégrales en deux parties. A partir des données réelles et simulées, les performances d'estimation des méthodes proposées sont évaluées en termes du CNR. Dans le cas du CNR connu, il a été montré que les méthodes HOME et CMLE peuvent produire des estimés du paramètre de forme similaires pour un nombre d'échantillons élevé. Pour un CNR inconnu, les méthodes CNIOME et CMLE présentent des résultats approximatifs. La méthode HOME présente de mauvais résultats pour toutes les valeurs du paramètre de forme. Lorsque le nombre d'impulsions et le CNR sont élevés, la méthode CMLE offre de meilleurs résultats par rapport aux autres approches.

Les détecteurs paramétriques et non paramétriques CFAR ont été utilisés pour un clutter de distribution de Weibull. Les performances de ces algorithmes CFAR sont mesurées par la perte CFAR dans des environnements homogènes et hétérogènes. L'amélioration des performances de détection en termes de faible consommation de temps qui est très importante dans les applications en temps réel est également envisagée. À cet effet, l'estimateur basé sur la statistique zlog (z) pour la détection CFAR dans le cas du clutter Weibull homogène est utilisé. Cette méthode d'estimation est obtenue en fonction de la fonction digamma où les estimations du paramètre de forme sont déterminées par l'outil d'interpolation. L'estimateur NIOME est également donné et coïncide avec les résultats d'estimation zlog (z) pour les faibles valeurs de l'ordre fractionnaire du moment. A l'aide du test de Neyman-Pearson, des comparaisons de détection CFAR basées sur l'estimateur proposé et les détecteurs logt-CFAR et ML-CFAR existants ont été effectuées.

Contents

Chapter I : Radar Overview

Chapter II : Clutter Modeling using Mixtures of Compound Gaussian Models

Chapter III : Estimators of CGIG Clutter plus Noise Parameters

Chapter IV : Radar CFAR Detection in Weibull Clutter based on zlog (z) Estimator

List of Figures

Chapter I:

Chapter II:

Chapter III:

Chapter IV:

List of Tables

Chapter I:

Chapter II:

Chapter III:

Chapter IV:

Table of Abbreviations

CFAR	Constant False Alarm Rate
CNR	Clutter-to-Noise Ratio
CUT	Cell Under Test
CGIG	Compound Gaussian Inverse Gaussian
CIG	Inverse Compound Gaussian
CDF	Cumulative Distributed Function
CCDF	Complementary CDF
CG	Compound Gaussian
CCR	Clutter-to-Clutter Ratio
CNIOME	constrained non-integer order moments estimator
CA-CFAR	Cell-Averaging CFAR
CMLD-CFAR	Censored-Mean-Level CFAR
EM	Electromagnetic
FOME	Fractional Order Moments Estimator
GP	Generalized Pareto
$G\Gamma$	Generalized gamma
GM-CFAR	Geometric Mean CFAR
GO-CFAR	Greatest-Of CFAR
GC	Generalized Compound
HOME	Higher Order Moments Estimator
IPIX	Intelligent PIxel processing X-band
IF	Intermediate Frequency
ICR	Interfering-to-Clutter Ratio
IID	Identically and Independent Distributed
LLF	Log-Likelihood Function
MSE	Mean Square Error
MLE	Maximum Likelihood Estimate
N-M	Nelder-Mead
NIOM	Non-Integer Order Moments
N-P	Neyman-Pearson
OS-CFAR	Order Statistics CFAR

PCFE	Parametric Curve Fitting Estimation
PDF	Probability Density Function
P_{FA}	Probability of False Alarm
P_D	Probability of Detection
RADAR	RAdio Detection And Ranging
RCS	Radar Cross Section
RF	Radio Frequency
STC	Sensitivity time control
SNR	Signal-to-Noise Ratio
SCR	Signal-to-Clutter Ratio
SO-CFAR	Smallest-Of CFAR

Table of Symbols

Chapter I

P_{Di}	Power density of a wave incident
R	Range
σ	Target cross section
P_{Dr}	Power density of the scattered waves at the receiving antenna.
P_t	Peak transmitted power
G	Antenna gain
A_e	Antenna effective aperture
λ	Wavelength
ρ	Aperture efficiency
S_{min}	Minimum detectable signal power
R_{max}	Maximum radar range
A_c	Clutter area
σ_c	Average clutter RCS
σ_t	Target RCS
σ^0	Clutter scattering coefficient
ψ_g	Grazing angle
θ_{3dB}	Beam width
c	Scale parameter of the K-distribution
ν	Shape parameter of the K-distribution
α	Shape parameter of the Pareto type 2 distribution
β	Scale parameter of the Pareto type 2 distribution
a	Scale parameter of the GC distribution
$\nu_{1,2}$	Shape parameters of the GC distribution
$b_{1,2}$	Power parameters of the generalized gamma ($G\Gamma$)
$K_{\nu\text{-}1}(2cx)$	Modified Bessel function
m_s	Average cross section
S	Ratio of the power
Z	Observation space
H_0, H_1	Binary Hypothesis
$\Re$	Average cost
σ^0	Grazing angle minimal

μ	Median
σ	Standard deviation
P_F	Probabilities of false alarm
P_D	Probabilities of detection
P_M	Probability of miss
$P(H_0), P(H_1)$	A priori probabilities
a	Power of signal
b	Power of clutter
α	Scale factor
U	Sums of the outputs of the leading cells
V	Sums of the outputs of lagging cells
T	Detection threshold
p_n	Noise power
$\Gamma(.)$	Gamma function

Chapter II

ν	Shape parameter of the *K* distribution
b	Scale parameter of the *K* distribution
α	Shape parameter of the Pareto plus noise distribution
b	Scale parameter of the Pareto plus noise distribution
λ	Shape parameter of the inverse Gaussian distribution
μ	Mean power of the inverse Gaussian distribution
${}_2F_0(.,.;.;.)$	Hypergeometric function
r	Moment's order
θ	Vector of unknown parameters
k	Weighting factor

Chapter III

p_n	Noise power
σ^2	Variance
μ	Clutter power of inverse Gaussian distribution
λ	Shape parameter of inverse Gaussian distribution
N	Number of integrated pulses
$p_Z(z \mid p_n, N)$	PDF for multilook case

h	Distance
$w(x)$	Weight function
$L_n(x)$	Laguerre Polynomials
$H_n(x)$	Hermite Polynomials
$T_n(x)$	Chebyshev Polynomials
$P_n(x)$	Legendre Polynomials
R_n.	Error term of Gauss quadrature
$\hat{\lambda}$	Estimated shape parameter
λ_{eff}	Effective shape parameter.
M	Number of samples
$\hat{\mu}$	Estimated mean power

Chapter IV

b	Scale parameter of weibull distribution
c	Shape parameter of weibull distribution
r	Order moment
$\langle . \rangle$	Expectation
$\psi(.)$	Psi function
$\hat{\mu}$	The clutter mean estimate
$\hat{\sigma}$	the standard deviation
P_{FA}	Probabilities of false alarm
P_D	Probabilities of detection
α	The scale factor

Published Works

Articles:

1. **A. Gouri** , A. Mezache and H. Oudira, “Radar CFAR detection in Weibull clutter based on zlog(z) estimator“, Remote Sensing Letters, Taylor & Francis, Vol. 11, no. 6, pp. 581-586, 2020.
2. A. Mezache, **A. Gouri** and H. Oudira, “ Parameter estimation of CGIG clutter plus noise using constrained NIOME and MLE approaches“, IET Radar, Sonar & Navigation, Vol. 12, no. 2, pp. 176-185, 2018.
3. H. Oudira, **A. Gouri** and A. Mezache , “ Optimization of Distributed CFAR Detection using Grey Wolf Algorithm”, Procedia Computer Science, Elsevier, Vol. 158, pp. 74-83, 2019.
4. **A. Gouri**, A. Mezache, H. Oudira, “Distributed CA-CFAR and OS-CFAR Detectors Mentored by Biogeography Based Optimization Tool”, International Journal of Information Science & Technology (IJIST), Vol. 3, no. 3, pp. 20-29, 2019.

Conferences:

1. **A. Gouri**, A. Mezache and H. Oudira,” The performance of Decentralized CFAR Detection using Biogeography Based Optimization”, 5th IEEE CiSt (OMCM), 20-24 October, 2018, Marrakech-Morocco.
2. **A. Gouri**, A. Mezache, H. Oudira and A. Bentoumi, ‘Mixture of compound-Gaussian distributions for radar sea-clutter modeling’, 4th International Conference on Control Engineering & Information Technology (CEIT), December 16-18, Hammamet-Tunisia.
3. A. Mezache, **A Gouri** and H. Oudira, “Sea clutter modeling comparisons using compound Gaussian distributions with noise”, 2nd International Conference on Pure & Applied Science, June 1-5, 2016, Istanbul-Turkey.

1. Introduction

A RADAR (**RA**dio **D**etection **A**nd **R**anging) is an electrical system that transmits radiofrequency (RF) electromagnetic (EM) waves toward a region of interest and receives and detects these EM waves when reflected from objects in that region. The details of a radar system vary from one to another; the major subsystems must include a transmitter, an antenna, a receiver, and a signal processor. The system may be significantly simpler or more complex. Originally developed to detect enemy aircraft during World War II, radar has through the years shown diverse applications, not just for military consumers, but also for commercial customers. Radar systems are still used to detect enemy aircraft, but they also keep commercial air routes safe, detect speeding vehicles on highways, image polar ice caps, assess deforestation in rain forests from satellite platforms, and image objects under foliage or behind walls [1].

The purpose of radar signal processing is to extract desired data from radar signals. The desired data usually concerns the detection of a target of interest, the location of the target in space about the radar, the time rate of change of the target's location in space and, in some cases, the identification of the target as being a particular one of a number of classes of targets [2]. The problems of radar clutter have been discussed in all the basic radar texts, and remain the subject of extensive current research. Interest in clutter is almost universal in radar because most of the echo signals received by radar originate not from the desired target but from surrounding objects or surfaces which tends to mask the target signal [3]. In target detection systems (e.g. radar), the effects of interfering signals (clutter) from the environment are usually partially unknown and/or varying in terms of their statistical properties. In such instances, where the performance of the optimal detector deteriorates significantly, CFAR detectors can be used since they are insensitive to changes in the underlying statistics of the clutter. Statistical decision theory used in such fields as radar, sonar, digital communication and ultrasonic imaging, attempts to discriminate between information bearing signals and noise or interference [4]. In recent years, general compound and compound Gaussian distributions have been utilized extensively to fit sea and land clutter. In target detection context, the main objective of radar researchers is to select the best statistical clutter model with consistent estimation of its parameters and robust CFAR detectors.

2. State of the art.

Generally the radar applications are related to the three research topics as mentioned in the following subsections:

(i) Clutter modeling:

In radar systems with low resolution capabilities, the intensity statistics of the sea echoes have been found to be described by the exponential or Rayleigh (i.e., Gaussian clutter case) probability density function (PDF). With the development of radar technologies operating at low grazing angles, the resolutions of sea clutter statistics have been greatly reduced and have been observed to deviate from Gaussianity [5]. Nowadays, CG distributions with and without thermal (system) noise are commonly used to fit high-resolution sea echoes and are the basis of the construction of most target detection schemes [6]. The CG models are formed by two components; the speckle component and the texture component that is also termed by the modulation component. The gamma, the inverse gamma and the inverse Gaussian distributed texture components were used to obtain the *K*, the generalized Pareto (GP) and the CGIG PDFs respectively [7, 8]. The difference between the CG models with and without noise is that the clutter power levels can be affected by an additional amount of noise in the speckle component which is referred to as CNR. CG models plus noise have been effectively tested to fit the IPIX radar lake-clutter measurements in order to attaint better goodness-of-fit against the conventional Rayleigh, Weibull, log-normal and *K* PDFs [9, 10].

To give more fitting precision to empirical (real) data, the mixture of two distributions have been considered in the open literature [11, 12]. In this context, Rosenberg *et al* [11] applied the KK distribution for the analysis of the Ingara data collected at medium to high grazing angles. The model is generalized to account the integration of multiple looks and a thermal noise component to produce greater accuracy of the underlying shape of the fitted PDF. Moreover, the required detection threshold to achieve a CFAR property was studied and compared to case of *K*-distributed clutter. Abraham *et al* [12] proposed a mixture of Rayleigh and *K* PDFs for representing active sonar data comprising clutter sparsely observed in a Rayleigh-distributed background. The *K*-Rayleigh mixture model was seen to provide improved PDF fits and inference on the clutter statistics. A parameter estimation technique based on the expectation maximization (EM) algorithm is proposed and shown to perform adequately [12]. Zhou *et al* [13] proposed an alternative statistical model, which is a mixture of

K-distribution and log-normal distribution for modeling the SAR (synthetic aperture radar) data. This mixture model is able to model the clutter data, the target data, or the mixed data of clutter and target.

(ii) Parameter estimation:

In real life radar applications, most of target detectors can not carry out without parameter estimation of clutter models. During the past two decades, a great deal of attention has been focused on the problem of parameter estimation of CG models with and without noise. Methods based on maximum likelihood (ML), HOME, NIOM and [zlog(z)] were commonly used for the shape parameter estimates of CG models [9-16]. Practical use of the HOME method for *K* clutter plus noise parameters is limited by the number of the data to be processed [15]. To improve the estimation precision with small sample sizes, asymptotic expression of NIMOE method is derived in terms of confluent hypergeometric functions [16]. The use of this formula with positive and negative order moments leads to closed-form estimator of the shape parameter [14]. Such estimator is advantageous in single look data and gives approximate results compared to the numerical [zlog(z)] based approach obtained in a previous work [72]. To obtain a good characterization of observed samples, the speckle and the texture components are both modeled by two generalized gamma distributions with different parameters values [17]. Here, parameters are estimated by matching theoretical moments with the data and parametric curve fitting estimation (PCFE) methods. An approximate method for calculating the PDF of the amplitude of the sum of Weibull distributed radar clutter and thermal noise is derived in [18]. The impact of considering Rayleigh clutter plus noise in the speckle component of the *K* distribution to correctly model the radar backscatter is studied at high grazing angles [19]. The *K* plus Rayleigh model contains an additional parameter and methods based on moments and least squares are used for parameter estimation. On the other hand, NIOME, [zlog(z)] and CMLE approaches are developed for Pareto clutter plus noise parameters [20, 21]. In terms of accuracy, the CMLE approach showed a slight superiority compared to the [zlog(z)] method, but the computing time is relatively high due to the optimization of likelihood functions. When CGIG clutter plus noise is considered, the PCFE method is utilized to find the unknown parameters [22]. Ollila *et al* [9] presented the ML estimate for tail fitting comparisons of the CGIG model with the fitted *K* and *t*-distributions. The form of NIOME, [zlog(z)] and MLE estimators of CGIG distribution parameters are derived in terms of Bessel and exponential-integral functions [23]. In [24], low-order moment-based estimation is proposed using the first two moments to obtain a higher precision estimator and a look-up table method is employed to overcome the lack of an analytical expression of the shape parameter. An iterative ML and outlier-robust bi-percentile estimators are derived and compared to the standard moment-based estimator [25].

***(iii) CFAR detection*:**

CFAR detectors have been utilized in radar systems where the clutter environment is partially unknown and/or has varying statistical properties (e.g., power,…etc). ln such instances, the performance of a fixed optimal detector deteriorates significantly, and nonparametric CFAR detectors ra designed to be invariant to changes in the clutter PDF. An effective method of accomplishing this is to use local estimates for the threshold from a set of known noise or clutter samples related to the unknown (or varying) parameters of the clutter distribution. However, the problem arises where the known noise samples contains target information which will significantly degrade the probability of detection. In an automatic radar detection system, resolution cells range are used to estimate the background level and a threshold is then formed to test for the presence of a target in the cell under test (CUT). Centralized and decentralized CFAR detectors operating in homogeneous and heterogeneous clutter are developed in terms of different test statistics. For instance, the cell averaging CFAR (CA-CFAR), the ML-CFAR, the logt-CFAR and the geometric mean CFAR (GM-CFAR) algorithms are all suited when the clutter is independent and identically distributed (iid) in the reference window [26-29]. In the realistic case when interfering targets and/or clutter edge situations are present, CFAR procedures based on the censoring of cells resolution contents like the order statistic CFAR (OS-CFAR), censored mean level CFAR (CMLD-CFAR), censored maximum likelihood CFAR (CML-CFAR) and Weber-Hykin CFAR (WH-CFAR) processors have been utilized to obtain robust estimates of the threshold in the presence of inhomogeneous clutter observations for exponential clutter distributions [32-35]. These techniques, however, do not fully utilize the priori information related to the clutter distribution resulting in degradation in the probability of detection. Furthermore, the study of OS-based threshold estimators designed under the CFAR constraint is applicable to other clutter distributions [4].

In the past, radar clutter amplitude has been described using Rayleigh model assumptions. However, as the size of the resolution cell of the radar decreases, the clutter distribution develops a larger tail than the Rayleigh distribution. The log-normal distribution is the simplest and has been proposed before as a model for sea clutter [30]. The most successful and best known of which is the *K*- distribution, but the Weibull has also been widely used in data analysis of radar clutter [31]. In radar target detection, parametric and non-parametric CFAR detectors for Weibull distributed clutter have been suggested achieving the full CFAR property [32-35]. The performances of these CFAR algorithms are measured by CFAR loss in homogeneous and heterogeneous environments. The adaptive threshold was effectively based on the estimation of the scale parameter and the shape parameter, using either moments or order statistics [32]**.** Both techniques exhibit extensive CFAR loss**.** It has also been demonstrated that the loss is related to the variance of the estimated parameters**.** The well known logt-CFAR detector has been developed for Weibull better than the log-normal clutter [33]. The test statistic is independent on clutter parameters and is suited for iid clutter samples. In order to improve the CFAR loss due to the presence of interfering targets in Weibull background, the WH-CFAR (Weber/hykin) detector is formed by dual order statistics [34]. Under the assumption of scale and power invariant distributions, Weinberg *et al* derived recently new non-coherent CFAR processes operating in homogeneous and non-homogeneous situations [35]. Here, the so-called GMOS-CFAR (Geometric Mean Order Statistic CFAR), TMOS-CFAR (Trimmed MOS CFAR) and IE-CFAR (Inclusion/Exclusion CFAR) detectors achieve the full CFAR property which is acquired without the requirements of the estimates of the clutter parameters through secondary data.

3. Contributions

The objective of this thesis is highlighted by presenting the summary of our contributions that are treated in the three outfits.

(i) Clutter modeling:

The first contribution in this work concerns the modelling of sea radar clutter using a mixture of two compound Gaussian distributions plus thermal noise. The speckle component of the proposed models is formed by an exponential distribution while the texture component is particularly modelled by means of two different distributions [36]. The work presented in [36] is extended here to account three types of mixture models which are compared to the standard *K*, GP and KK clutter plus noise models. To do this, the gamma, the inverse gamma and the inverse Gaussian distributions are considered to describe the modulation components. The proposed models are analysed and the non-linear least squares curve fitting technique based on the N-M algorithm [37] is employed to obtain optimal parameters estimates.

Compared to the existing KK, *K*, and Pareto clutter plus noise distributions, experimental results show that the proposed mixture models with different random textures are well suited to fit high resolution sea clutter data IPIX ((Intelligent PIxel processing X-band)) in several cases.

***(ii) Parameter estimation*:**

Concerning the second contribution, estimators based on HOME, NIOME and MLE methods presented in [23] are extended in this work for CGIG clutter plus noise parameters. In doing this, the compact expression of HOME is derived firstly. As the closed-form of NIOM is quite difficult to obtain, numerical integration based on 'Legendre' and 'Laguerre' polynomials of Gauss quadrature method is employed. This approach is referred to as CNIOME method. By means of the first two intensity moments, a CMLE is constructed by minimizing the negative log likelihood function in one variable to find the shape parameter. For comparison purposes, computer simulations are presented with known and unknown *CNR*. In the case of known *CNR*, the method of moments provides a good fit as compared to the NIOME and the CMLE methods. For unknown *CNR*, the HOME provides a rapid calculation but less accurate than the others. The CNIOME method requires numerical optimization for the shape parameter and is somewhat fast to compute. In most cases, the CMLE approach is accurate, but relatively slow due to the calculation of the numerical integration of log likelihood functions.

(iii) CFAR detection:

The third contribution presented in this dissertation focuses on the improvement of CFAR detection performance in Weibull clutter in terms of low time-consuming which is very important in real time applications. To this effect, the zlog(z) based estimator for CFAR detection in homogeneous Weibull clutter is used. This estimation method is obtained in terms of the digamma function where the estimates of the shape parameter are determined by the interpolation tool. NIOME is also given and coincides the zlog(z) estimation results for low values of the moment's fractional order. Based on the Neyman-Pearson type test, CFAR detection comparisons based on the proposed estimator and the existing logt-CFAR and ML-CFAR detectors are conducted.

4. Thesis Organization

The present thesis is structured in the following manner:

Chapter 1 presents firstly the different elements of monostatic radar system as well as radar cross section and radar equation. Then, two types of radar clutter (surface clutter and volume clutter) are discussed and numerous statistical models representing high resolution radar echoes are given. Next, target models proposed in the open literature are present where classical binary decision criteria and some standard CFAR detectors, used for homogeneous and heterogeneous environments, are described at the end of this chapter.

Chapter 2 recalls the expressions of *K*, Pareto type II and CGIG clutter plus noise PDFs. Mixture PDFs and Complementary Cumulative Distributed Functions (CCDFs) formed by these distributions with thermal noise are given and the flowchart of the N-M algorithm is presented for estimating respective parameters. Then, modeling performances of the proposed mixture models against the three *K*, GP and *KK* distributions plus noise are investigated by means of IPIX real data with different cell resolutions.

Chapter 3 presents initially the expression of moments of CGIG clutter plus noise PDF in terms of the Bessel function. Then, mathematical stages for the derivation of HOME, CNIOME and CMLE based estimators of CGIG clutter plus noise parameters are given for iid samples. Both simulated and IPIX real data are examined to assess estimation performances of the above underlying methods.

Chapter 4 develops firstly the zlog(z) based estimator for CFAR detection in Weibull clutter. This estimation method is obtained in terms of the digamma function where the estimates of the shape parameter are determined by the interpolation tool. NIOME is also given and coincides the zlog(z) estimation results for low values of the moment's fractional order. Swerling I target CFAR detection performances based on the zlog(z) estimator are compared with those obtained by existing ML CFAR detector.

Finally, main conclusions made in this work are reported. Some perspectives concerning the extension of this research work are outlined in the future.

Chapter I

1

Radar Overview

Chapter outline:

I.1 Introduction

Radar is placed among its surroundings in space, it sends, receives, and processes signals in time. These signals are described by their spectra and statistical distributions. Hence, radar is a detection system that uses radio waves to determine the range, angle, and/ or velocity of objects. It can be used to detect aircraft, ships, spacecraft, guided missiles, motor vehicles, weather formations, and terrain.

A radar system consists of a transmitter producing electromagnetic waves in the radio or microwaves domain, a transmitting antenna, a receiving antenna (often the same antenna is used for transmitting and receiving), a receiver and processor to determine properties of the objects. Radio waves (pulsed or continuous) from the transmitter reflect off the object and return to the receiver, giving information about the object's location and speed. Radar was developed secretly for military use by several nations in the period before and during World War II. A key development was the cavity magnetron in the UK, which allowed the creation of relatively small systems with sub-meter resolution [38].

This chapter is organized as follows. Section I.2 presents different elements of monostatic radar system where radar cross section and radar equation that provide the maximum range are also given. Section I.3 describes the two types of radar clutter (i.e., surface clutter and volume clutter) and then presents statistical models characterizing low and high resolution radar echoes. Section I.4 outlines target models found in the open literature. Section I.5 summarizes classical binary decision criteria. Section I.6 describes some CFAR detectors used for homogeneous and heterogeneous environments. Finally, a conclusion is drawn in Section I.7.

I.2 Radar Systems

As discussed earlier, radar is an object-detection system that uses radio waves to determine the range, angle, or velocity of objects.

I.2.1 Main monostatic radar components

A typical arrangement of stages for a basic monostatic radar is shown in Figure I. 1. The radar timing is contained in the coherent oscillator and trigger generator box. The coherent oscillator provides the phase reference for the radar and the basic timing clock [1, 39]. Radar components cover a wide range of sizes and use a number of different special techniques so that they are normally developed by specialists in their own field.

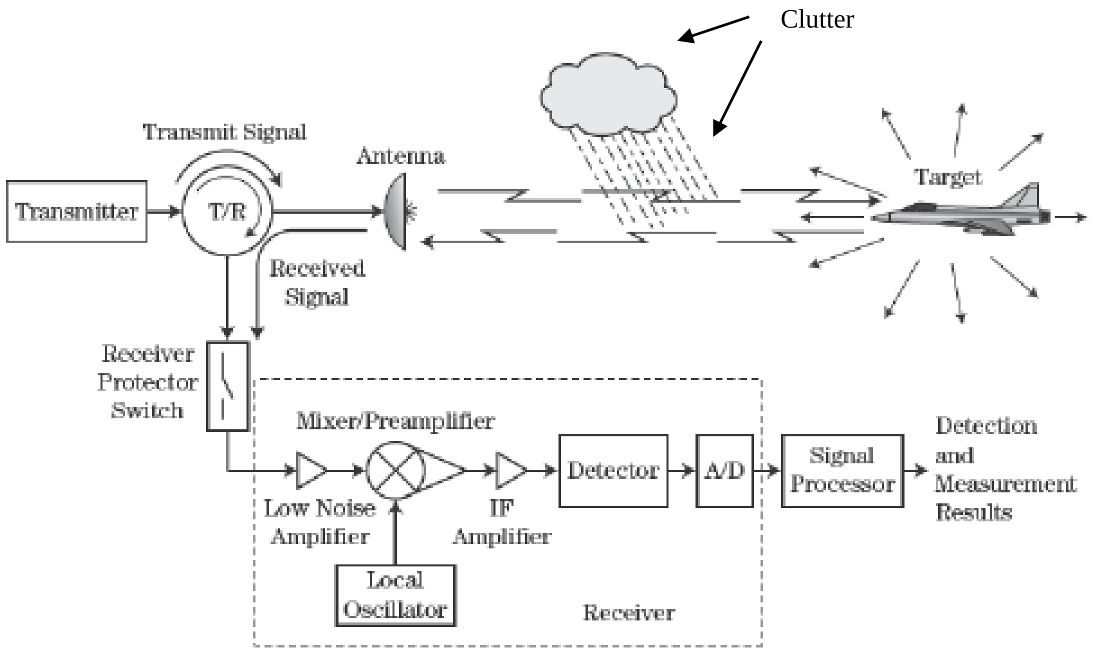

Figure I.1: Major elements of the radar transmission/reception process [1]

A number of common factors must be observed throughout the design of radar, such as the avoidance of signal distortion, which requires a wide dynamic range, and the best arrangement of the stages using the components at hand. As long as no signals are distorted or suppressed, linear signal processing may take place in any order, and the processes used in analogue processing (mostly at intermediate frequency), and digital processing (digital representations of a two-phase video signal) are equivalent [1, 2, 39].

- Transmitter: The transmitter converts mains power into radio frequency power, which leaves the radar by the antenna to illuminate its surroundings in the same way as a searchlight. The waveguide or transmission line system connects the transmitters and receivers to a common antenna.

- Antenna: The antenna directs the transmitter energy into a beam that illuminates the radar's surroundings. The echoes of the illumination are gathered by the antenna for the receivers. The antenna is the principal filter to attenuate signals (interference or jamming) coming from other directions. Once the radio frequency energy leaves the antenna, it is subject to atmospheric refraction and attenuation.

- Receiver: The receiver is normally a super heterodyne receiver with one or more intermediate frequencies. The first stage of the receiver is the principal component that defines the noise level and thus the sensitivity of the radar. The signals that arrive at the signal processor must not be distorted so they may be separated into the original components without the distortion components. The use of sensitivity time control (STC) reduces the necessity for a very wide dynamic in the receiver circuits. The matched filter has a shape and a bandwidth that gives best selection of signal energy out of the mixture of signals and noise coming from the receiver. These filters are often difficult to produce, so commonly simpler filters are used, called matching filters.

- Detector: The intermediate frequency signals need to be detected before they can be displayed. Simpler detectors reject either phase or amplitude information and change the statistics of the thermal noise on a theoretical carrier from the receiver. Coherent signal processors, which follow detectors, require the full amplitude and phase information in the echo signals. This information is preserved in vector detectors. The most common detector circuit is a synchronous detector that develops the in-phase (I) component of the vector and the quadrature (Q) phase component.

- Analogue-to-digital converter: Digital signal processors perform arithmetic on trains of binary numbers that represent the signals. Analogue to digital converters convert the signals, normally from a vector detector, to digital form. The side effects are the limiting of the dynamic range, quantization noise, and distortion. Even in more modern systems in which the signal is sampled at the intermediate frequency (IF) with a single analog-to-digital converter (ADC), an algorithm implemented in the system firmware constructs the I and Q components of the signal for processing the envelop, $V = \sqrt{I^2 + Q^2}$.

- Signal processor: Signal processing may take place during one sweep, many sweeps, and many scans. Radar echoes are a mixture of wanted echoes (for example, aircraft) and clutter echoes (often from land, sea, weather, or birds), which are generally of no interest. Signal processing tries to filter the echoes for the user and match them to his display. Modern digital processing often causes the echoes to be displayed as synthetic shapes that show only the information for which it has been preprogrammed. In contrast, radar operators who use older equipment are used to identifying echoes by size, shape, and movement. The evaluation of these criteria takes time and greatly reduces the number of echoes that an operator may follow, but it may be critical in unusual or unforeseen situations.

- Detection and measurement results: After the signals have been filtered to exclude out-of-band noise, the pulse has been compressed (when necessary), and the clutter and interference have been reduced to the noise level, a decision is made as to whether the echo signal represents an object of interest. The decision may be made automatically or by an operator. Once the echo signals have been detected, the position, radial velocity and classification of the object must be estimated. The echo signals are combined with noise and the measurement accuracy depends on the signal-to-noise ratio (SNR) [39].

I.2.2 Radar classification

The concept of radar emerged in 1886, when Hertz discovered that metallic and dielectric objects reflect radio waves. Though substantial progress in radar technology has been made since, the most rapid development of radar systems has occurred during the Second World War, which is also the time when the term Radar was coined by the US Navy. Although originally only meant for target detection and early warning, today radar is being used in a countless number of applications, such as acquisition, detection, height finding, homing, mapping, navigation,…etc. Figure I. 2. shows the different types of radar systems available. Radars can be classified as ground based, airborne, space borne, or ship based radar systems. They can also be classified into numerous categories based on the specific radar characteristics, such as the frequency band, antenna type, and waveforms utilized. Another classification is concerned with the mission and/or the functionality of the radar. This includes: weather, acquisition and search, tracking, track-while-scan, fire control, early warning, over the horizon, terrain following, and terrain avoidance radars. Phased array radars utilize phased array antennas, and are often called multifunction (multimode) radars [40].

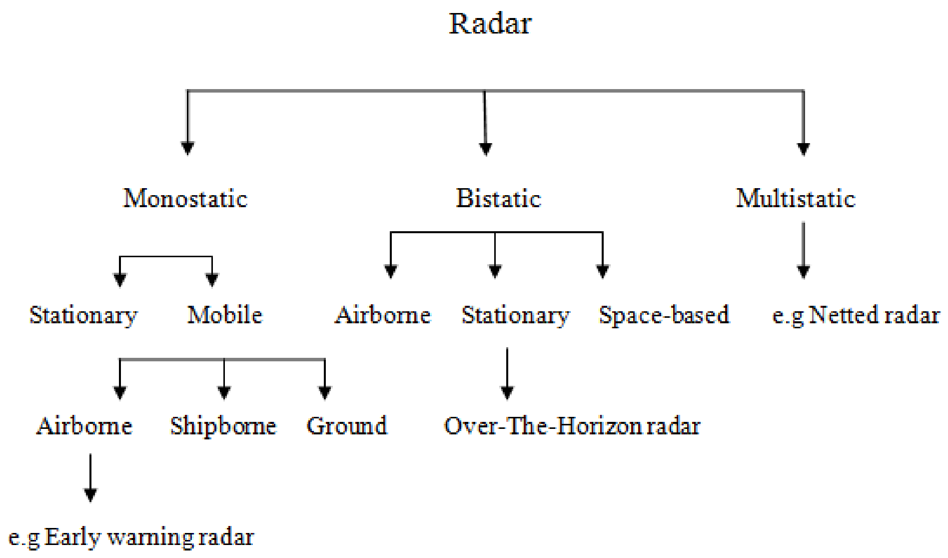

Figure I. 2: Different types of radar systems

I.2.3 Radar cross section

The term Radar Cross Section (RCS) was used to describe the amount of scattered power from a target towards the radar, when the target is illuminated by RF energy. At that time, RCS was referred to as a target-specific constant. This was only a simplification and, in practice, it is rarely the case [40]. The RCS is a measure of how detectable an object is by radar. A larger RCS indicates that an object is more easily detected. An object reflects a limited amount of radar energy back to the source. The factors that influence this include:

- The material of which the target is made;
- The absolute size of the target;
- The relative size of the target (in relation to the wavelength of the illuminating radar);

- The incident angle (angle at which the radar beam hits a particular portion of the target, which depends upon the shape of the target and its orientation to the radar source);
- The reflected angle (angle at which the reflected beam leaves the part of the target hit; it depends upon incident angle);
- The polarization of the transmitted and the received radiation with respect to the orientation of the target.

Assume the power density of a wave incident on a target located at range R away from the radar is P_{Di} . The amount of reflected power from the target is

$$P_r = \sigma P_{Di} \tag{I.1}$$

where σ denotes the target cross section. Define P_{Dr} as the power density of the scattered waves at the receiving antenna. It follows that

$$P_{Dr} = \frac{P_r}{4\pi R^2} \tag{I.2}$$

Equating (I.1) and (I.2) yields

$$\sigma = 4\pi R^2 \frac{P_{Dr}}{P_{Di}} \tag{I.3}$$

and in order to ensure that the radar receiving antenna is in the far field (i.e., scattered waves received by the antenna are planar), (I.3) is modified

$$\sigma = 4\pi R^2 \lim_{R\to\infty}\left(\frac{P_{Dr}}{P_{Di}}\right) \tag{I.4}$$

The RCS defined by (I.4) is often referred to as either the monostatic RCS, the backscattered RCS, or simply target RCS.

The backscattered RCS is measured from all waves scattered in the direction of the radar and has the same polarization as the receiving antenna. It represents a portion of the total scattered target RCS σ_t , where $\sigma_t > \sigma$. Assuming spherical coordinate system defined by (ρ,θ,φ), then at range ρ the target scattered cross section is a function of (θ,φ). Let the angles (θ_i,φ_i) define the direction of propagation of the incident waves. Also, let the angles (θ_s,φ_s) define the direction of propagation of the scattered waves. The special case, when $\theta_s = \theta_i$ and $\varphi_s = \varphi_i$, defines the monostatic RCS. The total target scattered RCS is given by

$$\sigma_t = \frac{1}{4\pi}\int_{\theta_s=0}^{2\pi}\int_{\varphi_s=0}^{\pi}\sigma(\theta_s,\varphi_s)\sin\theta_s\, d\theta_s\, d\varphi_s \tag{I.5}$$

The amount of backscattered waves from a target is proportional to the ratio of the target extent (size) to the wavelength, λ, of the incident waves. In fact, a radar will not be able to detect targets much smaller than its operating wavelength [40].

I.2.4 Radar equation

Consider a radar with an omni directional antenna (one that radiates energy equally in all directions). Since these kinds of antennas have a spherical radiation pattern, we can define the peak power density (power per unit area) at any point in space as

$$P_D = \frac{Peak\ transmitted\ power}{area\ of\ a\ sphere} \tag{I.6}$$

The power density at range *R* away from the radar (assuming a lossless propagation medium) is

$$P_D = \frac{P_t}{4\pi R^2} \tag{I.7}$$

where P_t is the peak transmitted power and $4\pi R^2$ is the surface area of a sphere of radius *R*. Radar systems utilize directional antennas in order to increase the power density in a certain direction. Directional antennas are usually characterized by the antenna gain *G* and the antenna effective aperture A_e. They are related by

$$A_e = \frac{G\lambda^2}{4\pi} \tag{I.8}$$

where λ is the wavelength. The relationship between the antenna's effective aperture A_e and the physical aperture *A* is $A_e = \rho A,\ 0 \le \rho \le 1$. ρ is referred to as the aperture efficiency, and good antennas require $\rho \to 1$. In this case we will assume, unless otherwise noted, that *A* and A_e are the same. We will also assume that antennas have the same gain in the transmitting and receiving modes. In practice, $\rho = 0.7$ is widely accepted. The power density at a distance *R* away from a radar using a directive antenna of gain *G* is then given by

$$P_D = \frac{P_t G}{4\pi R^2} \tag{I.9}$$

when the radar radiated energy impinges on a target, the induced surface currents on that target radiate electromagnetic energy in all directions. If we set $\sigma = P_r / P_D$, the total power delivered to the radar signal processor by the antenna is

$$P_{Dr} = \frac{P_t G \sigma}{\left(4\pi R^2\right)^2} A_e \qquad \text{(I.10)}$$

Substituting (I.8) into (I.10), (I.10) becomes

$$P_{Dr} = \frac{P_t G^2 \lambda^2 \sigma}{\left(4\pi\right)^3 R^4} \qquad \text{(I.11)}$$

Let S_{min} denote the minimum detectable signal power. It follows that the maximum radar range R_{max} is

$$R_{max} = \left(\frac{P_t G^2 \lambda^2 \sigma}{\left(4\pi\right)^3 S_{min}}\right)^{1/4} \qquad \text{(I.12)}$$

(I.12) suggests that in order to double the radar maximum range, one must increase the peak transmitted power P_t sixteen times; or equivalently, one must increase the effective aperture four times [40].

I.3 Radar clutter

Clutter is a term used for unwanted echoes in electronic systems, particularly in reference to radars. Radar clutter echoes consist of radar returns from reflectors that are not of interest and often obscure the signals from targets that are of interest. Radar clutter signals are typically caused by things such as rain, chaff, sea, woods, mountains and atmospheric turbulences, and can cause serious performance issues with radar systems. Clutter in some applications might be reflectors or targets of interest in other applications. This is illustrated by ground-mapping radar where reflections from the ground are of interest. Often clutter returns are much stronger than target returns and radar processing is required to improve the signal-to-clutter ratio (SCR). Several techniques are available to achieve this goal. One method is to reduce the resolution cell size in angle and range in order to decrease the amount of clutter return that competes with the target. Another method is to take advantage of differences between polarization characteristics of the target and the clutter. A third method is to filter the signals to improve the SCR based on the differences in Doppler frequency because echoes from desired targets are generally moving at a high radial velocity than clutter signals. Clutter can be classified into two main categories: surface clutter and airborne or volume clutter. Surface clutter changes from one area to another, while volume clutter may be more predictable [1, 2, 3, 39, 40].

Clutter echoes are random and have thermal noise-like characteristics because the individual clutter components (scatterers) have random phases and amplitudes. In many cases, the clutter signal level is much higher than the receiver noise level. Thus, the radar's ability to detect targets embedded in high clutter background depends on the SCR rather than the SNR. White noise normally introduces the same amount of noise power across all radar range bins, while clutter power may vary within a single range bin. Since clutter returns are target-like echoes, the only way a radar can distinguish target returns from clutter echoes is based on the target RCS σ_t , and the anticipated clutter RCS σ_c (via clutter map). Clutter RCS can be defined as the equivalent radar cross section attributed to reflections from a clutter area, A_C. The average clutter RCS is given by $\sigma_c = \sigma^0 A_c$, where σ^0 is the clutter scattering coefficient, a dimensionless quantity that is often expressed in dB. Some radar engineers express σ^0 in terms of squared centimeters per squared meter. In these cases, σ^0 is $40dB$ higher than normal.

I.3.1 Surface clutter

Surface clutter includes both land and sea-clutter, and is often called area clutter. Surface clutter includes trees, vegetation, ground terrain, man-made structures, and sea surface (sea clutter). Area clutter manifests itself in airborne radars in the look-down mode. It is also a major concern for ground-based radars when searching for targets at low grazing angles. The grazing angle ψ_g is the angle from the surface of the earth to the main axis of the illuminating beam, as illustrated in Figure I. 3.

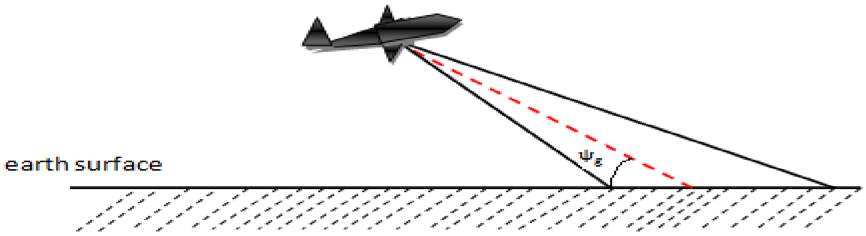

Figure I.3: Definition of grazing angle [40].

Three factors affect the amount of clutter in the radar beam. They are the grazing angle, surface roughness, and the radar wavelength. Typically, the clutter scattering coefficient σ^0 is larger for smaller wavelengths. Figure I. 4 shows a sketch describing the dependency of σ^0 on the grazing angle. Three regions are identified; they are the low grazing angle region, flat or plateau region, and the high grazing angle region.

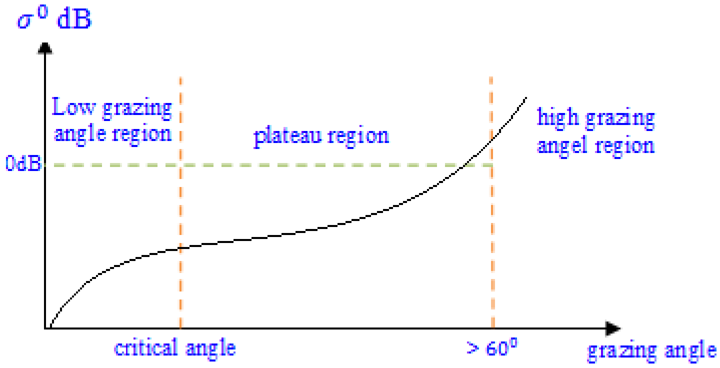

Figure I.4: Clutter regions [40].

Clutter at low grazing angles is often referred to as diffuse clutter, where there are a large number of clutter returns in the radar beam (non-coherent reflections). In the flat region the dependency of σ^0 on the grazing angle is minimal. Clutter in the high grazing angle region is more specular (coherent reflections) and the diffuse clutter components disappear. In this region the smooth surfaces have larger σ^0 than rough surfaces, opposite of the low grazing angle region.

Consider airborne radar in the look-down mode as shown in Figure I. 5. The intersection of the antenna beam with the ground defines an elliptically shaped footprint. The size of the footprint is a function of the grazing angle and the antenna 3dB beam width θ_{3dB} , as illustrated in Figure I. 6. The footprint is divided into many ground range bins each of size $(c\tau/2)\sec\psi_g$, where τ is the pulse width, c is speed of light. From Figure I. 6, a resolution area A_c is

$$A_c \approx R\theta_{3dB}\frac{c\tau}{2}\sec\psi_g \qquad \text{(I.13)}$$

where $\sec(x) = 1/\cos(x)$

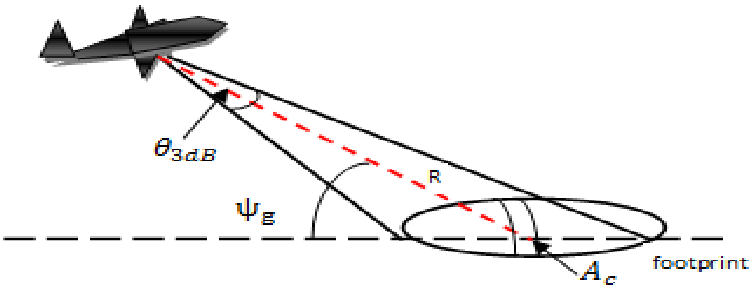

Figure I.5: Airborne radar in the look-down mode [40].

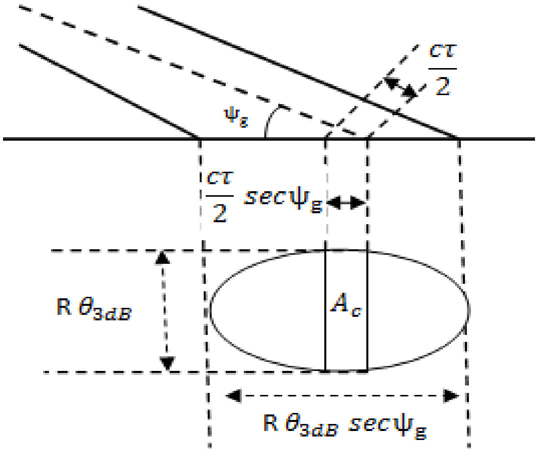

Figure I. 6: Footprint definition [40].

The SCR for area clutter is given by [40].

$$SCR_c = \frac{2\sigma_t \cos\psi_g}{\sigma^0 \theta_{3dB} R c\tau} \tag{I.14}$$

where σ_t is the target RCS.

I.3.2 Volume clutter

Volume clutter normally has large extent and includes chaff, rain, snow, hail, birds, and insects and other flying particles. Weather or rain clutter is easier to suppress than chaff, since rain droplets can be viewed as perfect small spheres. A resolution volume is shown in Figure I. 7. and is approximated by

$$V_W \approx \frac{\pi}{8}\theta_a \theta_e R^2 c\tau \tag{I.15}$$

where θ_e , θ_a are, respectively, the antenna beam width in azimuth and elevation.

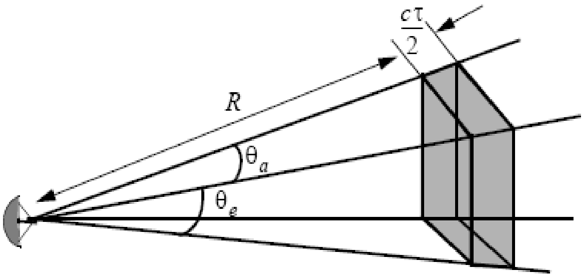

Figure I.7: Definition of a resolution volume [40].

The SCR$_c$ for weather clutter is computed as

$$SCR_c = \frac{8\sigma_t}{\pi\theta_a\theta_e c\tau R^2 \sum_{i=1}^{N}\sigma_i} \tag{I.16}$$

where σ_i is the i^{th} rain droplet RCS approximation.

I.3.3 Clutter models

Since clutter within a resolution cell or volume is composed of a large number of scatterers with random phases and amplitudes, it is statistically described by a PDF. The type of distribution depends on the nature of clutter itself (sea, land or volume), the radar operating frequency, and the grazing angle. Typically, clutter is non stationary in that its statistical characterization varies with time. The power spectrum of sea clutter is therefore a function of two variables: time and frequency. As discussed earlier, clutter could be so strong so that the targets are difficult or even impossible to be detected. The modeling of clutter has been investigated in depth because a proper model is essential in clutter suppression, and there are several widely adopted statistical models fitting reality quite well, such as the Rayleigh, log-normal, Weibull, non-central Chi-square, and *K* distributions [3, 40, 41].

If sea or land clutter is composed of many small scatterers when the probability of receiving an echo from one scatterer is statistically independent of the echo received from another scatterer, then the clutter may be modeled using a Rayleigh distribution. Generally weather clutter or smooth surface clutter is modeled by a Rayleigh PDF where either the in-phase *I* or quadrature *Q* component follows the following Gaussian distribution

$$p(I) = p(Q) = \frac{1}{\sqrt{2\pi}\sigma}\exp\left(-\frac{I^2}{2\sigma^2}\right) \tag{I.17}$$

where σ^2 is the variance. The output of the envelop detector, $X = \sqrt{I^2+Q^2}$ is Rayleigh distributed.

$$p(x) = \frac{x}{\sigma^2}\exp\left(-\frac{x^2}{2\sigma^2}\right) \tag{I.18}$$

where $2\sigma^2$ is the mean squared value of *X*.

In modern high resolution adaptive thresholding radar CFAR, the clutter (sea clutter, weather clutter, or land clutter) returns may not follow the Gaussian or Rayleigh model, since the amplitude distribution develops a “larger” tail that may increase the false alarm rate. The log-normal distribution best describes land clutter at low grazing angles. It also fits sea clutter in the plateau region. It is given by [33]

$$p(x) = \frac{1}{\sigma\sqrt{2\pi}\,x} exp\left(-\frac{(ln(x)-\mu)^2}{2\sigma^2}\right) \quad , \tag{I.19}$$

where μ and σ are the median and the standard deviation of the random variable ln(*x*)(x> 0, $\mu \in [-\infty, +\infty]$) respectively. The Weibull PDF is used to model clutter at low grazing angles (less than five degrees) for frequencies between 1 and 10GHz. The Weibull PDF is determined by the Weibull slope parameter *a* and a median scatter coefficient $\bar{\sigma}_0$, and is given by [32]

$$p(x) = \frac{c}{b}\left(\frac{x}{b}\right)^{c-1} \exp\left(-\left(\frac{x}{b}\right)^{c}\right) \tag{I.20}$$

where *c*=1/*a* is the shape parameter and $b = \bar{\sigma}_0^{1/c}$ is the scale parameter.

CG models are often used to characterize heavy tailed clutter distributions in high-resolution radar. The key problems in CG clutter modeling are choosing the texture distribution and estimating its parameters. Previous work on the modeling of the envelope of sea clutter returns have shown that excellent agreement with observed data can be achieved form the *K*-distribution at low grazing angles (less than one degree) [15]. The latter consists of two components of the envelope amplitude of the clutter returns. The first is the local mean level *y* with a PDF *p*(*y*) (texture component) which has been found to be a good fit to the Chi family of amplitude distributions [15]. This local mean level characterizes the mean level variation of clutter spikes. The second component is termed the "speckle" component which follows Rayleigh distribution indicating a return from multiple scatters. For the *K* distribution, the speckle and the texture components are respectively given by the following laws

$$p(x|y) = \frac{\pi x}{2y^2} \exp\left(-\frac{\pi x^2}{4y^2}\right) \tag{I.21}$$

and

$$p(y) = \frac{2b^{2\nu} y^{2\nu-1}}{\Gamma(\nu)} \exp(-b^2 y^2) \tag{I.22}$$

Using (I.21) and (I.22), the overall amplitude distribution is a *K*-distribution

$$p(x) = \int_0^\infty p(x|y)p(y)dy = \frac{4c}{\Gamma(\nu)}(cx)^\nu K_{\nu\text{-}1}(2cx) \tag{I.23}$$

where $K_{\nu\text{-}1}(2cx)$ is the modified Bessel function, c is a scale parameter ($c = b\sqrt{\pi/4}$) and ν is the shape parameter and $\Gamma(.)$ is the gamma function.

Another way to compute $p(x)$ is to present a CG model for a radar sea/land clutter $x(t)$ by a product of two components [7]

$$x(t) = \sqrt{\tau(t)}.y(t) \tag{I.24}$$

where t is a discrete time index, and $x(t)$ is samples from a given range cell at repetition frequency. $y(t) = y_I(t) + y_Q(t)$ is a stationary complex Gaussian process which accounts for local backscattering where $y_I(t)$ and $y_Q(t)$ are white Gaussian noises. The factor $\tau(t)$ is a nonnegative real random process, usually called the texture; it describes the variations of the local reflected power due to the tilting of the illuminated area. Another form of the compound Gaussian (CG) model can be obtained if the random variable τ follows the inverse gamma distribution [7]

$$p(\tau) = \frac{1}{\beta^{\alpha}\Gamma(\alpha)}\tau^{-(\alpha+1)}\,exp(-1/\beta\tau) \tag{I.25}$$

where α is the shape parameter and β is the scale parameter. Using (I.21) and (I.25), the magnitude or the amplitude of the clutter $R = |x| = \sqrt{\tau}|y|$ follows the Pareto type II model [7]

$$p(x) = \int_0^{\infty} p(x|y)p(y)dy = \frac{2x\beta\Gamma(\alpha+1)}{(\beta x^2+1)^{\alpha+1}\Gamma(\alpha)} \tag{I.26}$$

To provide an excellent description of sea clutter measurements, the generalized compound (GC) PDF is considered in the past [17]. The particularity of this PDF is the deviation of the speckle component from Rayleigh to Weibull or other PDF with longer tails. For this the GC PDF is formed using the generalized gamma (GΓ) law to characterize both the speckle and the modulation components of the radar clutter [17]

$$\begin{cases} p(x|y) = \dfrac{b_1}{y\Gamma(\nu_1)}\left(\dfrac{x}{y}\right)^{b_1\nu_1-1} exp\left(-\left(\dfrac{x}{y}\right)^{b_1}\right) \\ p(y) = \dfrac{b_2}{y\Gamma(\nu_2)}\left(\dfrac{y}{a}\right)^{b_2\nu_2-1} exp\left(-\left(\dfrac{y}{a}\right)^{b_2}\right) \end{cases} \tag{I.27}$$

where a is the scale parameter, $\nu_{1,2}$ are the shape parameters, and $b_{1,2}$ are the power parameters of the $G\Gamma$ model. Using (I.27), the overall PDF of X yields [17]

$$
\begin{aligned}
p(x) &= \int_0^\infty p(x|y)p(y)dy \\
&= \frac{b_1 b_2}{\Gamma(\nu_1)\Gamma(\nu_2)} \frac{x^{b_1\nu_1-1}}{a^{b_2\nu_2}} \int_0^\infty y^{b_2\nu_2-b_1\nu_1-1} \exp\left(-\left(\frac{x}{y}\right)^{b_1} - \left(\frac{y}{a}\right)^{b_2}\right)
\end{aligned}
\tag{I.28}
$$

As shown in Table I. 1, several statistical models that are commonly used for radar clutter modeling can be inspired from the GC PDF given by (I.28).

Table I.1: Distributions of sea clutter inspired from the GC PDF

Distribution	**Parameters**	**Speckle**	**Texture**
GC (General Compound)	ν_1, ν_2, b_1, b_2 and a	Generalized gamma	Generalized gamma
GK (Generalized *K*)	ν_1, ν_2, $b_1 = b_2 = b$ and a	Generalized gamma	Generalized gamma
K	$\nu_1 = 1$, $\nu_2 = \nu$, $b_1 = b_2 = b = 2$ and a	Rayleigh	gamma
WG (Weibull speckle, Gamma mean)	$\nu_1 = 1$, $\nu_2 = \nu$, $b_1 = b$, $b_2 = 2$ and a	Weibull	gamma
Weibull	$\nu_1 = 1$, $\nu_2 = 1/2$, $b_1 = b_2 = b$ and a	Weibull	Generalized gamma
Rayleigh	$\nu_1 = 1$, $\nu_2 = 1/2$, $b_1 = b_2 = b = 2$ and a	Rayleigh	-
Exponential	$\nu_1 = 1$, $\nu_2 = 1/2$, $b_1 = b_2 = b = 1$ and a	Exponential	-
HG (Hypergeometric gamma)	ν_1, ν_2, b_1, b_2 and a or b_1 and b_2 are integers	Generalized gamma	Generalized gamma

I.4 Targets models

Most objects of interest, such as aircraft, ships, and many other types of irregular shapes, consist of groups of scattering facets that interfere with each other, and only statistical estimations are valid. These vary from spherical objects, which give a constant reflection to an irregular cluster of equally sized reflectors. The reflections from such clusters are constant during the short radar pulse length. If the radar frequency changes, there are different interference effects that depend on the probability distribution of the scatterer. This is the same distribution as if the object were rotated when measured at a constant frequency. Steady echoes are the easiest to detect and measure. Fluctuating echoes must be observed during a number of fading cycles to obtain a reasonable mean value for detection and measurement. A number of probability distributions have been postulated (see Table I. 2) with decreasing degrees of dispersion [39].

Table I.2: A number of probability distributions used to describe scatterers [39].

Distribution	Used for
Log-normal	Ground clutter, ships
Weinstock	Aircrafts
Swerling I and II models	Aircrafts
Swerling III and IV models	Missiles
Rice	Satellites
Uniform for steady or Marcum model Towed spheres	Towed spheres

The radar equation uses the mean RCS to calculate the average echoed signal. Except for the log-normal case, the probability distributions are related to gamma distributions [39].

When a target is present, the amplitude of the signal at the receiver depends on the target RCS, which is the effective scattering area of a target as seen by the radar. In general, the target RCS fluctuates because targets consist of many scattering elements, and returns from each scattering element vary. The effect of the fluctuation is to require a higher SNR for high probability of detection, and lower values for low probability of detection than those required with non fluctuating signals. In addition, returns from the same scattering element are functions of the illumination angle, the frequency and polarization of the transmitted wave, the target motion and vibration, and the kinematics associated with the radar itself [41]. Target RCS fluctuations are often modeled according to the four Swerling target cases, Swerling case 1 to 4. These fluctuating models assume that the target RCS fluctuation follows either a Rayleigh or one-dominant-plus Rayleigh distribution with scan-to-scan or pulse-to pulse statistical independence.

I.4.1 Weinstock models

The Weinstock model uses the modified gamma distribution with η between 0.6 and 4 given by [39]

$$p(s) = \frac{\eta^{\eta}}{\Gamma(\eta)} s^{\eta-1} e^{-\eta s} \tag{I.29}$$

I.4.2 Swerling models

Swerling Case 1: In this case, the returned signal power per pulse on any one scan is assumed to be constant, but these echo pulses are independent (uncorrelated) from scan to scan. A returned signal of this type is then a scan-to-scan fluctuation. The intensity of the entire pulse-train is a single exponential-distributed independent random variable given by [41]

$$p(s) = \frac{1}{m_s} \exp\left(-\frac{s}{m_s} \right) \tag{I.30}$$

where m_s is the average cross section (average of RCS or signal-to-noise power ratio S) over all target fluctuations.

Swerling Case 2: In this case, the fluctuations are more rapid than in Case 1, and are assumed to be independent from pulse-to-pulse instead of from scan-to-scan. This is pulse-to-pulse fluctuation where the voltages of the echoes from the scatterer are parts of a PDF given in (I.30).

Swerling Case 3: In this case, the fluctuations are scan-to-scan as in Case 1, but the PDF is given by

$$p(s) = \frac{4s}{m_s^2} \exp\left(-\frac{2s}{m_s} \right) \tag{I.31}$$

Swerling Case 4: In this case, the fluctuations are pulse-to-pulse as in Case 2, but the PDF is given by (I.31).

Note that in Cases 1 and 2, the targets are assumed to be composed of a large number of independent scatterers, none of which dominates (e.g., large aircraft). Cases 3 and 4 represent targets that have a single dominant nonfluctuating scatterer, together with other smaller independent scatterers (e.g., missiles). Observe that Cases 1 and 2 targets produce signals whose envelopes are Rayleigh distributed, while Cases 3 and 4 targets produce signals whose envelopes are chisquared distributed [41].

Swerling Cases 1 to 4 are the models most commonly used, even though other models have been developed. They are summarized in the chi-square χ^2 target models family [41].

$$p(s) = \frac{1}{\Gamma(k)} \frac{k}{m_s} \left(\frac{ks}{m_s} \right)^{k-1} \exp\left(-\frac{ks}{m_s} \right) \tag{I.32}$$

Swerling Case 5*:* Often, non fluctuating targets are said to have Swerling Case 5 or Swerling Case 0. In this case, the received signal amplitude is assumed unknown, and there is no amplitude or RCS fluctuation.

I.4.3 Rice models

The echoes from one large scatterer accompanied by several much smaller ones, such as a spherical satellite with antennas, are represented by the Rice distribution namely [39].

$$p(s) = (1+s)\exp\left(-s-(1+s)x\right)I_0\left(2\sqrt{s(1+s)x}\right) \tag{I.33}$$

where S is the ratio of the power of the steady component to the total power in the random components, I_0 is the modified Bessel function of zero order. The Rice distribution may be approximated to the modified gamma distribution by equating the means and variances of the two distributions ($\eta = 1 + s^2 /(1+2s)$).

I.5 Decision theory

In engineering, when there is a radar signal detection problem, the returned signal is observed and a decision is made as to whether a target is present or absent. In a digital communication system, a string of zeros and ones may be transmitted over some medium. At the receiver, the received signals representing the zeros and ones are corrupted in the medium by some additive noise and by the receiver noise. The receiver does not know which signal represents a zero and which signal represents a one, but must make a decision as to whether the received signals represent zeros or ones. The process that the receiver undertakes in selecting a decision rule falls under the theory of signal detection [41].

The situation above may be described by a source emitting two possible outputs at various instants of time. The outputs are referred to as hypotheses. The null hypothesis H_0 represents a zero (target not present) while the alternate hypothesis H_1 represents a one (target present), as shown in Figure I.8. (a). Each hypothesis corresponds to one or more observations that are represented by random variables. Based on the observation values of these random variables, the receiver decides which hypothesis (H_0 or H_1) is true. Assume that the receiver is to make a decision based on a single observation of the received signal. The range of values that the random variable Y takes constitutes the observation space Z. The observation space is partitioned into two regions Z_0 and Z_1, such that if Y lies in Z_0 the receiver decides in favor of

H_0, while if Y lies in Z_1 the receiver decides in favor of H_1, as shown in Figure I. 8. (b). The observation space Z is the union of Z_0 and Z_1; that is, $Z = Z_0 \cup Z_1$

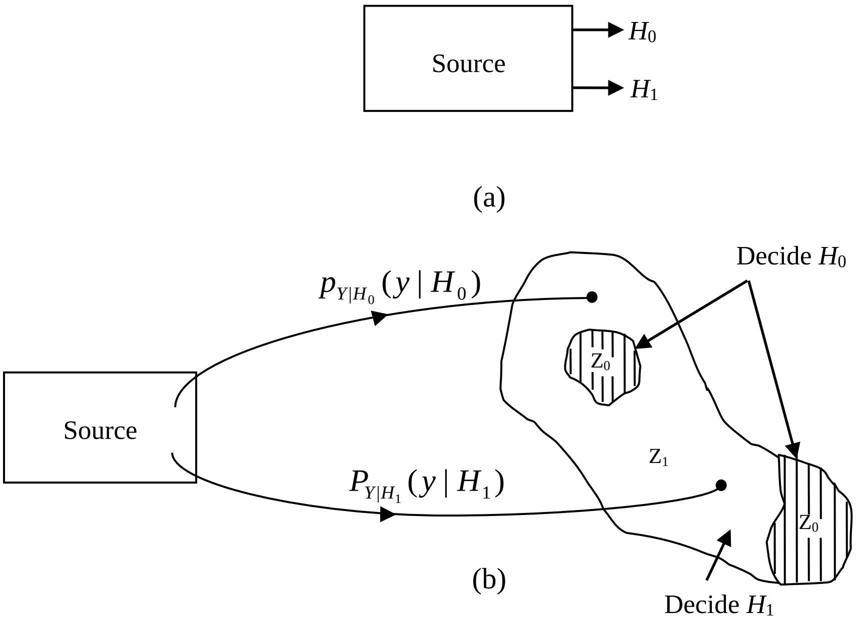

Figure I. 8: (a) Source for binary hypothesis.
(b) Decision regions.

The PDF of Y corresponding to each hypothesis are $P_{Y|H_0}(y \mid H_0)$ and $P_{Y|H_1}(y \mid H_1)$, where y is a particular value of the random variable Y.

Each time, a decision is made, based on some criteria, for this binary hypothesis testing problem, four possible cases can occur:

(1). Decide H_0 when H_0 is true.

(2). Decide H_0 when H_1 is true.

(3). Decide H_1 when H_0 is true.

(4). Decide H_1 when H_1 is true.

Observe that for cases (1) and (4), the receiver makes a correct decision, while for cases (2) and (3), the receiver makes an error. From radar nomenclature, case (2) is called miss, case (3) a false alarm, and case (4) detection.

In the next sections, we study some of the criteria that are used in decision theory, and the conditions under which these criteria are useful [41].

I.5.1 Bayes criterion

In using Bayes criterion, two assumptions are made. First, the probability of occurrence of the two source outputs is known. They are the *a priori* probabilities $P(H_0)$ and $P(H_1)$. $P(H_0)$ is the probability of occurrence of hypothesis H_0, while $P(H_1)$ is the probability of occurrence of hypothesis H_1. Denoting the *a priori* probabilities $P(H_0)$ and $P(H_1)$ by P_0 and P_1 respectively. If we let D_i, $i = 0,1$, where D_0 denotes "decide H_0" and D_1 denotes "decide H_1," we can define C_{ij}, $i, j = 0,1$, as the cost associated with the decision D_i, given that the true hypothesis is H_j. Given $P(D_i, H_j)$, the joint probability that we decide D_i, and that the hypothesis H_j is true, the average cost is

$$\Re = E[C] = C_{00}P(D_0, H_0) + C_{01}P(D_0, H_1) + C_{10}P(D_1, H_0) + C_{11}P(D_1, H_1) \tag{I.34}$$

From Bayes′ rule, we have

$$P(D_i, H_j) = P(D_i \mid H_j)P(H_j) \tag{I.35}$$

where

$$\begin{cases} P(D_0 \mid H_0) = \int_{Z_0} P_{Y|H_0}(y \mid H_0)dy \\ P(D_0 \mid H_1) = \int_{Z_0} P_{Y|H_1}(y \mid H_1)dy \\ P(D_1 \mid H_0) = \int_{Z_1} P_{Y|H_0}(y \mid H_0)dy \\ P(D_1 \mid H_1) = \int_{Z_1} P_{Y|H_1}(y \mid H_1)dy \end{cases} \tag{I.36}$$

The probabilities $P(D_0 \mid H_1)$, $P(D_1 \mid H_0)$, and $P(D_1, H_1)$ represent the probability of miss, P_M, the probability of false alarm, P_{FA}, and the probability of detection, P_D, respectively ($P_M = 1 - P_D$ and $P(D_0 \mid H_0) = 1 - P_F$). The average cost is given by

$$\Re = E[C] = C_{00}(1 - P_F)p_0 + C_{01}(1 - P_D)p_1 + C_{10}P_F p_0 + C_{11}P_D p_1 \tag{I.37}$$

In terms of the decision regions, the average cost is expressed as

$$\begin{aligned} \Re = {} & P_0C_{00}\int_{Z_0} P_{Y|H_0}(y \mid H_0)dy + P_1C_{01}\int_{Z_0} P_{Y|H_1}(y \mid H_1)dy \\ & + P_0C_{10}\int_{Z_1} P_{Y|H_0}(y \mid H_0)dy + P_1C_{11}\int_{Z_1} P_{Y|H_1}(y \mid H_1)dy \end{aligned} \tag{I.38}$$

The fact that $\int_Z P_{Y|H_0}(y \mid H_0)dy = \int_Z P_{Y|H_1}(y \mid H_1)dy = 1$, we can write

$$\int_{Z_1} P_{Y|H_j}(y \mid H_j)dy = 1 - \int_{Z_0} P_{Y|H_j}(y \mid H_j)dy, \quad j = 0,1 \tag{I.39}$$

Consequently, the risk is minimized by selecting the decision region Z_0 to include only those points of Y for which the second term is larger, and hence the integrand is negative. Specifically, we assign to the region Z_0 those points for which

$$P_1(C_{01}-C_{11})P_{Y|H_1}(y\,|\,H_1)<P_0(C_{10}-C_{00})P_{Y|H_0}(y\,|\,H_0) \tag{I.40}$$

All values for which the second term is greater will be excluded from Z_0 and assigned to Z_1. The values for which the two terms are equal do not affect the risk, and can be assigned to either Z_0 or Z_1. Consequently, we say if

$$P_1(C_{01}-C_{11})P_{Y|H_1}(y\,|\,H_1)>P_0(C_{10}-C_{00})P_{Y|H_0}(y\,|\,H_0) \tag{I.41}$$

then we decide H_1. Otherwise, we decide H_0. Hence, the decision rule resulting from the Bayes criterion is [41].

$$\Lambda(y)=\frac{P_{Y|H_1}(y\,|\,H_1)}{P_{Y|H_0}(y\,|\,H_0)}\ \overset{H_1}{\underset{H_0}{\gtrless}}\ \frac{P_0(C_{10}-C_{00})}{P_1(C_{01}-C_{11})} \tag{I.42}$$

The ratio of $P_{Y|H_1}(y\,|\,H_1)$ over $P_{Y|H_0}(y\,|\,H_0)$ is called the likelihood ratio, and is denoted $\Lambda(y)$. We note that if we select the cost of an error to be one and the cost of a correct decision to be zero, that is, $C_{01}=C_{10}=1\,\text{and}\,C_{00}=C_{11}=0$, then the risk function of (I.37) reduces to

$$\Re=P_M P_1+P_F P_0=P(\varepsilon) \tag{I.43}$$

where $P(\varepsilon)$ is the error probability. Thus, in this case, minimizing the average cost is equivalent to minimizing the probability of error. Receivers for such cost assignment are called minimum probability of error receivers. The threshold reduces to, $\eta=\dfrac{P_0}{P_1}$.

I.5.2 Minimax criterion

The Bayes criterion assigns costs to decisions and assumes knowledge of the *a priori* probabilities. In many situations, we may not have enough information about the *a priori* probabilities and consequently, the Bayes criterion cannot be used. One approach would be to select a value of P_1, the *a priori* probability of H_1, for which the risk is maximum, and then minimize that risk function. This principle of minimizing the maximum average cost for the selected P_1 is referred to as minimax criterion. Seting $P_0=1-P_1$, the risk function in terms of P_1 is given by

$$\Re = C_{00}(1-P_F) + C_{10}P_F + P_1[(C_{11}-C_{00}) + (C_{01}-C_{11})P_M - (C_{10}-C_{00})P_F] \tag{I.44}$$

Assuming a fixed value of P_1, $P_1 \in [0,1]$, we can design a Bayes′ test. These decision regions are then determined, as are the P_{FA}, and miss, P_M. The test results in

$$\Lambda(y) \underset{H_0}{\overset{H_1}{\gtrless}} \frac{(1-P_1)(C_{10}-C_{00})}{P_1(C_{01}-C_{11})} \tag{I.45}$$

The minimax equation is given by

$$(C_{11}-C_{00}) + (C_{01}-C_{11})P_M - (C_{10}-C_{00})P_F = 0 \tag{I.46}$$

If the cost of a correct decision is zero $(C_{00} = C_{11} = 0)$, then the minimax equation for $P_1 = P_1^*$ such that $P_1^* \in (0,1)$ reduces to [41]

$$C_{01}P_M = C_{10}P_F \tag{I.47}$$

I.5.3 Neyman-pearson criterion

In the previous sections, we have seen that for the Bayes criterion we require knowledge of the *a priori* probabilities and cost assignments for each possible decision. Then, we have studied the minimax criterion, which is useful in situations where knowledge of the a priori probabilities is not possible. In many other physical situations, such as radar detection, it is very difficult to assign realistic costs and *a priori* probabilities. To overcome this difficulty, we use the conditional P_{FA}, and detection P_D. The Neyman-Pearson test requires thatP_{FA}, be fixed to some value α while P_D is maximized. Since $P_M = 1 - P_D$, maximizing P_D is equivalent to minimizing P_M.

In order to minimize P_M (maximize P_D) subject to the constraint that $P_{FA} = \alpha$, we use the calculus of extrema, and form the objective function J to be

$$J = P_M + \lambda(P_{FA} - \alpha) \tag{I.48}$$

where $\lambda(\lambda \geq 0)$ is the Lagrange multiplier. We note that given the observation space Z, there are many decision regions Z_1 for which $P_{FA} = \alpha$. The question is to determine those decision regions for which P_M is minimum. Consequently, we rewrite the objective function J in terms of the decision region to obtain

$$J = \int_{Z_0} P_{Y|H_1}(y \mid H_1)dy + \lambda\left[\int_{Z_1} P_{Y|H_0}(y \mid H_0)dy - \alpha\right] \tag{1.49}$$

using $Z = Z_0 \bigcup Z_1$, (I.49) can be rewritten as

$$\begin{aligned} J &= \int_{Z_0} P_{Y|H_1}(y \mid H_1)dy + \lambda\left[\int_{Z_0} P_{Y|H_0}(y \mid H_0)dy - \alpha\right] \\ &= \lambda(1-\alpha) + \int_{Z_0} [P_{Y|H_1}(y \mid H_1) - \lambda P_{Y|H_0}(y \mid H_0)]dy \end{aligned} \tag{I.50}$$

Hence, *J* is minimized when values for which $f_{Y|H_1}(y \mid H_1) > f_{Y|H_0}(y \mid H_0)$ are assigned to the decision region Z_1. The decision rule is, therefore,

$$\Lambda(y) = \frac{P_{Y|H_1}(y \mid H_1)}{P_{Y|H_0}(y \mid H_0)} \begin{array}{c} H_1 \\ > \\ < \\ H_0 \end{array} \lambda \tag{I.51}$$

The threshold η derived from the Bayes 'criterion is equivalent to λ, the Lagrange multiplier in the Neyman-Pearson (N-P) test for which the P_{FA} is fixed to the value α. If we define the conditional density of Λ given that H_0 is true as $P_{\Lambda|H_0}(\lambda \mid H_0)$, then $P_{FA} = \alpha$ may be rewritten as [41]

$$P_F = \int_{Z_1} P_{Y|H_0}(y \mid H_0)dy = \int_{\lambda}^{\infty} P_{\Lambda(y)|H_0}[\lambda(y) \mid H_0]d\lambda \tag{I.52}$$

The test is called most powerful of level α if its probability of rejecting H_0 is α.

I.6 CFAR detection

In practical radar signal detection systems, the problem is to automatically detect a target in thermal noise plus clutter [4, 41]. The input signal at the radar receiver, when a target is present, is an attenuated randomly phase-shifted version of the transmitted pulse in noise. A typical radar processor for a single-range cell sums the *K* samples of the matched filter output and compares the sum to a fixed threshold, as shown in Figure I. 9. In this case, a small increase in noise power causes the P_{FA}, to increase intolerably.

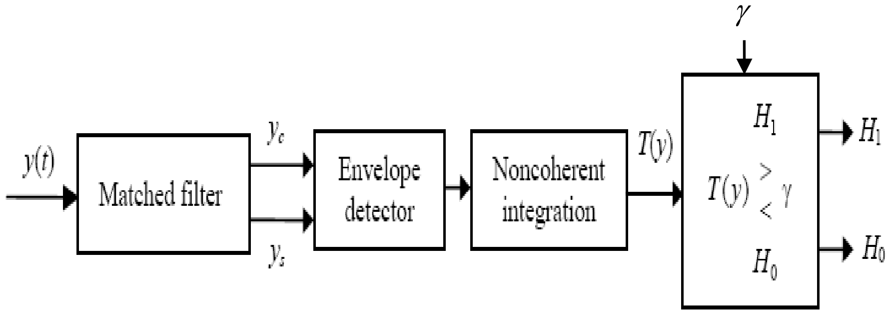

Figure I.9: A Scheme for a fixed threshold radar detection.

The role of the CFAR circuitry is therefore to determine the power threshold which any return can be considered to probably originate from a target. If this threshold is too low, then more targets will be detected at the expense of increased numbers of false alarms. Conversely, if the threshold is too high, then fewer targets will be detected, but the number of false alarms will also be low [4, 41]. In most radar detectors, the threshold is set in order to achieve a required P_{FA} (or equivalently, false alarm rate or time between false alarms). If the background against which targets are to be detected is constant with time and space, then a fixed threshold level can be chosen that provides a specified P_{FA}, governed by the PDF of the noise, which is usually assumed to be Gaussian. The P_D is then a function of the SNR of the target return. However, in most fielded systems, unwanted clutter and interference sources mean that the noise level changes both spatially and temporally. In this case, a changing threshold can be used, where the threshold level is raised and lowered to maintain a constant P_{FA}. This is known as CFAR detection. Hence, when the noise variance is not known, and in order to regulate the P_{FA}, numerous CFAR procedures have been developed in the open literature in order to adaptively select a threshold level by taking a rigorous account of the statistics of the background in which targets are to be detected. In most simple CFAR detection schemes, the threshold level is calculated by estimating the level of the noise floor around the CUT. This can be found by taking a block of cells around the CUT and calculating the average power level. On the other hand, some procedures calculate separate averages for the cells to the left and right of the CUT, and then use the greatest-of or smallest-of these two power levels to define the local power level. Other related approaches estimate the background level after ordering the samples in the window. These are referred to as cell-averaging CFAR (CA-CFAR), greatest-of CFAR (GO-CFAR), smallest-of CFAR (SO-CFAR), order-statistics CFAR (OS-CFAR), censored-mean-level CFAR (CMLD-CFAR),…etc. In the following, we give the description of some of these CFAR algorithms.

There are three main approaches to the CFAR problem: the adaptive threshold processor, the nonparametric processor, and the nonlinear receiver approach. The adaptive threshold processor is the one most commonly used, because it provides the lowest CFAR loss when the actual environment closely matches the design environment. Of the hundreds of papers published in this field, we shall mention only a few to give a sketch of the advance of this rich field up to the actual interest when using high-resolution radars. A real environment in which a radar operates cannot be described by a single clutter model. We refer to homogeneous clutter in situations where the outputs of the range cells are iid. In a non homogeneous background, the adaptive threshold setting is seriously affected, resulting in a degradation of the performance [4, 26, 42, 43].

- CA-CFAR detector: Finn and Johnson [26] proposed the use of a reference channel, from which an estimate of the noise environment can be obtained, and upon which the decision threshold is adapted. The radar uses the range cells surrounding the CUT as reference cells, as shown in Figure I. 10. The detector proposed in [26] is the CA-CFAR, where the adaptive threshold is obtained from the arithmetic mean or the sum of the reference cells, $Q = \sum_{i=1}^{M} x_i$.

For a homogeneous background noise, and iid reference cells outputs, the arithmetic is the MLE. This means that the detection threshold is designed to adapt changes in the environment (Gaussian clutter). If we consider a Swerling 1 fluctuating target, the PDF of received signal for each hypothesis H_0 and H_1 is given by

$$\begin{cases} H_0 : p_X(x|H_0) = \dfrac{1}{b} exp\left(-\dfrac{x}{b}\right) \\ H_1 : p_X(x|H_1) = \dfrac{1}{b+a} exp\left(-\dfrac{x}{b+a}\right) \end{cases} \tag{I.53}$$

where a and $b = 2\sigma^2$ represent the power of signal and the power of clutter respectively. Conventionally, P_{FA} and P_D are computed using the following integrals:

$$\begin{cases} P_{FA} = \int_0^{\infty} Pr(CUT > \alpha q|H_0) p_Q(q) dq \\ P_D = \int_0^{\infty} Pr(CUT > \alpha q|H_1) p_Q(q) dq \end{cases} \tag{I.54}$$

where α is a scale factor, and $Pr(.)$ denotes probability with

$$Pr\left(CUT > \alpha q|H_0\right) = exp\left(-\frac{\alpha q}{b}\right) \tag{I.55}$$

and

$$\Pr\left(CUT > \alpha q|H_1\right) = \exp\left(-\frac{\alpha q}{b(1+SNR)}\right) \tag{I.56}$$

where $SNR=a/b$. The PDF of Q is found to be gamma distributed

$$p_Q(q) = \frac{q^{M-1}}{b^M \Gamma(M)} \exp\left(-\frac{q}{b}\right) \tag{I.57}$$

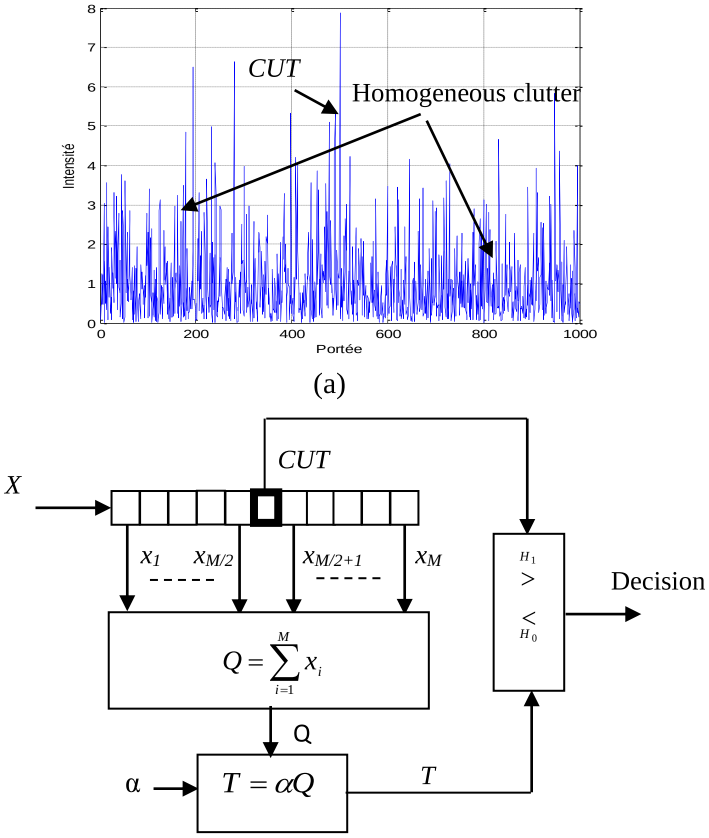

(a)

(b)

Figure I.10: CA-CFAR detector for homogeneous background
(a) Homogeneous clutter situation with $2\sigma^2 = 1$ and SNR = 5dB
(b) Arithmetic mean for ML estimate of clutter power

Substituting (I.55), (I.56) and (I.57) into (I.54), (I.54) becomes

$$\begin{cases} P_{FA} = (1+\alpha)^{-M} \\ P_D = \left(1 + \dfrac{\alpha}{1+SNR}\right)^{-M} \end{cases} \tag{I.58}$$

It is worth noting that the P_{FA} is independent of the clutter power b, which means that the CA-CFAR algorithm has a CFAR property in presence of Gaussian clutter.

- GO-CFAR detector: In the case of clutter edge situations where there is a transition in the clutter power distribution, Hansen and Sawyers [44] proposed the greatest-of-selection logic in CA-CFAR detector (GO-CFAR) to control the increase in the P_{FA}. In the GO-CFAR detector, the estimate of the noise level in the CUT is selected to be the maximum of U and V, Q = max (U, V), where U and V are the sums of the outputs of the leading and the lagging cells, respectively (see Figures I. 11 (a) and I.11. (b)). The clutter-to-clutter ratio, CCR = 5dB is taken. The random variables U and V have analog PDFs given by

$$p_U(q) = p_v(q) = \frac{q^{M/2-1}}{b^{M/2}\Gamma(M/2)}\exp\left(-\frac{q}{b}\right) \tag{I.59}$$

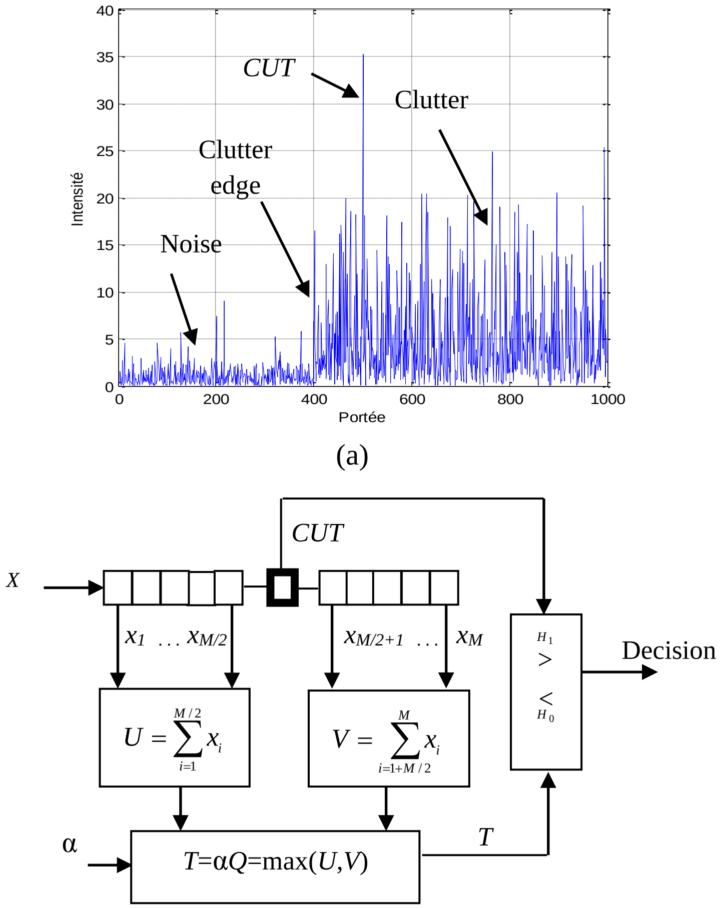

(a)

(b)

Figure I.11: GO-CFAR detector for hyterogeneous clutter
(a) clutter edge situation for $2\sigma^2 = 1$, CCR = 5dB and SNR = 10dB)
(b) ML estimation of Q from the maximum of leading and lagging windows

The Cumulative Distributed Function (CDF) of U or V is given by

$$P_U(q) = Pv(q) = \int_0^q \frac{q^{M/2-1}}{b^{M/2}\Gamma(M/2)}\exp\left(-\frac{q}{b}\right)dq \tag{I.60}$$

From [4], the PDF of Q is

$$p_Q(q) = \frac{2q^{M/2-1}}{\Gamma(N/2)}exp(-q/b)\left[1-exp(-q/b)\sum_{kr=0}^{M/2-1}\frac{(q/b)^k}{k!}\right] \tag{I.61}$$

Substituting (I.61) into (I.54), the P_{FA} and the P_D have the following forms

$$\begin{cases} P_{FA} = 2(1+\alpha)^{-M/2} - 2\sum_{i=0}^{M/2-1} \binom{M/2+i-1}{i} (2+\alpha)^{-(M/2+i)} \\ P_D = 2\left(1+\dfrac{\alpha}{1+SNR}\right)^{-M/2} - 2\sum_{i=0}^{M/2-1} \binom{M/2+i-1}{i} \left(2+\dfrac{\alpha}{1+SNR}\right)^{-(M/2+i)} \end{cases} \tag{I.62}$$

where $\binom{i}{j} = \frac{i!}{j!(i-j)!}$, is the binomial combination.

- SO-CFAR detector: If one or more interfering targets are present, Weiss [45] has shown that the GO-CFAR detector performs poorly, and suggested the use of the smallest-of-selection logic in cell averaging constant false-alarm rate detector (SO-CFAR). In the SO-CFAR detector, the minimum of U and V, Q = min (U, V) , is selected to represent the noise level estimate in the cell under test. The SO-CFAR detector was first proposed by Trunk [46] while studying the target resolution of some adaptive threshold detectors. We can intuitively see that the SO-CFAR detector performs well for the case shown in Figure I. 12 (a). From [4], the PDF of Q is

$$\begin{aligned} p_Q(q) &= p_U(q)[1-P_V(q)] + p_V(q)[1-P_U(q)] \\ &= p_U(q) + p_V(q) - [p_U(q)P_V(q) + p_V(q)P_U(q)] \\ &= p_U(q) + p_V(q) - p_Q^{GO}(q) \end{aligned} \tag{I.63}$$

Substituting (I.60) into (I.63), (I.63) will be

$$p_Q(q) = \frac{2q^{M/2-1}}{\Gamma(N/2)} exp(-2q)) \sum_{kr=0}^{M/2-1} \frac{(q)^k}{k!} \tag{I.64}$$

Replacing (I.64) into (I.54), the P_{FA} and the P_D are

$$\begin{cases} P_{FA} = 2(2+\alpha)^{-M/2} \sum_{i=0}^{M/2-1} \binom{M/2+i-1}{i} (2+\alpha)^{-i} \\ P_D = 2\left(2+\dfrac{\alpha}{1+SNR}\right)^{-M/2} \sum_{i=0}^{M/2-1} \binom{M/2+i-1}{i} \left(2+\dfrac{\alpha}{1+SNR}\right)^{-i} \end{cases} \tag{I.65}$$

- OS-CFAR detector: By studying the homogeneity of the reference cells, it has been shown that targets can be detected by the SO-CFAR detector, especially in the case where secondary targets are in a single window and are not present in the other window [47, 48]. If interfering targets are present in both the leading and lagging windows, neither the GO-CFAR detector nor the SO-CFAR detector solves the problem of the capture effect. To remedy this limitation, [48] introduced the OS-CFAR detector, that is, the OS-CFAR as shown in Figure I.13 with interfering-to-target ration, ICR = 5dB. Here, the samples of the reference window are sorted

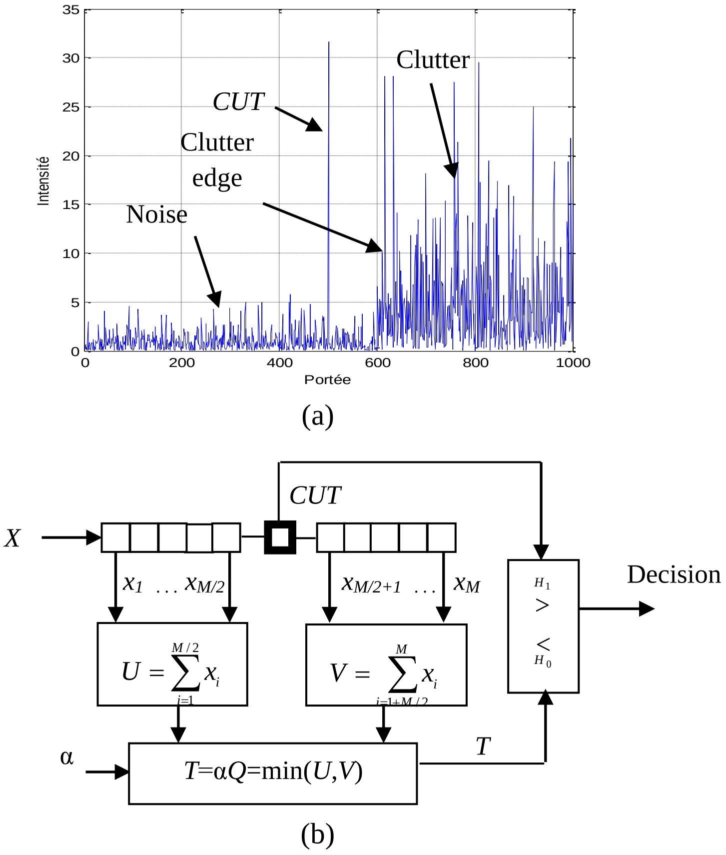

Figure I.12: SO-CFAR detector for hyterogeneous clutter
(a) clutter edge situation for $2\sigma^2 = 1$, CCR = 5dB and SNR = 10dB)
(b) ML estimation of Q from the minimum of leading and lagging windows

in ascending order and one ordered sample between them is chosen to represent the noise level estimate in the CUT. The k^{th} ordered sample value, $X\ (k)$, selected as the test statistic Q, is multiplied by the scale factor α to achieve the desired P_{FA}, and then a decision is made by comparing the output of the CUT with the adaptive threshold, $T = \alpha Q$. The value suggested in [48] to represent a good background estimate for typical radar applications in Gaussian noise is $k = 3N / 4$. The calculations of P_D and P_{FA} require the formulation of the PDF of the k^{th} ranked sample, $Q = X_{(k)}$. In the case of Gaussian homogeneous background, it is shown in [4, 48] that

$$\begin{aligned} p_Q(q) &= k\binom{M}{k}\left[P(q)\right]^{k\text{-}1}\left[1-P(q)\right]^{M\text{-}k} p(q) \\ &= \frac{k}{b}\binom{M}{k}\left(1-exp\left(-\frac{q}{b}\right)\right)^{k-1} exp\left(-\frac{q}{b}\right)^{M-k+1} \end{aligned} \qquad (I.66)$$

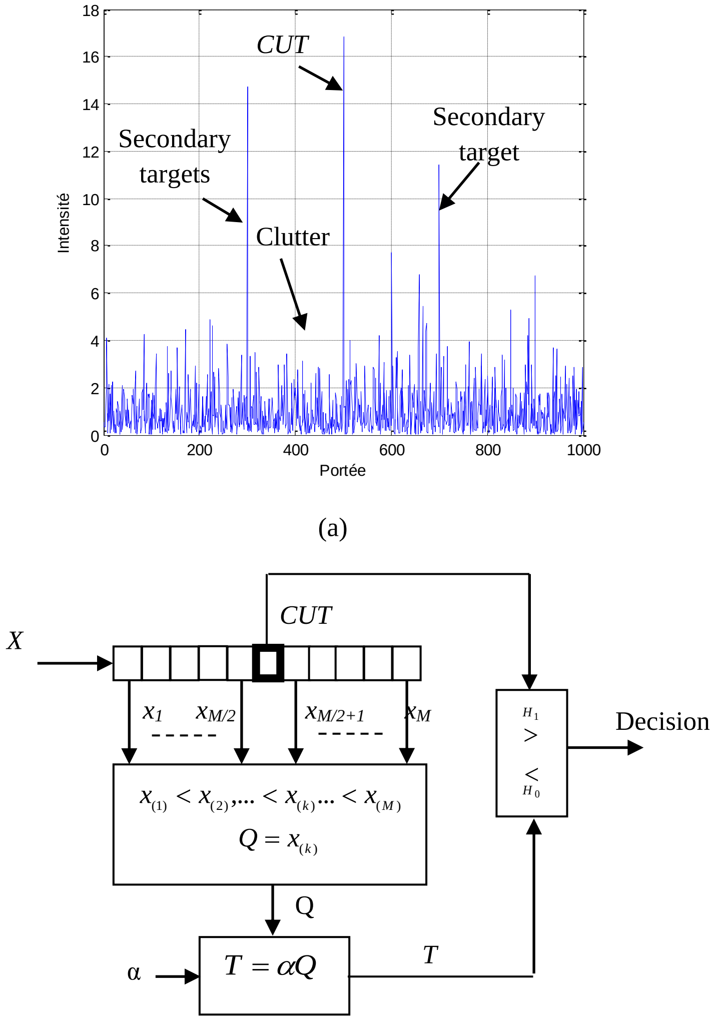

(a)

(b)

Figure I.13: OS-CFAR detector used for interfering targets situations
(a)Situation of two secondary targets ($2\sigma^2 = 1$, ICR = 5dB and SNR = 10dB).
(b) Estimation of clutter level from a selected ranked cell

Substituting (I.66) into (I.54), expressions of P_{FA} and P_D are

$$\begin{cases} P_{FA} = \int_0^\infty exp\left(-\frac{\alpha q}{b}\right)\frac{k}{b}\binom{M}{k} exp\left(-\frac{q}{b}\right)^{M-k+1}\left(1-exp\left(-\frac{q}{b}\right)\right)^{k-1} dq \\ P_D = \int_0^\infty exp\left(-\frac{\alpha q}{b(1+SNR)}\right)\frac{k}{b}\binom{M}{k} exp\left(-\frac{q}{b}\right)^{M-k+1}\left(1-exp\left(-\frac{q}{b}\right)\right)^{k-1} dq \end{cases} \qquad (I.67)$$

If we set $y = q/b$, (I.67) is simplified to

$$\begin{cases} P_{FA} = k\binom{M}{k}\int_0^{\infty} exp(-(\alpha + M + 1 - k)y)(1 - exp(-y))^{k-1}\,dq \\ P_D = k\binom{M}{k}\int_0^{\infty} exp(-(\frac{\alpha}{1+SNR} + M + 1 - k)y)(1 - exp(-y))^{k-1}\,dq \end{cases} \tag{I.68}$$

Finally, solutions of (I.68) give

$$\begin{cases} P_{FA} = \dfrac{M!}{(M-k)!}\dfrac{\Gamma(M - k + \alpha + 1)}{\Gamma(M + \alpha + 1)} \\ P_D = \dfrac{M!}{(M-k)!}\dfrac{\Gamma(M - k + 1 + \alpha/(1+SNR))}{\Gamma(M + 1 + \alpha/(1+SNR))} \end{cases} \tag{I.69}$$

I.7 Conclusion

In this chapter, we presented some basic concepts of the radar system. Radar components are described firstly, as well as its classification, radar cross-section and radar equation. As the modeling of radar clutter plays an important role in CFAR detection, we presented some statistical models for high resolution radars. It is shown that radar echoes can be scattered from sea or land surface with different grazing angles. Targets models are also given using Rayleigh and other distributions. Decision theory is introduced by giving three decision rules. Finally, some CFAR detectors used in homogeneous and hyterogeneous Gaussian clutter are also described where mathematical stages for computing probabilities of false alarm and detection are given.

2

Clutter Modeling using Mixtures of Compound Gaussian Models

Chapter outline:

II. 1 Introduction

From the previous chapter, it is discussed that parameter estimation of radar clutter is necessary to accomplish target CFAR detectors. To this effect, numerous methods to estimating the parameters of CG models with and without thermal noise have been proposed in [14, 20, 36, 37, 48, 49, 50]. In the case of the noise power is not ignored in the speckle component, the validation of the GC PDF with real data was also carried out using the matching of statistical moments for the estimates of its parameters as well as goodness-of-fit tests [17]. In [10], the analysis of IPIX data was investigated using the CIG (or CGIG), *K*, Pareto distributed clutter plus noise where the parametric curve fitting estimation method based on the N-M algorithm was used.

In this chapter, the statistical description of sea clutter using a mixture of CIG distribution, *K* distribution and generalized Pareto (GP) distribution with additive thermal noise is presented. The work presented in [36] is extended in this chapter and compared to the

K, GP and KK clutter plus noise models. To do this, the gamma, the inverse gamma and the inverse Gaussian distributions are considered to describe the modulation components. The proposed models are analyzed and the non-linear least squares curve fitting technique based on the N-M algorithm [37] is employed to obtain the optimal parameter estimation.

The rest of the chapter is structured in the following manner. In section II.2, we briefly recall the expressions of *K*, Pareto and CIG clutter plus noise PDFs. Section II.3 describes the proposed mixture models where the description and flowchart of the N-M algorithm are presented in Section II.4. Section II.5 investigates modeling comparisons using IPIX data of the proposed mixture models against the existing *K*, GP and *KK* distributions plus noise. Finally, concluding remarks are listed and commented in Section II.6.

II. 2 *K*, GP and CIG plus noise distributions

It is convenient that Compound Gaussian processes are useful to describe sea-clutter returns which consist of a rapidly varying speckle component modulated by a slowly varying texture component. Under the assumption of iid single look data, the overall CG distribution of the random variable *X*, is given by [5, 15].

$$P_x(x) = \int_0^\infty P_{x/y}\,(x/\,y)P_y(y)dy \tag{II.1}$$

If a square law detector is used and the thermal noise power denoted by $p_n = 2\sigma^2$ is incorporated, the speckle component (namely the conditional PDF of *x* given *y*) follows the exponential distribution (i.e., single pulse case) given by

$$P_{x/\,y}\,(x/y) = \frac{1}{y+P_n}\exp(-\frac{x}{y+P_n}) \tag{II.2}$$

The *K*-distribution plus noise is obtained if the texture component fluctuates according to a gamma PDF [6, 15].

$$P_y(y) = \frac{b^\nu y^{\nu-1}}{\Gamma(\nu)}\exp(-by) \tag{II.3}$$

Where ν is the shape parameter which governs the spikness of the clutter, *b* is the scale parameter. Substituting (II.2) and (II.3) into (II.1), the overall *K* plus noise PDF is given in integral form [49, 51].

$$p_X(x)=\frac{b^{\nu}}{\Gamma(\nu)}\int_0^{\infty}\frac{y^{\nu-1}}{y+p_n}\exp\left(-\frac{x}{y+p_n}\right)\exp(-by)dy \tag{II.4}$$

Integrating (II.4), from T to $+\infty$, the corresponding CCDF is given in an integral form

$$\begin{aligned}CCDF(T)&=\int_T^{+\infty}p_X(x)dx\\&=\frac{b^{\nu}}{\Gamma(\nu)}\int_0^{\infty}y^{\nu-1}\exp\left(-\frac{T}{p_n+y}\right)\exp(-by)dy\end{aligned} \tag{II.5}$$

where T denotes the normalized detection threshold. It is shown in [49] that the moment formula of order $r>0$ can be expressed as

$$\langle x^r\rangle=p_n^r\Gamma(r+1)\,{}_2F_0\left(\nu,-r;.;-\frac{1}{bp_n}\right) \tag{II.6}$$

where $\langle . \rangle$ denotes expectation and ${}_2F_0(.,.;.;.)$ is the generalized hypergeometric function. When the modulation component is an inverse Gamma PDF, the Pareto plus noise distribution is constructed [7, 50].

$$p_Y(y)=\frac{\beta^{\alpha}y^{-\alpha-1}}{\Gamma(\alpha)}\exp\left(-\frac{\beta}{y}\right) \tag{II.7}$$

where α is the shape parameter, and β is the scale parameter. Substituting (II.2) and (II.7) into (II.1), the GP plus noise PDF is obtained [20, 21].

$$p_X(x)=\frac{\beta^{\alpha}}{\Gamma(\alpha)}\int_0^{\infty}\frac{y^{-\alpha-1}}{p_n+y}\exp\left(-\frac{x}{p_n+y}\right)\exp\left(-\frac{\beta}{y}\right)dy \tag{II.8}$$

Integrating (II.8) from T to $+\infty$, the corresponding CCDF is also given in an integral form

$$CCDF(T)=\frac{\beta^{\alpha}}{\Gamma(\alpha)}\int_0^{\infty}y^{-\alpha-1}\exp\left(-\frac{T}{p_n+y}\right)\exp\left(-\frac{\beta}{y}\right)dy \tag{II.9}$$

Using (II.8), the expression of moments of order $r<\alpha$ is derived in [9] to be

$$\langle x^r\rangle=\frac{\beta^r\Gamma(1+r)\Gamma(\alpha-r)}{\Gamma(\alpha)}\,{}_2F_0\left(\alpha-r,-r;;-\frac{p_n}{\beta}\right) \tag{II.10}$$

If the inverse Gaussian law is used to describe the modulation component in (II.1), the CIG plus noise PDF is obtained. The underlying inverse Gaussian distribution is presented in [23, 52].

$$p_Y(y) = \frac{\lambda^{1/2}}{\sqrt{2\pi y^{3/2}}} \exp\left(-\lambda \frac{(y-\mu)^2}{2\mu^2 y} \right) \tag{II.11}$$

where λ is the shape parameter, and μ is the mean. Note that, λ relies upon sea conditions and radar parameters. Spiky clutter corresponds to values of $0 < \lambda < 1$ and the Exponential distribution or Gaussian clutter is attained for $\lambda \to \infty$. Substituting (II.2) and (II.11) into (II.1), the CIG PDF plus noise is expressed by

$$p_X(x) = \frac{\lambda^{1/2}}{\sqrt{2\pi}} \int_0^{\infty} \frac{y^{-3/2}}{y + p_n} \exp\left(-\frac{x}{y + p_n} \right) \exp\left(-\lambda \frac{(y-\mu)^2}{2\mu^2 y} \right) dy \tag{II.12}$$

The corresponding CCDF of (II.12) is determined to be

$$CCDF(T) = \frac{\lambda^{1/2}}{\sqrt{2\pi}} \int_0^{\infty} y^{-3/2} \exp\left(-\frac{T}{p_n + y} \right) \exp\left(-\lambda \frac{(y-\mu)^2}{2\mu^2 y} \right) dy \tag{II.13}$$

Contrary of (II.6) and (II.10), it is difficult to solve the integral of moment's expression from (II.12) of order *r*. Numerical integration is used to evaluate the following non-integer order moments [53]

$$\langle x^r \rangle = \Gamma(1+r) \sqrt{\frac{\lambda}{2\pi}} e^{\lambda/\mu} \int_0^{\infty} y^{-3/2} (y + p_n)^r \exp\left(-\frac{\lambda}{2\mu^2} y - \frac{\lambda}{2y} \right) dy \tag{II.14}$$

II.3 Proposed mixtures of CG models

The mixtures of CG models are presented with different random textures for the best tail fitting to real data. Three PDFs of the texture components are considered as devoted in Section II. 2. To this end, we resort to combine two CG distributions with an appropriate weighting factor *k* (0<*k*<1) given by [13].

$$p(x) = k p_1(x|\theta_1) + (1-k) p_2(x|\theta_2) \tag{II.15}$$

Where $\theta = [k, \theta_1, \theta_2]$ is a vector of unknown parameters to be estimated at each estimation task. The two CG distributions $p_1(x)$ and $p_2(x)$, have the same exponential distribution for the speckle component given by (II.2) and two different texture components. For instance, if we choose the CIG and the GP plus noise models to describe $p_1(x)$ and $p_2(x)$ respectively, (II.16) spans from CIG plus noise PDF to GP plus noise PDF. With *k*=1 and *k*=0 corresponding to the purely CIG plus noise distribution and the purely GP plus noise respectively. If 0<k<1, (II.16) is a mixture of the CIG and the GP plus noise PDFs. Consequently, three combinations between *K*+noise, GP+noise and CIG+noise PDFs can be used in (II.15) as will show in the following sections. However, it is shown in [36] that the best estimation of the parameters of *K*-clutter plus noise model can be achieved when the corresponding CCDF is considered in the objective (fitness) function of the N-M algorithm. To this effect, we apply in this work the PCFE method described in [36, 54] to optimize the parameters of the following CCDFs instead of mixture models given by (II.15).

II. 3.1 Mixture of CIG and GP plus noise model

If the CIG and the GP plus noise models are described by $p_1(x)$ and $p_2(x)$ respectively, (II.15) will be (after substitution (II.12) and (II.8) into (II.15))

$$\begin{aligned} p_X(x) = {} & k\frac{\lambda^{1/2}}{\sqrt{2\pi}}\int_0^\infty \frac{y^{-3/2}}{y+p_n}\exp\left(-\frac{x}{y+p_n}\right)\exp\left(-\lambda\frac{(y-\mu)^2}{2\mu^2 y}\right)dy \\ & + \frac{(1-k)\beta^\alpha}{\Gamma(\alpha)}\int_0^\infty \frac{y^{-\alpha-1}}{p_n+y}\exp\left(-\frac{x}{p_n+y}\right)\exp(-\beta/y)dy \end{aligned} \tag{II.16}$$

In this case , the CCDF obtained from a mixture of the CIG and GP plus noise models is

$$\begin{aligned} CCDF_{Pareto}^{CIG}(T) = {} & k\frac{\lambda^{1/2}}{\sqrt{2\pi}}\int_0^\infty y^{-3/2}\exp\left(-\frac{T}{y+p_n}\right)\exp\left(-\lambda\frac{(y-\mu)^2}{2\mu^2 y}\right)dy \\ & + \frac{(1-k)\beta^\alpha}{\Gamma(\alpha)}\int_0^\infty y^{-\alpha-1}\exp\left(-\frac{T}{p_n+y}\right)\exp(-\beta/y)dy \end{aligned} \tag{II.17}$$

where $\theta = [k, \lambda, \mu, \alpha, \beta, P_n]$

II.3.2 Mixture of CIG and *K* plus noise model

When the CIG and the *K* plus noise models are described by $p_1(x)$ and $p_2(x)$ respectively, (II.15) is given by (after substitution (II.12) and (II.4) into (II.15))

$$\begin{aligned} p_X(x) = {} & k\frac{\lambda^{1/2}}{\sqrt{2\pi}}\int_0^\infty \frac{y^{-3/2}}{y+p_n}\exp\left(-\frac{x}{y+p_n}\right)\exp\left(-\lambda\frac{(y-\mu)^2}{2\mu^2 y}\right)dy \\ & + \frac{(1-k)b^\nu}{\Gamma(\nu)}\int_0^\infty \frac{y^{\nu-1}}{y+p_n}\exp\left(-\frac{x}{y+p_n}\right)\exp(-by)dy \end{aligned} \tag{II.18}$$

where $\theta = [k, \lambda, \mu, \nu, b, p_n]$. The CCDF obtained from a mixture of CIG and *K* plus noise models is

$$CCDF_K^{CIG}(T) = k\frac{\lambda^{1/2}}{\sqrt{2\pi}}\int_0^\infty y^{-3/2}\exp\left(-\frac{T}{y+p_n}\right)\exp\left(-\lambda\frac{(y-\mu)^2}{2\mu^2 y}\right)dy + \frac{(1-k)b^\nu}{\Gamma(\nu)}\int_0^\infty y^{\nu-1}\exp\left(-\frac{T}{y+p_n}\right)\exp(-by)dy \quad \text{(II.19)}$$

II.3.3 Mixture of *K* and GP plus noise model

In this case, the *K* and the GP plus noise models are described by $p_1(x)$ and $p_2(x)$ respectively, thus (II.15) is given by (after substitution (II.4) and (II.8) into (II.15))

$$P_x(x) = k\frac{b^\nu}{\Gamma(\nu)}\int_0^\infty \frac{y^{\nu-1}}{y+p_n}\exp(-\frac{x}{y+p_n})\exp(-by)dy + \frac{(1-k)\beta^\alpha}{\Gamma(\alpha)}\int_0^\infty \frac{y^{-\alpha-1}}{p_n+y}\exp(-\frac{x}{p_n+y})\exp\left(-\frac{\beta}{y}\right)dy$$

(II.20)

where, $\theta = [\,k, b, \nu, \alpha, \beta, p_n]$. Also, the resulting CCDF from a mixture of *K* and GP plus noise models is given by

$$CCDF_{Pareto}^{K}(T) = k\frac{b^\nu}{\Gamma(\nu)}\int_0^\infty y^{\nu-1}\exp\left(-\frac{T}{y+p_n}\right)\exp(-by)dy + \frac{(1-k)\beta^\alpha}{\Gamma(\alpha)}\int_0^\infty y^{-\alpha-1}\exp\left(-\frac{T}{p_n+y}\right)\exp(-\beta/y)dy \quad \text{(II.21)}$$

II.4 Nelder-Mead algorithm

In this section, we present the N-M algorithm for unconstrained optimization. This algorithm is based on the iterative update of a simplex. The N–M method is a non-linear optimization algorithm that was published by John Nelder and Mead in 1965. The method is described for the minimization of a function of *n* variables, which depends on the comparison of function values at the (*n* + 1) vertices of a general simplex, followed by the replacement of the vertex with the highest value by another point. The simplex adapts itself to the local landscape, and contracts on to the final minimum. The method is shown to be effective and computationally compact [54]. This method is a local search method developed for nonlinear and deterministic optimization without the need for gradient information. The N-M algorithm can be implemented based on four basic procedures: reflection, expansion, contraction, and shrinkage depending on the values at the vertices and center of the simplex. To be more specific, n-dimensional simplex is defined as the convex hull of *n* + 1 vertices. If any vertex of non degenerate simplex is taken as the origin, then the rest *n* vertices define vector directions that span the n-dimensional vector space. The extreme point of the simplex with the worst function value is moved, and the reflected point is generated. On one hand, if the reflected point is better than the best point, the expansion of the simplex is performed in one or another direction to take larger steps. On the other hand, a contraction step will be taken when the reflected point is the worst point in the new simplex, restricting the search on a smaller region. If the earlier worst point is better than the contracted one, the shrinkage step is performed. Through these operations, the simplex can improve itself and come closer and closer to a local optimum point sequentially [55]. In our application, the N-M algorithm was used as a method for minimizing a real-valued function $f(x)$ for $x \in \Re^n$ where four scalar parameters must be specified to define a complete method: coefficients of *refection* (ρ), *expansion* (χ), *contraction* (γ), and *shrinkage* (σ). We have six unknown parameters to be optimized. The residuals of an adequate tail fitting regions of the theoretical CCDFs with real data are optimized. The basic steps that described the N-M algorithm are given by the flowchart of Figure II.1.With the fixed parameters $\rho = 1$, $\chi = 2$, $\gamma = 1/2$ and $\sigma = 1/2$ [36]

II. 5 Modeling assessment using IPIX data

The capabilities of the proposed mixture models given in (II.15) to fit the real PDFs and CCDFs, for various sets are investigated in this section. This modeling performance is assessed using real-world IPIX lake clutter. The lake-clutter data we processed were collected at Grimsby, Ontario, with the McMaster University IPIX radar. IPIX is experimental X-band search radar, capable of dual polarized and frequency agile operation [56]. As in references [5, 8], we focus our analysis on the datasets 84, 85 and 86 which correspond to the range resolutions 30m, 15m and 3m respectively. Characteristic features of the IPIX radar are summarized in Table II. 1. The radar site was located at east of the “Place Polonaise” at Grimsby, Ontario (Latitude 43:2114±N, Longitude 79:5985±W), looking at lake Ontario from a height of 20 meter (m). The nearest shore on the far side of the lake is more than 20 Km away. The data of the Grimsby database are stored in 222 files, as 10 bits integers.

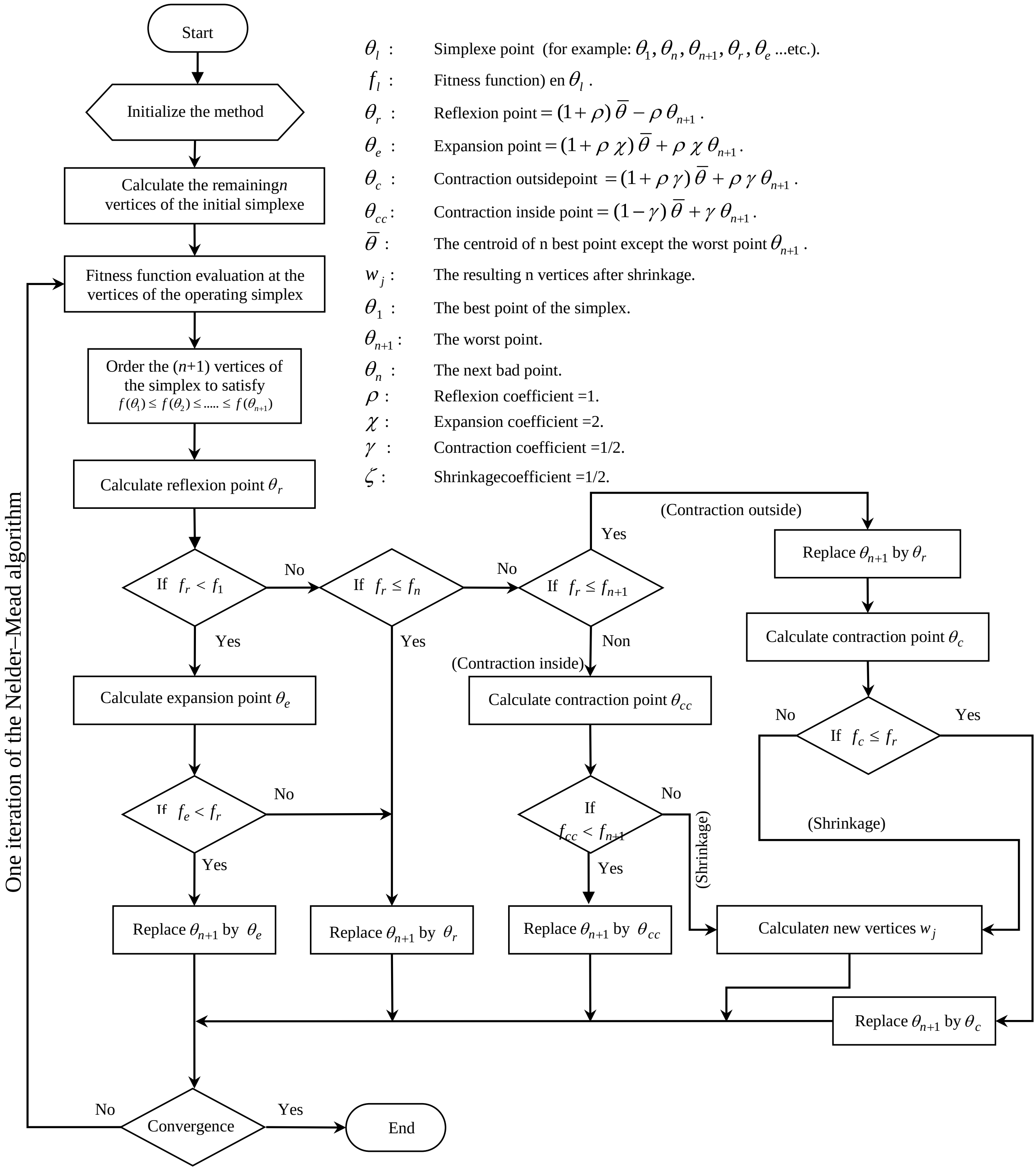

Figure II.1: Flowchart of the Nelder-Mead algorithm [37, 57]

Table II.1: Data description of IPIX radar [5, 8]

Dataset	**19980204_220849 (file 84)**	**19980204_223220 (file 85)**	**19980204_223506 (file 86)**
Date and time	02/04/1998 22:08:49	02/04/1998 22:32:20	02/04/1998 22:35:06
Number of range cells	34	34	34
Start range	3201 m	3201 m	3201 m
Range resolution	30m	15m	3m
Number of sweeps	60000	60000	60000
Sample per cell	60000	60000	60000
PRF	1 KHz	1 KHz	1 KHz
RF-frequency	9.39 GHz	9.39 GHz	9.39 GHz
Radar and wave geometry	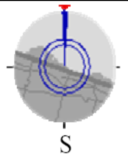	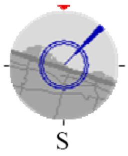	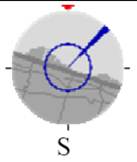

There are co-polarizations, HH and VV (Lpol), and cross-polarizations, HV and VH (Xpol), coherent reception, leading to a quadruplet of *I* and *Q* values for co-pol and cross-pol. In this section, the experimental modeling analysis was carried out for HH and VV antenna polarizations, 3 m, 15 m and 30 m range cell resolutions. During the recordings, the radar was transmitting with a pulse-repetition frequency (PRF) of 1000 Hz and a pulse length of 0.06 μs. The received IPIX data is treated by the arrival order and registered in a (60000x34) matrix where 34 denotes the number of range cells and 60000 is the number of pulses. Because parameter estimation of compound Gaussian models can not be obtained using low sample sizes, the proposed mixture models were validated using 60000 recorders rather than 34 range samples. High resolution sea clutter depends on both azimuth resolutions which are related to the beam width and range resolution. In cases of *d*=3m, *d*=15m and *d*=30m, the pulse duration (i.e., sampling time) has three different values where the grazing angle is fixed at a low value. Thus, these data does not have a connection with the grazing angle.

In order to investigate the statistical properties of the data, we compare the empirical PDF and CCDF of the data with their theoretical mixture models, in the case of single look data. Fitting with multilook data using for example 10 to 20 cells is not possible using the proposed theoretical distributions. Models providing the tail fitting to real data are important in radar detection applications. Thus, 1000 independent samples are not sufficient to fit the tail of the corresponding PDFs and CCDFs. Usually, 10^5 samples are needed for a desired CCDF value of 10^{-3}. Each range cell, 60000 measurements are therefore necessary to compare the tail fitting of the different models.

The following experimental procedure focuses firstly on the parameter estimation found by the N-M algorithm and secondly on the validation of the mixture models using the real data described previously. The MSE values are calculated from fitted and empirical CCDFs curves. According to these values which are obtained from specific range of the CCDFs between 10^{-3} and 10^{-2}, the proposed mixture models give lower values allowing best tail fitting as several scenes will show. The optimal estimates of the various models parameters as well as the MSE values are illustrated in Tables II.2 and II.3.

In the case of a resolution of 3m, HH polarization, 17th cell range; better modeling performance is obtained by the *K* plus GP and CIG plus GP CCDFs as depicted in Figure II.2. Note that, the *K* distribution plus noise does not fit accurately the tail of empirical data. If another study based on the use of the same resolution with VV polarization, but with the 9th cell range, the same pattern is observed in Figure II.3. The *K* plus GP and CIG plus GP give the lowest values of MSE. From these modeling experiments, it is pinpointed out that a mixture model constructed by the sum of the CIG, *K*, and GP distributions with noise is mostly an accurate statistical model of IPIX data, but it requires more computational time due to the number of estimated parameters.

In the case of a resolution of 15m, a VV polarization are considered with 32th cell range, the theoretical mixture models CIG plus GP and *K* plus GP have quasi-similar results with the empirical CCDFs as shown in Figure II.4. If another study based on the use of the same resolution with HH polarization, 4th cell range, the CIG + *K*, and GP + *K* provide lower values of MSE with respect to the other models as shown in Figure II.5.

For a resolution of 30m, HH polarization, 19th cell range, the PDFs and the CCDFs curves are depicted in Figure II.6. It is clearly seen from this experiment that a mixture model constructed by the CIG plus *K* distributions provides the smallest value of MSE which means the best fit to empirical data. If we use the same resolution with VV polarization, and 8th cell range, Figure II.7 illustrates the different PDFs and CCDFs for the all considered models. In this experiment, it can also be seen that the tail of the proposed mixture models (GP plus *K*) leads to the best fit.

Finally, the results obtained by the proposed mixture models are also assessed against those obtained by the existing KK model with thermal noise [11]. To this effect, we used the same PCFE based method given in Figure II.1 to compute the KK clutter plus noise parameters. For this, the corresponding PDF of the KK model with thermal noise is given by

$$p_x(x) = k\,\frac{b^{\nu}}{\Gamma(\nu)}\int_0^{\infty}\frac{y^{\nu-1}}{y+p_n}\exp\left(-\frac{x}{y+p_n}\right)\exp(-by)\,dy$$

$$+\frac{(1-k){b_1}^{\nu_1}}{\Gamma(\nu_1)}\int_0^{\infty}\frac{y^{\nu_1-1}}{y+p_n}\exp\left(-\frac{x}{y+p_n}\right)\exp(-by)\,dy \qquad \text{(II.22)}$$

where, $\theta = [\mathrm{k}, \mathrm{b}, \nu, \mathrm{b}_1, \nu_1, \mathrm{p}_\mathrm{n}]$

The corresponding CCDF of the KK model plus noise is given by

$$CCDF_K^K(T) = k\,\frac{b^{\nu}}{\Gamma(\nu)}\int_0^{\infty} y^{\nu-1}\exp\left(-\frac{T}{y+p_n}\right)\exp(-by)\,dy$$

$$+\ \frac{(1-k){b_1}^{\nu_1}}{\Gamma(\nu_1)}\int_0^{\infty} y^{\nu_1-1}\exp\left(-\frac{T}{y+p_n}\right)\exp(-by)\,dy \qquad \text{(II.23)}$$

Table II.4 illustrates the MSE values as well as the optimal estimates of the various models parameters. For VV polarization, resolution of 30m and 19th cell range, the PDFs and the CCDFs curves are depicted in Figure II.8. It is clearly seen from this study that a mixture model constructed by the CIG plus GP distributions provides the smallest value of MSE which means the best fit to empirical data. If the HH polarization is used with a resolution of 15m and the 10th cell range, all proposed models with noise as shown in Figure II.9 outperform the KK model and achieve almost the same tail fitting to real data with a slight superiority of the CIG plus *K* that is illustrated by the smallest value of the MSE (Tables II.4). Now, in the case of a resolution of 3m, HH polarization and 17th cell range, the estimated CIG plus GP CCDF as presented in Figure II.10 offers a goodness of fit compared to the obtained KK curve.

Table II.2: Estimated parameters of K and Pareto plus noise models for HH and VV polarizations

Model	Parameters	VV30 m 8th cell	HH30m 19th cell	VV15m 32th cell	HH15m 4th cell	HH3m 17th cell	VV3m 9th cell
***K*+noise**	$\hat{v}$	3.1302	0.2599	0.1311	1.8891	0.1000	0.1000
	b	4.5160	0.1105	0.0967	3.2661	0.0728	0.1709
	$\hat{\sigma}$	0.0000	0.1000	0.1000	0.0000	0.3166	0.7370
	MSE (dB)	**-4.7240**	**-5.5221**	**6.1445**	**5.3521**	**-5.7584**	**4.848**
Pareto +noise	$\hat{\alpha}$	0.6677	1.1005	0.1189	0.1329	7.1264	0.2376
	$\hat{\beta}$	0.3658	0.1205	0.0819	0.0686	0.2921	0.4774
	$\hat{\sigma}$	0.5766	0.0954	0.4403	0.3596	0.4727	0.6582
	MSE (dB)	**-4.7244**	**-5.2537**	**- 6.1455**	**-5.1837**	**-5.7713**	**-4.803**

Table II.3: Estimated parameters of mixture models for HH and VV polarizations

Model	Parameters	HH30m 19th cell	VV30 m 8th cell	VV15m 32th cell	HH15m 4th cell	HH3m 17th cell	VV3m 9th cell
CIG+*K* with noise	$\hat{\lambda}$	0.4855	0.6892	1.6354	1.0048	1.0725	0.1000
	$\hat{\mu}$	15.6892	0.1172	0.9238	2.0632	0.5922	1.3673
	κ	0.6466	0.4765	0.2343	0.2597	0.9757	0.0000
	$\hat{v}$	0.4087	0.6677	0.1189	0.1329	7.1264	0.2376
	$\hat{b}$	0.1498	0.3658	0.0819	0.0686	0.2921	0.4774
	$\hat{\sigma}$	0.3950	0.5766	0.4403	0.3596	0.3616	0.6902
	MSE (dB)	**-6.4875**	**-4.6758**	**-5.6832**	**-5.7971**	**-5.6434**	**4.878**
CIG+GP with noise	$\hat{\lambda}$	0.5370	1.0605	0.8444	1.0556	0.9649	0.9483
	$\hat{\mu}$	0.7762	1.4330	2.7913	0.1844	0.7570	0.8067
	κ	0.5259	0.8642	0.1053	0.3783	0.0000	0.7068
	$\hat{\alpha}$	0.7278	1.2748	1.2668	1.0198	1.5067	0.7037
	$\hat{\beta}$	0.8462	1.0000	0.6443	1.0000	0.4164	0.6455
	$\hat{\sigma}$	0.1000	0.0018	0.2500	0.1090	0.2711	0.2477
	MSE (dB)	**-6.1485**	**-4.7810**	**-6.2621**	**-4.7581**	**-5.8934**	**5.031**
***K*+GP with noise**	$\hat{v}$	0.2990	0.9194	0.1000	0.2021	0.2911	0.1583
	$\hat{b}$	1.9826	0.5532	0.3699	0.1628	0.7736	0.0723
	κ	0.4407	0.3171	0.0151	0.8283	0.0000	0.1601
	$\hat{\alpha}$	0.8815	1.6305	1.2490	0.7581	1.4422	2.8539
	$\hat{\beta}$	1.0000	1.0000	0.6774	1.0000	0.3532	1.0000
	$\hat{\sigma}$	0.1384	0.2153	0.2269	0.3359	0.5641	0.5561
	MSE (dB)	**-5.6246**	**-4.8006**	**-6.2348**	**-5.5571**	**-5.8783**	**-5.035**

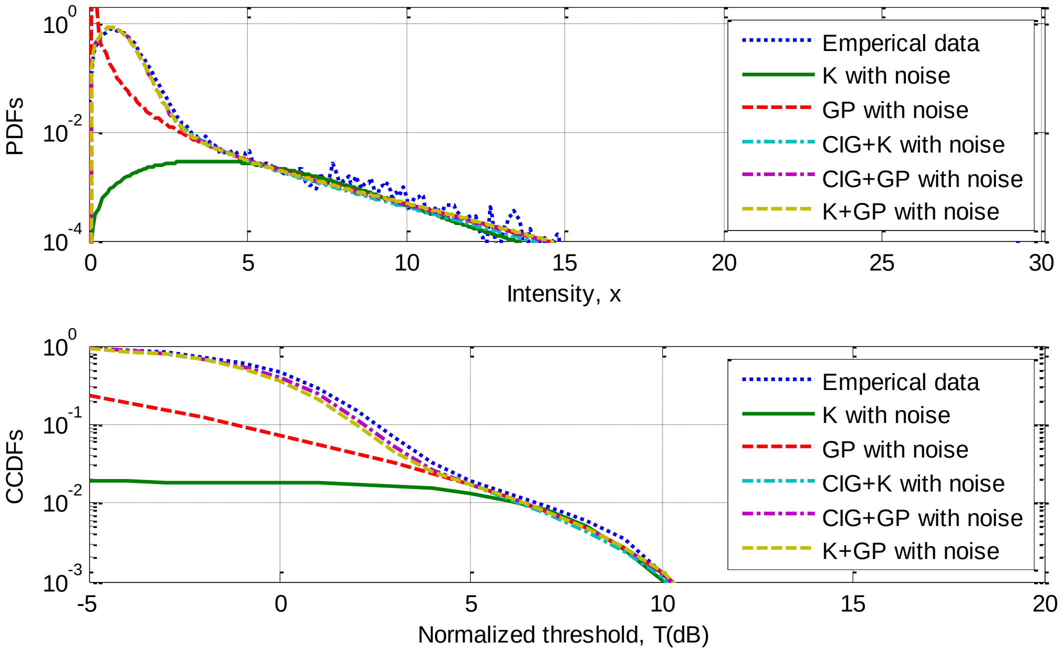

Figure II.2: Fitted PDFs and fitted CCDFs of mixture models for HH polarization, resolution of 3m and 17th cell range.

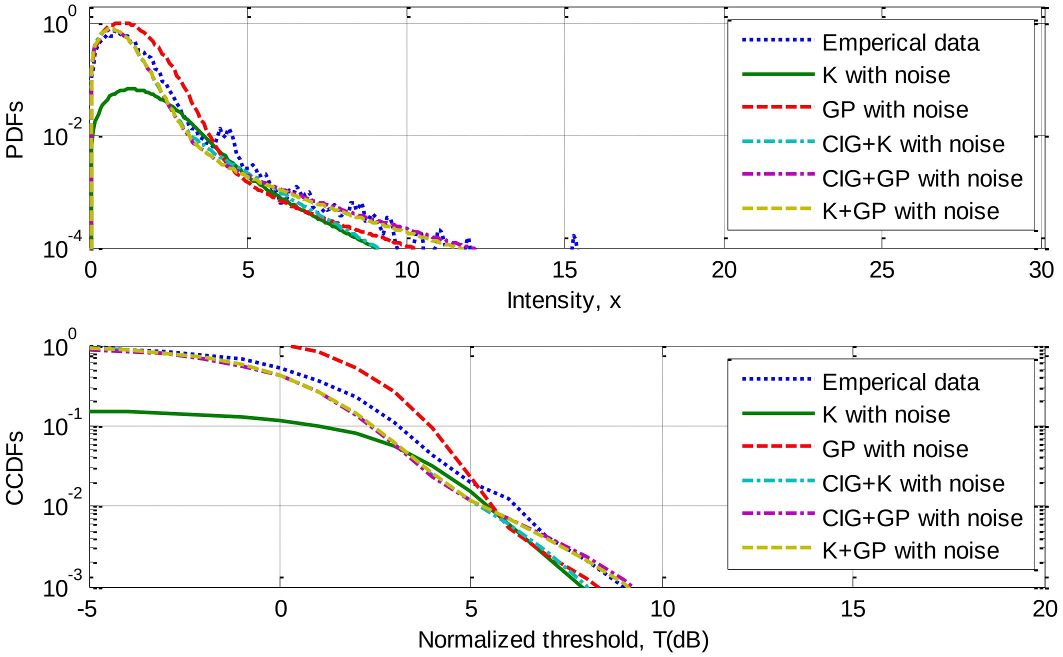

Figure II.3: Fitted PDFs and fitted CCDFs of mixture models for VV polarization, resolution of 3m and 9th cell range.

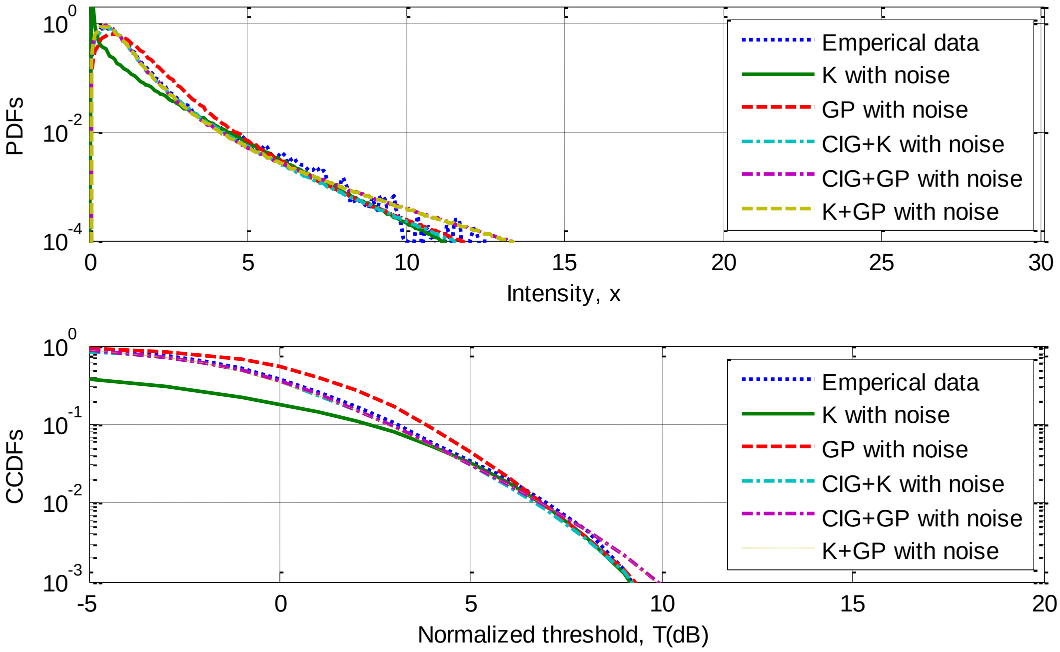

Figure II.4: Fitted PDFs and fitted CCDFs of mixture models for VV polarization, resolution of 15m and 32th cell range.

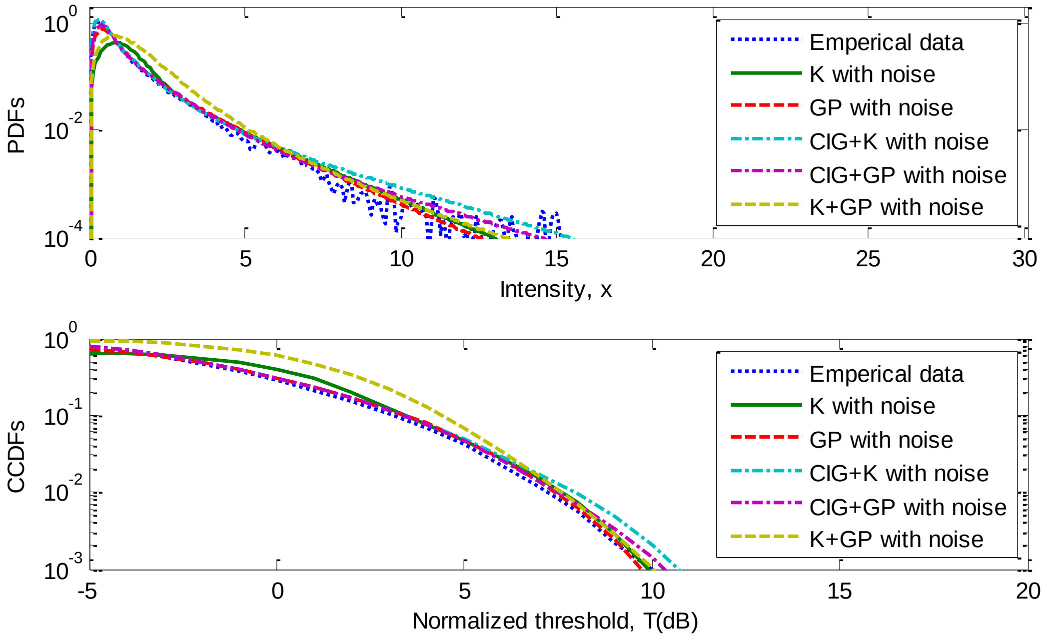

Figure II.5: Fitted PDFs and fitted CCDFs of mixture models for HH polarization, resolution of 15m and 4th cell range.

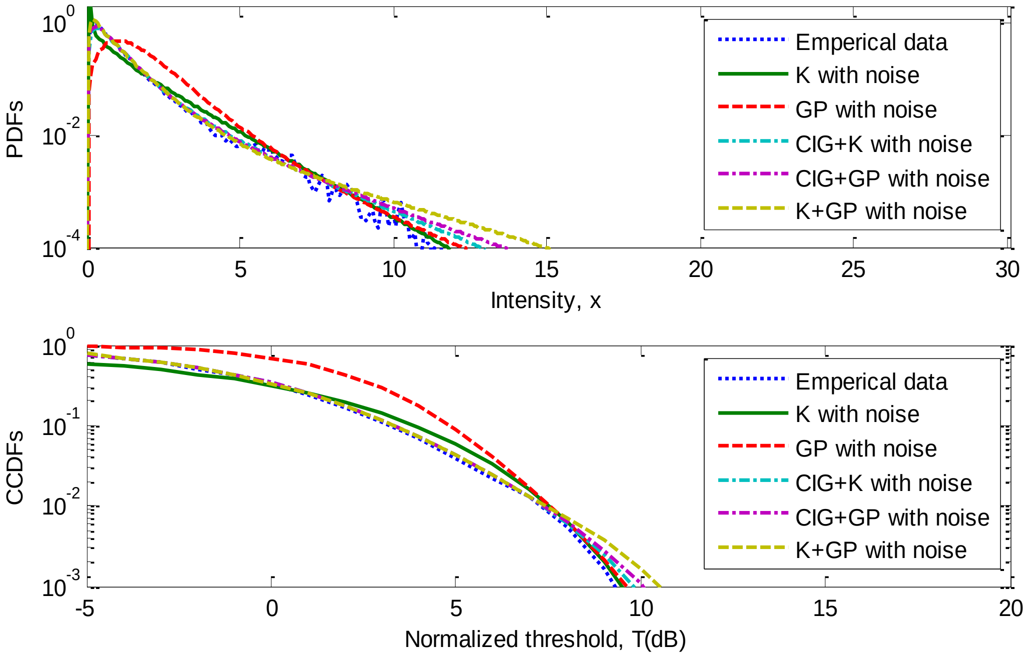

Figure II.6: Fitted PDFs and fitted CCDFs of mixture models for HH polarization, resolution of 30m and 19th cell range.

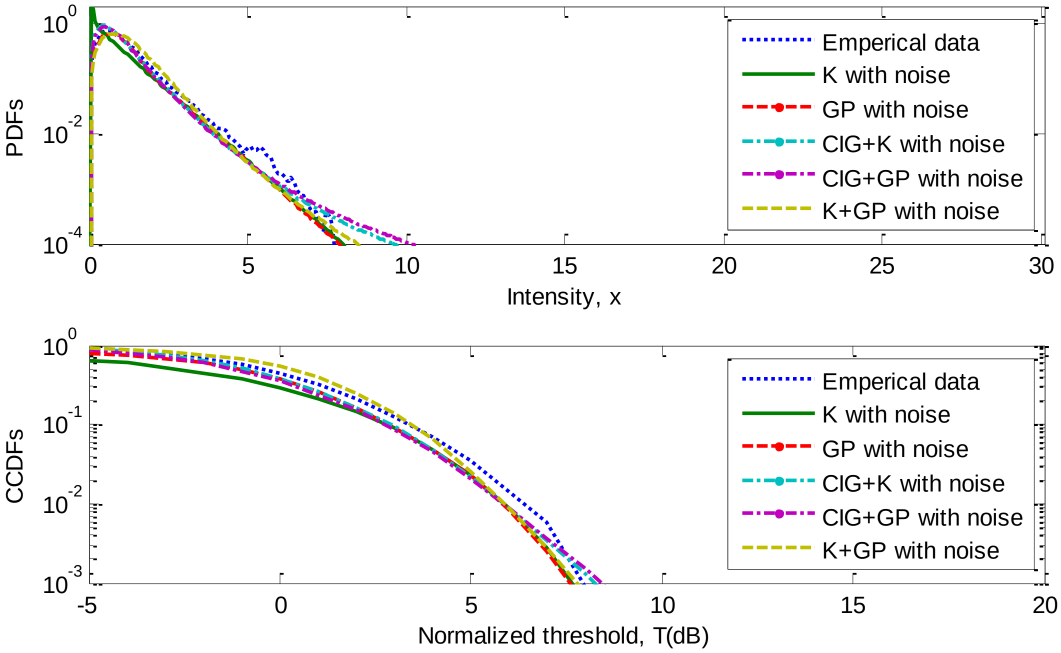

Figure II.7: Fitted PDFs and fitted CCDFs of mixture models for VV polarization, resolution of 30m and 8th cell range.

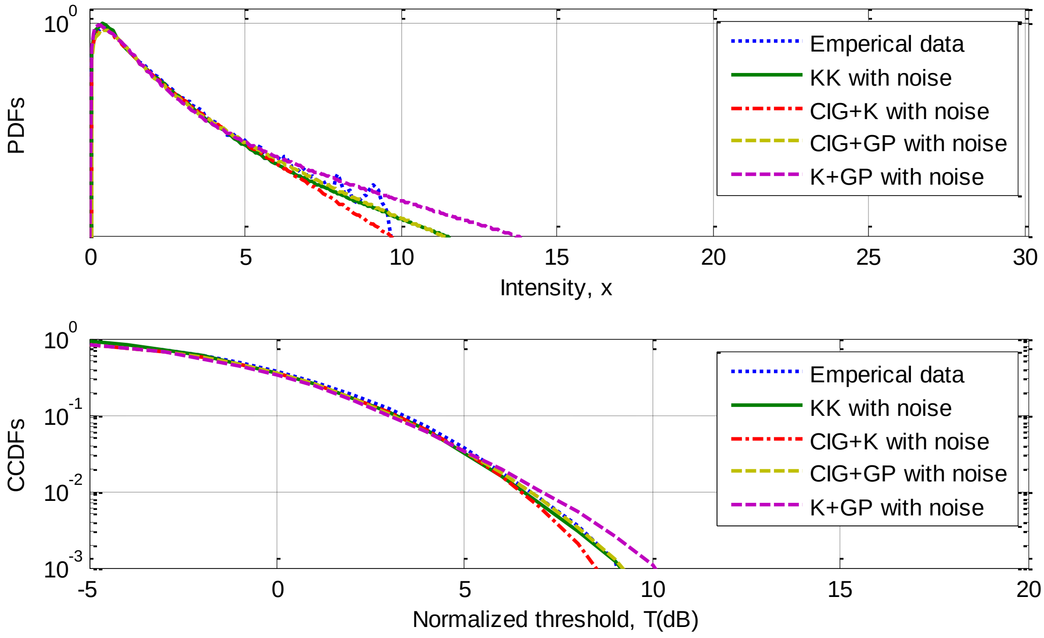

Figure II.8: Fitted PDFs and fitted CCDFs of mixture models for VV polarization, resolution of 30m and 19th cell range.

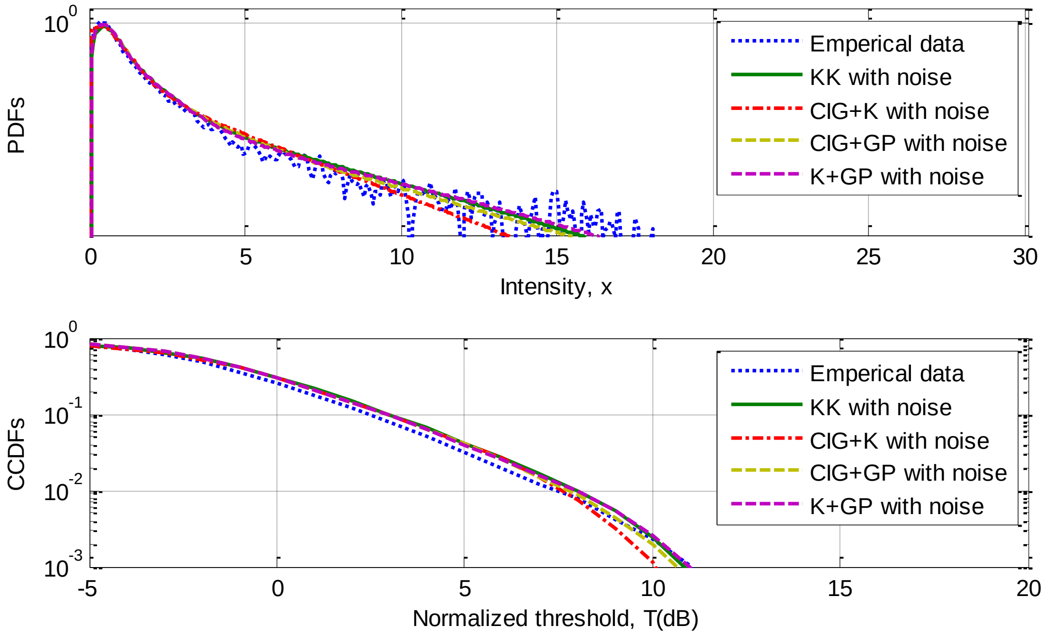

Figure II.9: Fitted PDFs and fitted CCDFs of mixture models for HH polarization, resolution of 15m and 10th cell range.

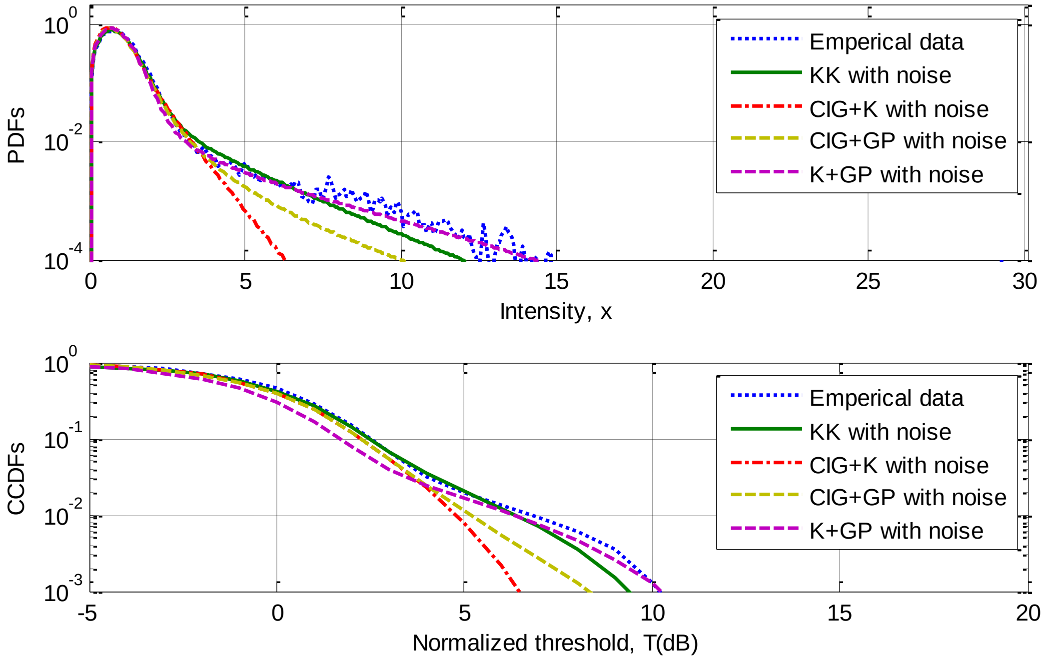

Figure II.10: Fitted PDFs and fitted CCDFs of mixture models for HH polarization, resolution of 3m and 17th cell range.

Table II.4: Estimated parameters of mixture models for HH and VV polarizations
$\hat{\nu}$

Distribution	b Parameters	VV, 30m, 19thcell	HH, 15m, 10th cell	HH, 3m, 17thcell
KK **With noise**	$\hat{\nu}$	1.1460	0.1254	0.2725
	b	0.2147	0.0551	0.9996
	κ $\hat{\sigma}$	0.8358	0.2957	0.0019
	1	1.5717	0.8931	0.7037
	$\hat{\lambda}$1	1.0000	0.5739	0.6455
	$\hat{\mu}$	0.0460	0.3859	0.6330
	MSE (dB)	**-5.7088**	**-5.4479**	**-4.304**
CIG+*K* With noise	$\hat{\nu}$	0.9362	1.1341	0.8181
	$\hat{b}$	1.1664	0.7402	0.7753
	κ $\hat{\sigma}$	0.8358	0.2957	0.7388
		1.1460	0.1254	0.8826
	$\hat{\lambda}$	0.2147	0.0551	0.8089
	$\hat{\mu}$	0.0460	0.3859	0.6330
	MSE κ (dB)	**-5.5441**	**-5.7499**	**-4.2484**
CIG+GP With noise	$\hat{\alpha}$	0.8729	0.9962	0.9483
	$\hat{\beta}$	2.4484	0.1109	0.8067
	$\hat{\sigma}$	0.5220	0.3889	0.7068
		1.5717	0.8931	0.7037
	$\hat{\nu}$	1.0000	0.5739	0.6455
	$\hat{b}$	0.0672	0.3206	0.2046
	MSE κ (dB)	**-7.2766**	**-5.7489**	**-5.1298**
***K*+GP With noise**	$\hat{\alpha}$	0.4945	0.3440	0.2687
	$\hat{\beta}$	1.0225	0.7993	3.3365
		0.3426	0.7225	0.7587
		1.2171	0.7481	0.4259
		1.0000	1.0000	0.0545
		0.2181	0.3536	0.6688
	MSE (dB)	**-5.5134**	**-5.5104**	**-4.4833**

II.7 Conclusion

The modeling of high resolution sea clutter has been discussed and the mixture distribution with different random textures has been proposed. The additive thermal noise has been incorporated to provide an appropriate theoretical model for real sea-clutter statistics collected by IPIX, X-band radar. The proposed model is based on the sum/mixture of two different compound Gaussian distributions with noise. Accordingly, the CIG the *K* and the GP plus noise distributions are combined to achieve better tail fitting. The curve fitting method based on the N-M optimizer is used to estimate the parameters of the mixture models. Experimental results showed that the proposed models provide the best fit of real data for several scenes compared to the standard *K* plus noise, GP plus noise and KK plus noise distributions.

3

Estimators of CGIG Clutter plus Noise Parameters

Chapter outline:

III.1 Introduction

Estimation theory is a branch of statistics that deals with estimating the values of parameters based on measured empirical data that has a random component. The parameters describe an underlying physical setting in such a way that their value affects the distribution of the measured data. An estimator attempts to approximate the unknown parameters using the measurements. In estimation theory, the probabilistic approach assumes that the measured data is random with probability distribution dependent on the parameters of interest. Commonly used estimators (estimation methods) and topics related to them include [58]:

- Maximum likelihood estimators (MLE)
- Bayes estimators.
- Method of moment’s estimators (MOME).
- Cramér-Rao bound.
- Least squares.

- Bayes least squared error (BLSE).
- Maximum a posteriori (MAP).
- Minimum variance unbiased estimator (MVUE).
- Nonlinear system identification.
- Best linear unbiased estimator (BLUE).
- Unbiased estimators.
- Particle filter.
- Markov chain Monte Carlo (MCMC).
- Kalman filter and its various derivatives.
- Wiener filter.

In radar applications, estimation of clutter model parameters forming the background level, in which the target of interest is embedded, is an essential part in CFAR detection schemes. For independent returns, numerous estimators have been designed to deal with estimation concerns of CG models with and without thermal noise [14-25]. For noiseless case, MLE, MOME, [zlog(z)] and artificial intelligence based methods have been proposed when both accuracy and computing time are concerned to estimating *K*, Pareto type II (GP) and CGIG radar clutter parameters [23-25]. Since the reflected samples are unavoidably embedded in thermal system noise, their measured values are randomly distributed in integral form, so that the noise power must be estimated after giving the estimates of the scale and the shape parameters. Despite the mathematical complexities, researchers seek for the generalization of the above estimators [14-21].

In the following, the CGIG clutter plus noise PDF with its expression of moments is given in Section III.2. Section III.3 describes existing definite numerical integration methods of a given function in particular the Gauss quadrature method. Mathematical stages for deriving the HOME, CNIOME and CMLE estimators of CGIG clutter plus noise parameters are presented in Section III.4. Using simulated and real data, Section III.5 investigates estimation performances of the proposed methods. Finally, conclusions are outlined in Section III.6.

III. 2 CGIG model with thermal noise

CG models are widely used as accurate and tractable distributions for the scattered returns generated by the reflection of the radar incident waveform on the sea surface [59, 60].

The CG models consist of a rapidly varying speckle component modulated by a slowly varying texture component. If *N* non-coherently integrated pulses, $z_j = \sum_{i=1}^{N} x_{ij}$, *j=1,..., M* is considered, the PDF for the clutter power is given by [15].

$$p_Z\left(z \middle| p_n, N\right) = \int_0^\infty p_Z\left(z \middle| y, p_n, N\right) p_Y\left(y\right) dy \qquad \text{(III.1)}$$

where *M* is the sample size and $p_n = 2\sigma^2$ denotes the noise power. Thus, if radar echoes are corrupted with zero-mean white Gaussian noise with a variance σ^2, the speckle component which is a sum of coherent Gaussian random variables follows a gamma distribution with shape parameter, *N* and clutter power, *y* [20].

$$p_Z\left(z \middle| y, p_n, N\right) = \frac{z^{N-1}}{\left(y + p_n\right)^N \Gamma(N)} \exp\left(-\frac{z}{y + p_n}\right) \qquad \text{(III.2)}$$

The CGIG model with thermal noise is obtained by making the random variable, *Y*, fluctuates according to the inverse Gaussian law given by (II.11)with shape parameter, λ and clutter power μ . Values of λ typically belong to [0.1, ∞], while spiky clutter corresponds to values of $\lambda \in [0.1,\ 1]$ and the exponential distribution is attained for $\lambda \to \infty$. In the following, the texture '*y*' is assumed constant across all *N* pulses. Substituting (III.2) and (II.11) into (III .1) yield

$$p_Z\left(z \middle| p_n, N\right) = \sqrt{\frac{\lambda}{2\pi}} \frac{e^{\lambda/\mu} z^{N-1}}{\Gamma(N)} \int_0^\infty \frac{y^{-3/2}}{\left(y + p_n\right)^N} \exp\left(-\frac{\lambda y}{2\mu^2} - \frac{\lambda}{2y} - \frac{z}{y + p_n}\right) dy \qquad \text{(III.3)}$$

Since the evaluation of the integral in (III .3) is quite difficult to obtain, numerical integration like conventional, Monte-Carlo or Gauss quadrature methods can be used [20, 61, 62]. For convenience, we shall use the notation $\left\langle z^r \right\rangle$ to denote moment of order *r*. With this notation, moment or expectation of order *r* is computed from (III .3) as

$$\begin{aligned} \left\langle z^r \right\rangle &= \int_0^\infty z^r p_Z\left(z \middle| p_n, N\right) dz \\ &= \int_0^\infty \frac{\lambda^{1/2}}{\sqrt{2\pi} y^{3/2}} \exp\left(-\lambda \frac{(y-\mu)^2}{2\mu^2 y}\right) \left[\int_0^\infty z^r \frac{z^{N-1}}{\left(y + p_n\right)^N \Gamma(N)} \exp\left(-\frac{z}{y + p_n}\right) dz\right] dy \end{aligned} \qquad \text{(III.4)}$$

The result $\int_0^\infty x^{a-1}\exp(-bx)dx = \frac{\Gamma(a)}{b^a}$ in [63, 64] is used to evaluate the integral in brackets of (III.4) to yield

$$\langle z^r \rangle = \sqrt{\frac{\lambda}{2\pi}} e^{\lambda/\mu} \frac{\Gamma(N+r)}{\Gamma(N)} \int_0^\infty y^{-3/2} (y+p_n)^r \exp\left(-\frac{\lambda}{2\mu^2} y - \frac{\lambda}{2y}\right) dy \qquad \text{(III.5)}$$

The left hand side of (III.5) is estimated by its sample counterpart, $\frac{1}{M}\sum_{i=1}^{M} z_i^r$ and the clutter to noise ratio is given by $CNR = \frac{\mu}{p_n}$. Non-integer order moments of (III.5) will be handled in Section III.4 to derive the HOME, CNIOME and CMLE based approaches for parameter estimation of CGIG clutter plus noise.

III. 3 Numerical integration methods

Numerical integration is the approximate computation of a definite integral using numerical techniques. Quadrature, or numerical integration, is therefore the process of approximating the definite integral of a given function. Mathematicians and scientists are sometimes confronted with definite integrals which are not easily evaluated analytically, even a function *f*(*x*) is known completely. To overcome this difficulty, numerical integration involves replacing an integral by a sum. There are a wide range of methods available for numerical integration. The most straightforward numerical integration technique uses the Newton-Cotes formula, which approximate a function tabulated at a sequence of regularly spaced intervals by polynomials of various degrees. If the endpoints are tabulated, then the 2- and 3-point formulas are called the trapezoidal rule and Simpson’s rule, respectively [20, 65]. The 5-point formula is called Boole’s rule. A generalization of the trapezoidal rule is Romberg integration, which can yield accurate results for relatively few function evaluations. If the integrand is known analytically, rather than being tabulated at equally spaced intervals, the best numerical integration method is Gaussian quadrature.

By cleverly choosing the abscissas at which to evaluate the function, Gaussian quadrature produces the most accurate approximations possible for a given number of function evaluations. However, given the speed of modern computers, the additional complication of Gaussian quadrature often makes it less convenient than simply brute-force calculating twice as many points on a regular grid (which also permits the already computed values of the function to be reused).

Recall that the definite integral $\int_a^b f(x)dx$ is the area under the curve $y=f(x)$ between the limits $x=a$ and $x=b$.

$$\int_a^b f(x)dx = \lim_{n\to\infty}\sum_{i=0}^{n} f(\alpha_i)(x_i - x_{i-1}) \tag{III.6}$$

where $x_{i-1} \le \alpha_i \le x_i$, $a = x_0<x_1< \ldots <b=x_n.$ Typically, this approximation takes the form of a weighted sum of function evaluations. In the following, we will summarize some quadrature methods used in most engineering applications.

III. 3.1 Equidistant formula

Equidistant integration formula evaluates the integrand at points that have a fixed distance h from their nearest neighbors. In other words, if we integrate from a to b, the nodes where we evaluate the function are $x_i = a+ih$, $i=0, \ldots, n$, $h = \frac{b-a}{n}$ and n is the number of intervals (i.e., the number of nodes minus 1).

(i) Left and right Riemann sums rule (rectangular rule)

Let us divide the interval into n subintervals of length h, and each subinterval choose $\alpha_i = x_{i-1}$(left Riemann sum), or $\alpha_i = x_i$(right Riemann sum) as shown in Figures III.1-a and b.

$$\begin{cases} \int_a^b f(x)dx \approx h(y_0 + y_1 + \ldots + y_{n-1}), & \text{Left Riemann sum} \\ \int_a^b f(x)dx \approx h(y_1 + y_2 + \ldots + y_n), & \text{Right Riemann sum} \end{cases} \tag{III.7}$$

(ii) Trapezoidal rule

The function of each interval is approximated by a linear function. It thus gives the exact result for constant or linear functions, as can be seen from the error (see Figure III.2).

$$
\begin{aligned}
\int_{x_0}^{x_n} f(x)dx &= \sum_{k=0}^{n-1} \int_{x_k}^{x_{k+1}} f(x)dx \\
&= \sum_{k=0}^{n-1} \frac{h}{2}\left[\mathrm{f}(\mathrm{x}_{\mathrm{k}}) + \mathrm{f}(\mathrm{x}_{\mathrm{k+1}})\right] + \mathrm{O}(\mathrm{h}^3 f''(\xi)) \qquad \text{(III.8)} \\
&= h\frac{f_0 + 2f_1 + \ldots + 2f_{n-1} + f_n}{2} + \mathrm{O}(\mathrm{h}^3 f''(\xi))
\end{aligned}
$$

Where $h = x_{k+1} - x_k$ and $x_0 < \xi < x_n$

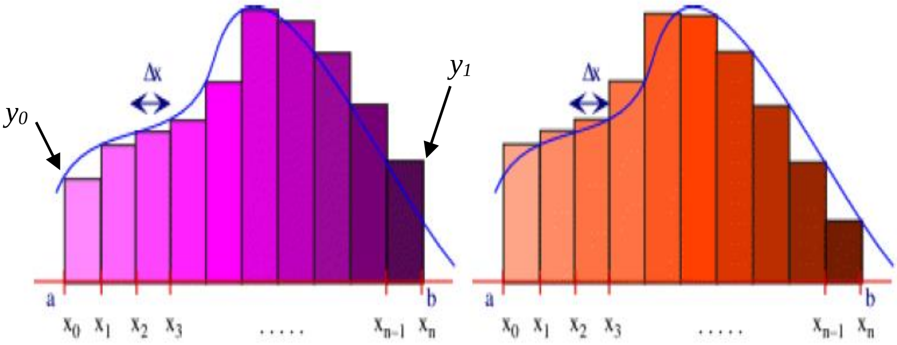

(a) (b)

Figure III. 1: Left and right Riemann quadrature method.
(a) Left Riemann sum; the left side of each rectangle matches the height of the graph.
(b) Right Riemann sum; the right side of each rectangle matches the height of the graph.

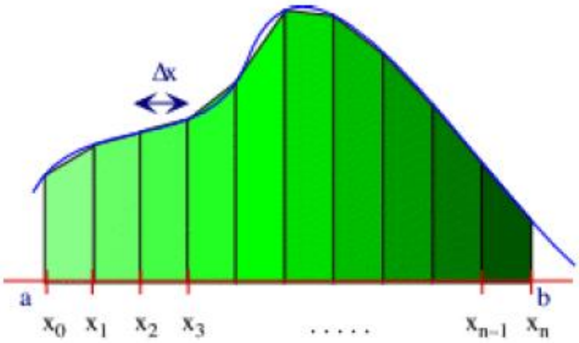

Figure III. 2: Trapezoidal quadrature method.

(iii) Simpson's rule

In order to get better results with respect to the above integration methods, Simpson's rule approximates the function on each interval by a parabolic function. It gives the exact result even for arbitrary polynomials of third order (see Figure III.3).

$$\begin{aligned}\int_{x_0}^{x_n} f(x)dx &= \sum_{k=0}^{(n-1)/2} \int_{x_{2k-1}}^{x_{2k+1}} f(x)dx \\ &= \sum_{k=0}^{(n-1)/2} \frac{h}{3}\left[\mathrm{f}(\mathrm{x}_{2k-1}) + 4\mathrm{f}(\mathrm{x}_{2k}) + \mathrm{f}(\mathrm{x}_{2k+1})\right] + \mathrm{O}(\mathrm{h}^5 f^{(4)}(\xi)) \qquad \text{(III.9)} \\ &= h\frac{f_0 + 4f_1 + 2f_2 + 4f_3 + \ldots + 2f_{n-2} + 4f_{n-1} + f_n}{3} + \mathrm{O}(\mathrm{h}^5 f^{(4)}(\xi))\end{aligned}$$

where $h = 2x_{2k+1} - x_{2k} = x_{2k} - x_{2k-1}$ and $n > 3$ is an odd integer number.

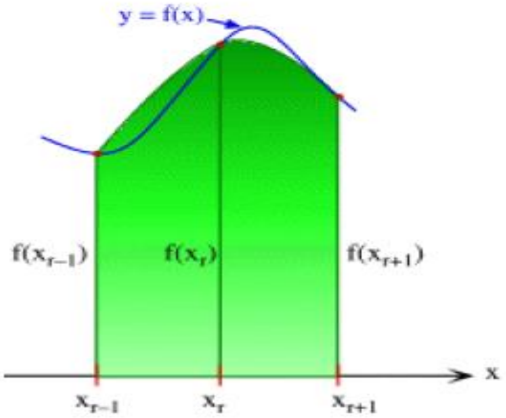

Figure III. 3: Simpson’s quadrature method.

III. 3. 2 Gaussian quadrature formulas

Gaussian quadrature formulae, which have non-uniformly spaced grid points, are very efficient for known smooth functions. The main idea is to choose not only the weighting coefficients (weight factors) but also the locations (abscissas) where the function *f*(*x*) is evaluated. As a result, Gaussian quadrature yields twice as many places of accuracy as that of equal space formula with the same number of function evaluations. In the evaluation of an integral on the interval *a* and *b*, it is not necessary to evaluate *f*(*x*) at the endpoints, i.e. at *a* and *b*, of the interval. Gauss quadrature based on arbitrary and orthogonal polynomials are given below [64, 65].

The general quadrature formula approximates an integral by a sum of the following form

$$\int_a^b w(x) f(x)dx = \sum_{i=1}^{n} w_i f(x_i) + R_n \qquad \text{(III.10)}$$

where *w*(*x*) is a weight function whose integral over the interval [*a*, *b*] is positive. The *n* numbers x_i are called nodes and the *n* numbers w_i are called weights. The nodes and the weights are chosen such that the right hand side is exact for all polynomials up to a certain order. The error term is R_n.

III. 3. 2. 1 Gaussian quadrature with arbitrary polynomials

For fixed nodes $\{x_i\}$, the theory of polynomial interpolation states that there is a corresponding Lagrange interpolation formula

$$p(x) = \sum_{i=1}^{n} f(x_i) l_i(x) \tag{III.11}$$

where $l_i(x) = \prod_{j=1}^{n} \frac{x - x_i}{x_i - x_j}, \ j \neq i$

This formula provides a polynomial of degree $\leq$n-1 that interpolates f at the nodes, i.e. that satisfies, $p(x_i) = f(x_i)$ for $1 \leq i \leq n$. Now we can simply write

$$\int_a^b f(x)dx \approx \int_a^b p(x)dx = \sum_{i=1}^{n} f(x_i) \int_a^b l_i(x)dx = \sum_{i=1}^{n} w_i f(x_i) \tag{III.12}$$

where the weights are $w_i = \int_a^b l_i(x)dx$

III. 3. 2. 2 Gaussian quadrature with orthogonal polynomials

The fundamental theorem of Gaussian quadrature states that the optimal abscissas of the *n*-point Gaussian quadrature formula are precisely the roots of the orthogonal polynomial for the same interval and weighting function. Gaussian quadrature is optimal because it fits all polynomials up to degree 2*n* exactly. More specifically, with arbitrary nodes (associated with roots of arbitrary polynomials), formula (III.10) will be exact for all polynomials of degree$\leq$*n*-1. With Gaussian nodes (associated with roots of orthogonal polynomials), formula (III.11) will be exact for all polynomials of degree ≤ 2*n*−1. In summary, all Gaussian quadrature rules have the format (III.10), where x_k, associated with zeros of orthogonal polynomials, are the integration points. There are many different choices for the nodes and weights. Table III.1 summarizes the 4 most common types of weight function *w*(*x*) and orthogonal polynomials *p*(*x*) used for Gaussian quadrature.

Table III. 1: Characteristics of the most popular Gaussian quadrature methods.

Interval	$w(x)$	Related orthogonal Polynomials
[-1, 1]	1	Legendre polynomials $P_n(x)$
[-1, 1]	$1/\sqrt{1-x^2}$	Chebyshev polynomials $T_n(x)$
[0, ∞]	e^{-x}	Laguerre polynomials $L_n(x)$
[-∞, ∞]	e^{-x^2}	Hermite polynomials $H_n(x)$

(i) Gauss-Legendre formula **[**$w(x)$=1**]**

Gauss, in 1814, constructed the Gauss–Legendre quadrature rule using hypergeometric functions and continued fractions, and Jacobi, twelve years later, noted the quadrature nodes were precisely the roots of the Legendre polynomial of degree *n*. Almost all introductory numerical analysis texts now show that the Gauss quadrature nodes are the simple roots of an associated orthogonal polynomial. The simplest form of Gaussian Integration is based on the use of an optimally chosen polynomial to approximate the integrand $f(x)$ over the interval [-1, +1].

$$\begin{aligned}\int_a^b f(x)dx &= \int_{-1}^{1} f\left(\frac{b-a}{2}x'+\frac{b+a}{2}\right)\frac{b-a}{2}dx' \\ &= \frac{b-a}{2}\int_{-1}^{1} g(x')dx' = \frac{b-a}{2}\sum_{k=1}^{n} w_k g(x_k^{'}) + R_n \\ &= \frac{b-a}{2}\sum_{k=1}^{n} w_k f\left(\frac{b-a}{2}x_k^{'}+\frac{b+a}{2}\right) + R_n\end{aligned} \tag{III.13}$$

where, $x' = \dfrac{x-(b+a)/2}{(b-a)/2}$, i.e., $x = \dfrac{b-a}{2}x' + \dfrac{b+a}{2}$, $-1 \le x' \le 1$, $x_k^{'}$ is the k^{th} zero of $P_n(x')$, $w_k = \dfrac{2}{(1-x_k^{'2})[P_n^{'}(x_k^{'})]^2}$, $R_n = \dfrac{2^{2n+1}(n!)^4}{(2n+1)[(2n)!]^3} g^{(2n)}(\xi)$ is the residual term and $P_n(x')$ is the Legendre polynomials of the first kind [62].

(ii) Gauss-Chebyshev formula **[** $w(x) = 1/\sqrt{1-x^2}$ **]**

This method is used for integrating over the interval [*a*, *b*] with a weighting function $w(x) = 1/\sqrt{1-x^2}$ and is based on the Chebyshev polynomials of the first kind $T_n(x)$.

$$\begin{aligned}\int_a^b f(x)dx &= \int_{-1}^{1} \frac{\sqrt{(x-a)(b-x)}\, f(x)}{\sqrt{(x-a)(b-x)}} dx \\ &= \int_{-1}^{1} \frac{g(x')}{\sqrt{1-x'^2}} dx' = \sum_{k=1}^{n} w_k g(x_k') + R_n \qquad \text{(III.14)} \\ &= \frac{b-a}{2} \sum_{k=1}^{n} w_k \sqrt{1-x_k'^2}\, f(\frac{b-a}{2} x_k' + \frac{b+a}{2}) + R_n\end{aligned}$$

where, $x' = \frac{x-(b+a)/2}{(b-a)/2}$, i.e., $x = \frac{b-a}{2} x' + \frac{b+a}{2}, -1 \le x' \le 1,$ $w_k = \frac{\pi}{n}$, $x_k' = \cos\frac{(2k-1)\pi}{2n}$ and $R_n = \frac{\pi}{2^{2n-1}(2n)!} g^{(2n)}(\xi)$.

(iii) Gauss-Hermite formula **[** $w(x) = e^{-x^2}$ **]**

This method is applicable for infinite integrals over the interval $[-\infty, \infty]$ and is based on the Hermite polynomials $H_n(x)$.

$$\begin{aligned}\int_{-\infty}^{\infty} f(x)dx &= \int_{-\infty}^{\infty} e^{-x^2} \left[e^{x^2} f(x)\right] dx \\ &= \sum_{k=1}^{n} w_k e^{x_k^2} f(x_k) + R_n\end{aligned} \qquad \text{(III.15)}$$

where x_k is the K^{th} zero of the Hermite polynomial $H_n(x)$, $w_k = \frac{2^{n-1} n! \sqrt{\pi}}{n^2 [H_{n-1}(x_k)]^2}$ and $R_n = \frac{n! \sqrt{\pi}}{2^n (2n)!} f^{(2n)}(\xi)$.

(iv) Gauss-Laguerre formula **[** $w(x) = e^{-x}$ **]**

This method is used for integration over the semi-infinite interval [0, 1] and is based on the Laguerre polynomials $L_n(x)$.

$$\begin{aligned}\int_{0}^{\infty} f(x)dx &= \int_{0}^{\infty} e^{-x} \left[e^{x} f(x)\right] dx \\ &= \sum_{k=1}^{n} w_k e^{x_k} f(x_k) + R_n\end{aligned} \qquad \text{(III.16)}$$

where x_k is the K^{th} zero of the Laguerre polynomial $L_n(x)$, $w_k = \frac{x_k}{(n+1)^2 [H_{n+1}(x_k)]^2}$ and $R_n = \frac{(n!)^2 \sqrt{\pi}}{(2n)!} f^{(2n)}(\xi)$.

The nodes and weights for the above Gauss quadrature methods are calculated from the eigen values and eigenvectors of a symmetric tridiagonal matrix, as described in [62, 66]. In order to show the efficiency of the Gauss quadrature method, we consider an example of gamma function computations, $\Gamma(x) = \int_0^\infty t^{x-1} e^{-t} dt$ using the Matlab "function gamma(.)", left sums, trapezoidal and Gauss quadrature rules. Note that, Legendre and Laguerre polynomials are employed for intervals of $x \in [0,\ 1]$ and $x \in [1,\ \infty]$ respectively. It is clear in Table III. 3 that the Gauss quadrature rule which uses a number n = 200 nodes and weights provides the best approximation to the ones given by a Matlab function. In cases of left and trapezoidal rules, n = 10000 is taken.

Table III.2: Gamma function evaluation using traditional and Gauss quadrature methods

x	**Matlab [74]**	**Left rule**	**Trapezoidal rule**	**Gauss**
0.3	2.9916	3.5179	2.8891	2.9008
0.7	1.2981	1.3369	1.2972	1.2979
0.9	1.0686	1.0774	1.0674	1.0686
1.7	0.9086	0.9086	0.9086	0.9086

III. 4 Estimators

In this section, three estimators are constructed on the condition that the CGIG clutter plus noise samples are statistically iid.

III. 4.1 Method of moments (HOME)

It will be shown bellow that a closed-form expression of the HOME method can be obtained using the first three integer order moments of (III.5). In general, the HOME method for a longer number of samples produces good estimation accuracy. Moments of orders 1, 2 and 3 can be calculated by

$$\begin{cases} \mu_1 = \dfrac{\langle z \rangle}{N} = \sqrt{\dfrac{\lambda}{2\pi}} e^{\lambda/\mu} \displaystyle\int_0^\infty y^{-3/2} (y + p_n) \exp\left(-\dfrac{\lambda}{2\mu^2} y - \dfrac{\lambda}{2y} \right) dy \\ \mu_2 = \dfrac{\langle z^2 \rangle}{(N+1)N} = \sqrt{\dfrac{\lambda}{2\pi}} e^{\lambda/\mu} \displaystyle\int_0^\infty y^{-3/2} (y + p_n)^2 \exp\left(-\dfrac{\lambda}{2\mu^2} y - \dfrac{\lambda}{2y} \right) dy \\ \mu_3 = \dfrac{\langle z^3 \rangle}{N(N+1)(N+2)} = \sqrt{\dfrac{\lambda}{2\pi}} e^{\lambda/\mu} \displaystyle\int_0^\infty y^{-3/2} (y + p_n)^3 \exp\left(-\dfrac{\lambda}{2\mu^2} y - \dfrac{\lambda}{2y} \right) dy \end{cases} \qquad \text{(III.17)}$$

The integral result $\int_0^\infty x^{\alpha-1} e^{-px-q/x} dx = 2(q/p)^{\alpha/2} K_\alpha\left(2\sqrt{pq}\right)$ in [63, 64] with their special cases of the second kind Bessel function order (i.e., $K_{\pm 1/2}(x) = e^{-x}\sqrt{\pi/2x}$, $K_{\pm 3/2}(x) = e^{-x}\sqrt{\pi/2x}(1+1/x)$ and $K_{\pm 5/2}(x) = e^{-x}\sqrt{\pi/2x}\left(3/x^2 + 3/x + 1\right)$ are used to evaluate (III.17). After some mathematical manipulations, (III.17) becomes

$$\begin{cases} \mu_1 = \mu + p_n \\ \mu_2 = \mu^2\left(\dfrac{\mu}{\lambda} + 1\right) + 2p_n\mu + p_n^2 \\ \mu_3 = \mu^3\left(\dfrac{3\mu^2}{\lambda^2} + \dfrac{3\mu}{\lambda} + 1\right) + 3p_n\mu^2\left(\dfrac{\mu}{\lambda} + 1\right) + 3p_n^2\mu + p_n^3 \end{cases} \qquad \text{(III.18)}$$

Three cases of *CNR* values can occur in practice; i.e. $CNR \to \infty$ (noise-free situation), known *CNR* (known system noise power) and unknown *CNR* (known system noise power plus unknown Rayleigh clutter power). When $CNR \to \infty$, the method of moments has been presented in [23]. In this case, $\hat{\lambda} = \lambda_{eff} = \dfrac{\hat{\mu}_1^3}{\hat{\mu}_2 - \hat{\mu}_1^2}$, where hat (^) symbol is used to identify the estimated quantity and λ_{eff} is a scalar defined as the effective shape parameter. If *CNR* is known and finite, we need only the first two intensity moments to compute $\hat{\lambda}$. Thus, substituting $p_n = \dfrac{\mu}{CNR}$ and $\mu = \hat{\mu}_1(1 + 1/CNR)^{-1}$ into (III.18), we obtain a closed-form of the moments method as

$$\hat{\lambda} = \frac{\hat{\mu}_1^3 (1 + CNR^{)-1^{-3}}}{\hat{\mu}_2 - \hat{\mu}_1^2 (1 + CNR^{-1})^{-2} (1 + 2CNR^{-1} + CNR^{-2})} \qquad \text{(III.19)}$$

If *CNR* is unknown, the system of equations given by (III.18) must be solved and after some mathematical stages, the HOME method can be obtained (we omit the details)

$$\hat{\lambda} = \frac{27(\hat{\mu}_2 - \hat{\mu}_1^2)^5}{(\hat{\mu}_3 - 3\hat{\mu}_2\hat{\mu}_1 + 2\hat{\mu}_1^3)^3} \tag{III.20}$$

values of $\hat{\mu}_1$, $\hat{\mu}_2$ and $\hat{\mu}_3$ are calculated from the data, ie., $\hat{\mu}_k = \frac{\Gamma(N)}{\Gamma(N+k)} \frac{1}{M} \sum_{i=1}^{M} z_i^k$, k=1,2 or3.

Using (III.18) and (III.20), the mean, the noise power and *CNR* are then estimated by

$$\begin{cases} \hat{\mu} = \left[(\hat{\mu}_2 - \hat{\mu}_1^2)\hat{\lambda}\right]^{1/3} = \hat{\mu}_1 \lambda_{eff}^{-1/3} \hat{\lambda}^{1/3} \\ \hat{p}_n = \hat{\mu}_1 - \hat{\mu} = \mu_1\left(1 - \lambda_{eff}^{-1/3} \hat{\lambda}^{1/3}\right) \\ C\hat{N}R = \dfrac{\hat{\mu}}{\hat{p}_n} = \left(\lambda_{eff}^{1/3} \hat{\lambda}^{-1/3} - 1\right)^{-1} \end{cases} \tag{III.21}$$

where the estimates $\hat{\lambda}$, $\hat{\mu}$, $C\hat{N}R$ and $\lambda_{eff} = \hat{\mu}_1^3 / (\hat{\mu}_2 - \hat{\mu}_1^2)$ are all scalars

III. 4.2 Constrained NIOME methods

In order to improve the estimation accuracy, non-integer order moment, $\langle z^r \rangle$ with r<1 should be used instead of moment of order 3, $\langle z^3 \rangle$. This estimation technique requires therefore a combination of three theoretical moments, i.e.,$\langle z^r \rangle$,$\langle z \rangle$ and $\langle z^2 \rangle$. First, we rearrange (III.5) as

$$\frac{\langle z^r \rangle \sqrt{2\pi}\,\Gamma(N)}{\Gamma(N+r)} = \sqrt{\lambda} e^{\lambda/\mu} \int_0^\infty y^{-3/2} (y + p_n)^r \exp\left(-\frac{\lambda}{2\mu^2} y - \frac{\lambda}{2y}\right) dy \tag{III.22}$$

The substitution of $t = \frac{\lambda}{2\mu^2} y$ into (III .22) yields

$$\frac{\langle z^r \rangle \sqrt{2\pi}\,\Gamma(N)}{\Gamma(N+r)} = \sqrt{\lambda} \left(\frac{2\mu^2}{\lambda}\right)^{r-\frac{1}{2}} e^{\lambda/\mu} \int_0^\infty t^{-3/2} \left(t + \frac{p_n \lambda}{2\mu^2}\right)^r e^{-t} \exp\left(-\frac{\lambda^2}{4\mu^2 t}\right) dt \tag{III.23}$$

Let $\hat{\theta} = \lambda / 2\mu$ be a scalar, (III.23) is readily expressed in terms of *CNR* and $\hat{\theta}$

$$\hat{A} = \frac{\hat{\theta}^{1-r} e^{2\hat{\theta}}}{\left(1 + \frac{1}{CNR}\right)^r} \int_0^\infty t^{-3/2} \left(t + \frac{\hat{\theta}}{CNR}\right)^r e^{-t} e^{-\frac{\hat{\theta}^2}{t}} dt \tag{III.24}$$

where, $\hat{A} = \dfrac{\langle z^r \rangle \sqrt{\pi}\,\Gamma(N) N^r}{\langle z \rangle^r \Gamma(N+r)}$. In the case of $CNR \to \infty$, (III.24) is exactly the same estimator obtained in [23] and the estimates of the shape parameter are computed using the interpolation method. On the other hand, if the *CNR* is known and finite, the evaluation of the integral in (III.24) is difficult in which numerical methods can be used. In this work, we resort to the use of the Gauss quadrature numerical integration method presented in the previous section. In such approach, Laguerre polynomials are generated from a recurrence relation, and the nodes and weights are calculated from the eigenvalues and eigenvectors of a symmetric tridiagonal matrix [20, 61, 62]. As stipulated in [20], it is advantageous to split the domain of integration into two parts and use Gauss-Legendre quadrature on [0, 1] and Gauss-Laguerre quadrature on $[1, \infty]$ for small values of the shape parameter. Thus, to obtain good estimates of λ, the same behavior is found in which (III.24) is rewritten in terms of two integrals as

$$\hat{A} = \frac{\hat{\theta}^{1-r} e^{2\hat{\theta}}}{\left(1 + \dfrac{1}{CNR}\right)^r} \left[\int_0^1 t^{-3/2} \left(t + \frac{\hat{\theta}}{CNR} \right)^r e^{-t} e^{-\frac{\hat{\theta}^2}{t}} dt + \int_1^\infty t^{-3/2} \left(t + \frac{\hat{\theta}}{CNR} \right)^r e^{-t} e^{-\frac{\hat{\theta}^2}{t}} dt \right] \tag{III.25}$$

The substitution *t*=*s*+1 is made in the second integral in (III.25)

$$\hat{A} = \frac{\hat{\theta}^{1-r} e^{2\hat{\theta}}}{\left(1 + \dfrac{1}{CNR}\right)^r} \left[\int_0^1 t^{-3/2} \left(t + \frac{\hat{\theta}}{CNR} \right)^r e^{-t} e^{-\frac{\hat{\theta}^2}{t}} dt + e^{-1} \int_0^\infty (s+1)^{-3/2} \left(s + 1 + \frac{\hat{\theta}}{CNR} \right)^r e^{-s} e^{-\frac{\hat{\theta}^2}{s+1}} ds \right] \tag{III.26}$$

Finally, $\hat{\theta}$ is obtained after the optimization of the following square error (SE) function

$$\hat{\theta} = \underset{\hat{\theta}}{\arg\min} \left(\hat{A} - \textit{right hand side of } (III.24) \text{ or } (III.26) \right)^2 \tag{III.27}$$

Once $\hat{\theta}$ is determined, the estimates of λ are obtained by, $\hat{\lambda} = 2\hat{\mu}\hat{\theta} = 2\hat{\theta}\hat{\mu}_1 (1 + 1/CNR)^{-1}$.

If *CNR* is unknown, it must be expressed in terms of the first two intensity moments (i.e., $CNR = (\lambda_{eff}^{1/3} \hat{\lambda}^{-1/3} - 1)^{-1}$. Substituting (III.21) into (III.23), (III.23) becomes

$$\hat{B} = \sqrt{\hat{\lambda}} \left(\frac{2\hat{\mu}^2}{\hat{\lambda}} \right)^{r - \frac{1}{2}} e^{\hat{\lambda}/\hat{\mu}} \int_0^\infty t^{-3/2} \left(t + \frac{\hat{p}_n \hat{\lambda}}{2\hat{\mu}^2} \right)^r e^{-t} \exp\left(-\frac{\hat{\lambda}^2}{4\hat{\mu}^2 t} \right) dt \tag{III.28}$$

where $\hat{B} = \dfrac{\langle z^r \rangle \sqrt{2\pi}\,\Gamma(N)}{\Gamma(N+r)}$. Also, the integral in (III.28) can be readily evaluated using the Gauss-Laguerre quadrature integration method. In the same manner as before, (III.28) is rewritten in terms of two integrals as

$$\begin{aligned}\hat{B}=\sqrt{\hat{\lambda}}\left(\frac{2\hat{\mu}^2}{\hat{\lambda}}\right)^{r-\frac{1}{2}} e^{\hat{\lambda}/\hat{\mu}}\Bigg[&\int_0^1 t^{-3/2}\left(t+\frac{\hat{p}_n\hat{\lambda}}{2\hat{\mu}^2}\right)^r e^{-t}\,\exp\left(-\frac{\hat{\lambda}^2}{4\hat{\mu}^2 t}\right)dt\\ &+\int_1^\infty t^{-3/2}\left(t+\frac{\hat{p}_n\hat{\lambda}}{2\hat{\mu}^2}\right)^r e^{-t}\,\exp\left(-\frac{\hat{\lambda}^2}{4\hat{\mu}^2 t}\right)dt\Bigg]\end{aligned}\tag{III.29}$$

The substitution $t=s+1$ is made in the second integral, (III.29) becomes

$$\begin{aligned}\hat{B}=\sqrt{\hat{\lambda}}\left(\frac{2\hat{\mu}^2}{\hat{\lambda}}\right)^{r-\frac{1}{2}} e^{\hat{\lambda}/\hat{\mu}}\Bigg[&\int_0^1 t^{-3/2}\left(t+\frac{\hat{p}_n\hat{\lambda}}{2\hat{\mu}^2}\right)^r e^{-t}\,\exp\left(-\frac{\hat{\lambda}^2}{4\hat{\mu}^2 t}\right)dt\\ &+e^{-1}\int_0^\infty (s+1)^{-3/2}\left(s+1+\frac{\hat{p}_n\hat{\lambda}}{2\hat{\mu}^2}\right)^r e^{-s}\,\exp\left(-\frac{\hat{\lambda}^2}{4\hat{\mu}^2(s+1)}\right)ds\Bigg]\end{aligned}\tag{III.30}$$

The estimates of λ are obtained after the optimization of the following SE function

$$\hat{\lambda}=\underset{\hat{\lambda}}{\arg\min}\left(\hat{B}-\mathit{right\ hand\ side\ of}\ (\mathit{III}.28)\ \mathrm{or}\ (\mathit{III}.30)\right)^2\tag{III.31}$$

Using the Gauss quadrature integration method, the CNIOME based approach is highlighted by the flowchart of Figure III.4 for $r=0.1$ (i.e., low values of r provide the best estimates of λ [23]). For known *CNR*, equations (III.24), (III.26) and (III.27) are used in Figure III.4 instead of (III.28), (III.30) and (III.31) respectively. In this case, the clutter mean is estimated by $\hat{\mu}=\hat{\mu}_1(1+1/CNR)$.

III. 4. 3 Constrained MLE methods

This estimator is based on the maximization of the logarithm of likelihood function. The compound representation of the CGIG model with noise for N non-coherently integrated pulses can be reformulated as

$$p_Z(z|p_n,N)=\sqrt{\frac{\lambda}{2\pi}}\int_0^\infty p_Z(z|y,p_n,N)\,y^{-3/2}\exp\left(-\frac{\lambda}{2\mu^2}y-\frac{\lambda}{2y}\right)dy\tag{III.32}$$

Also, there is no closed-form for (III.32), numerical integration is required to evaluate the log likelihood function and numerical optimisation must be used to find the maximum. If we make the substitution $t=\frac{\lambda}{2\mu^2}y$, (III.32) becomes

$$p_Z(z|p_n,N)=\frac{\lambda}{2\mu\sqrt{\pi}}\int_0^\infty p_Z(z|t,p_n,N)\,t^{-3/2}e^{-t}e^{-\frac{\lambda^2}{4\mu^2 t}}dt\tag{III.33}$$

As mentioned above, the domain of integration is subdivided into two parts. Gauss-Legendre quadrature is used on [0, 1] and Gauss-Laguerre quadrature on $[1,\infty]$. For small values of λ (typically less than 1), (III.33) is rewritten as

$$p_Z\left(z|p_n,N\right)=\frac{\lambda}{2\mu\sqrt{\pi}}\left[\int_0^1 p_Z\left(z|t,p_n,N\right)t^{-3/2}e^{-t}e^{-\frac{\lambda^2}{4\mu^2t}}dt+\int_1^\infty p\left(z|t,p_n,N\right)t^{-3/2}e^{-t}e^{-\frac{\lambda^2}{4\mu^2t}}dt\right]$$

$$=\frac{\lambda}{2\mu\sqrt{\pi}}\left[\int_0^1 p_Z\left(z|t,p_n,N\right)t^{-3/2}e^{-t}e^{-\frac{\lambda^2}{4\mu^2t}}dt+e^{-1}\int_0^\infty p_Z\left(z|t,p_n,N\right)(s+1)^{-3/2}e^{-s}e^{-\frac{\lambda^2}{4\mu^2(s+1)}}ds\right]$$

(III.34)

The fitness function or the negative log-likelihood function (LLF) to be minimized according to the CMLE method is given by

$$\hat{\lambda}=\min_{\hat{\lambda}}\left[-\sum_{i=1}^{M}\log\left(p_Z(z_i|p_n,N)\right)\right] \tag{III.35}$$

For noise-free case with N=1, partial derivatives of the LLF with respect to λ and μ are obtained and the MLE method is numerically solved in [23]. The CMLE approach based on the Gauss quadrature integration method is presented by the flowchart of Figure III.4, using (III.33)-(III.35). 100 point Gauss-Legendre quadrature used on [0,1] and 20 point Gauss-Laguerre quadrature used on $[1,\infty]$. As the nodes and weights are independent of the distribution parameters, they are not recalculated at each iteration. Throughout some cases of simulations, the optimization of the fitness function runs into the local minimum where the shape parameter values tend to the lower bound of the research range. The optimisation issue related to the upper bound is also observed in a constrained ML estimator for the K distribution shape parameter with noise [20]. To this effect, estimation results in Section III.4 are presented by adapting the lower bound for which the research interval is given by $[0.01\lambda_{eff}\ 1000]$.

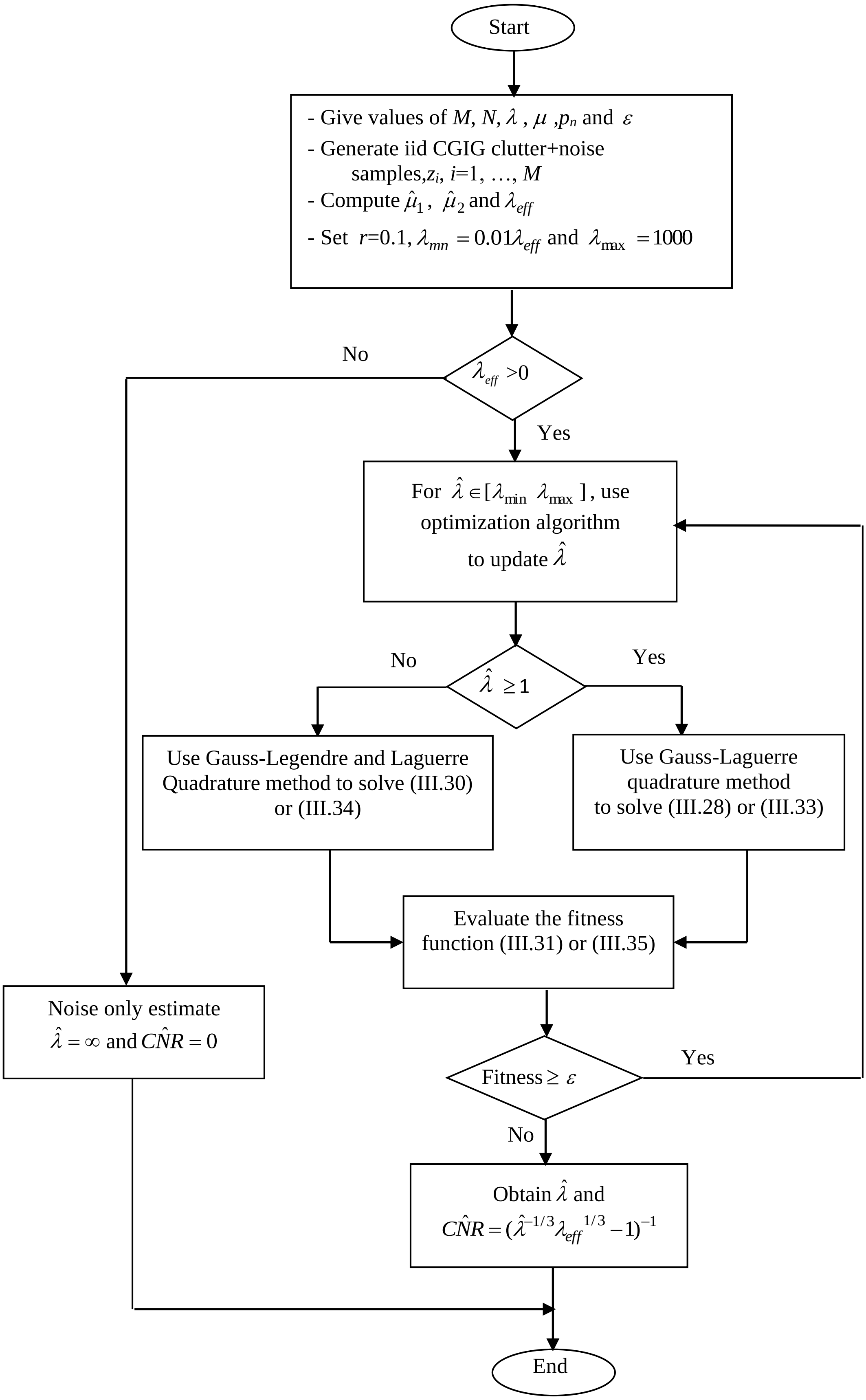

Figure III.4: Flowchart of CNIOME and CMLE methods to estimating CGIG clutter plus noise parameters using simulated data for one iteration.

III.5 Estimation analysis

In this section, we carry out some computer simulations in order to compare the estimation performance of the methods presented in Section III.4 and to confirm their applicability. Specifically, the mean squared error (MSE = $E[(\hat{\lambda}-\lambda)^2]$, $E(.)$ denotes the expected value) and bias of estimation (Bias = $E[\hat{\lambda}-\lambda])$ are performed to judge the estimation accuracy of the proposed methods. The CGIG clutter plus noise data are generated for a range 0.1 to 3.1 of the shape parameter for *CNR* = -3, 0, 5 and 10dB. In each case, the power of the random signals is normalized so that the first order moment of clutter plus noise process is unity ($\mu + p_n = 1$). Our attention is also focused on the number of samples *M* =1000, 2000 and 10000 and the number of non-coherent integrated pulses *N* =1, 5 and 10. Based on [67], the *M* samples of non-coherently integrated pulses of the CGIG clutter plus noise are generated by the following steps:

Start

Step 1: Set *i*=1 and let λ, *CNR*, p_n=1/(1+*CNR*) , $\mu = 1 - p_n$ be scalars with positive and real values

Step 2: Generate a random variable from the normal distribution with zero mean and a standard deviation equal to 1 $v = N(0,1)$

Step3: Square the value $a = v^2$

Step 4: Calculate a new random variable as $b = \mu + \frac{\mu^2 a}{2\lambda} - \frac{\mu}{2\lambda}\sqrt{4\mu\lambda a + \mu^2 a^2}$

Step 5: Generate a random variate sampled from the uniform distribution between '0' and '1'
$c = U(0,1)$

Step 6: If $c \le \frac{\mu}{\mu + b}$ then return $x_r(i) = b$, else return $x_r(i) = \mu^2 / b$
where v, *a*, *b* and *c* are all scalars

Step 7: Set *i*=*i*+1 and repeat step 2 through step 6 until *i*=*M*

Step 8: Obtain non-coherently *M* samples which follow the CGIG clutter plus noise

$$Z = \sum_{j=1}^{N} exprnd(X_r + p_n), \quad X_r = [x_r(1) \;\; x_r(2) \;\; \ldots \;\; x_r(M)]$$

where *Z* and X_r are vectors of *M* random variables and *exprnd*(.) denotes the Matlab subroutine used to generate random numbers from the exponential distribution with mean $X_r + p_n$.

End

Estimation of the unknown shape parameter is achieved over *n* = 100 independent Monte-Carlo trials. In all simulations, *CNR* values are assumed to be known and unknown. It may be noted that if *CNR* is known, the mean, $\langle z \rangle$ of the CGIG clutter plus noise is sufficient to calculate the estimates of λ. Otherwise, we need to exploit the first two intensity moments $\langle z \rangle$ and $\langle z^2 \rangle$ to compute λ_{eff} and $\hat{\lambda}$. Squared errors (fitness functions) given by (III.27) and (III.31) are optimized using 'fminserch' subroutine of the Matlab code. The latter finds the minimum of a scalar function of one variable starting at an initial value (i.e., $\hat{\theta}$ for known *CNR* and $\hat{\lambda}$ for unknown *CNR*). Left hand sides of (III.27) and (III.31) denote the estimated quantities from the data, but their right hand sides represent mathematical functions with an unknown parameter. Unconstrained nonlinear optimization is therefore used for parameter solutions.

First, we want to examine the estimation performance using the steps given by Figure III. 4 when the *CNR*=0 is known a *priori*. To this end, Figures III. 5a and 5b depict the MSE values in terms of true values of the shape parameter λ for *M* = 1000 and *M* = 2000 respectively, *CNR*=0dB and *N*=1. By investigating these results, we observe that, the CMLE method performs better than the CNIOME method which in turn performs better than the method of moments particularly when λ is greater than 0.7. In cases of low and high *CNR* values, it is readily seen from Figures. III. 6a and 6b, that the method of moments provides a good fit better then the CMLE method while the CNIOME method is less accurate than the others. The improvements in the MSE values can be explained by the fact that if *CNR* is known, $\hat{\mu}_3$ is not used and the optimisation complexity of (III.24), (III.26) and (III.27) is reduced. Since the estimates by the HOME are calculated straightforwardly, the computation time of the CMLE method is higher.

Next, the accuracy of the estimators is examined when *CNR* values are unknown. Figure III.7a shows three sets of MSE curves versus λ for *M*=1000, *N*=1 and *CNR*=0dB. A slight superiority of the CNIOME against the CMLE method is obtained and the HOME method presents poor results in this case. This serious degradation in the MSE is obvious, because the method of moments employs, $\hat{\mu}_3$ with low sample size. For multilook case with *N* = 10, Figure III. 7b depict MSE curves against λ. If $\lambda \geq 1$, there is a complete overlap of the two sets of the MSE curves corresponding to the CNIOME and the CMLE methods whereas the MSE values obtained by the HOME method are improved with respect to those obtained by Figure III. 7a. to investigate another operational condition, we test the effect of the number of samples *M* = 2000 and *CNR* = 0dB on the performance of the three estimation approaches.

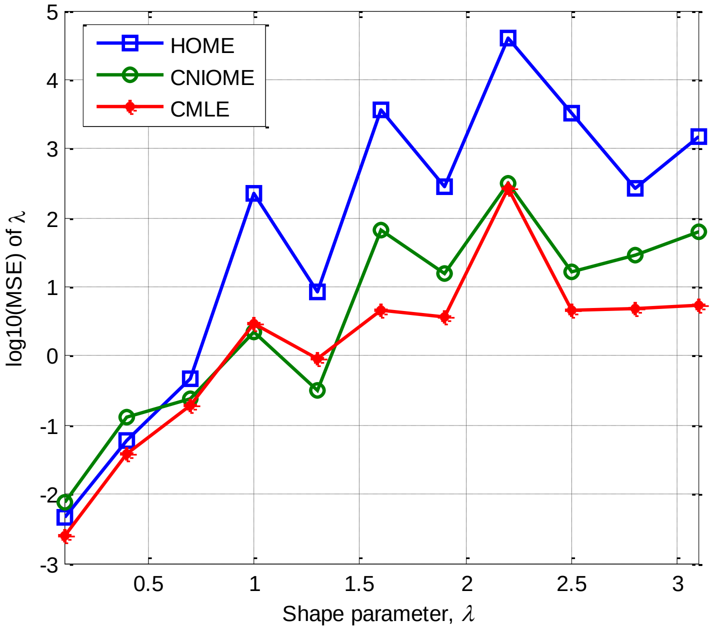

(a)

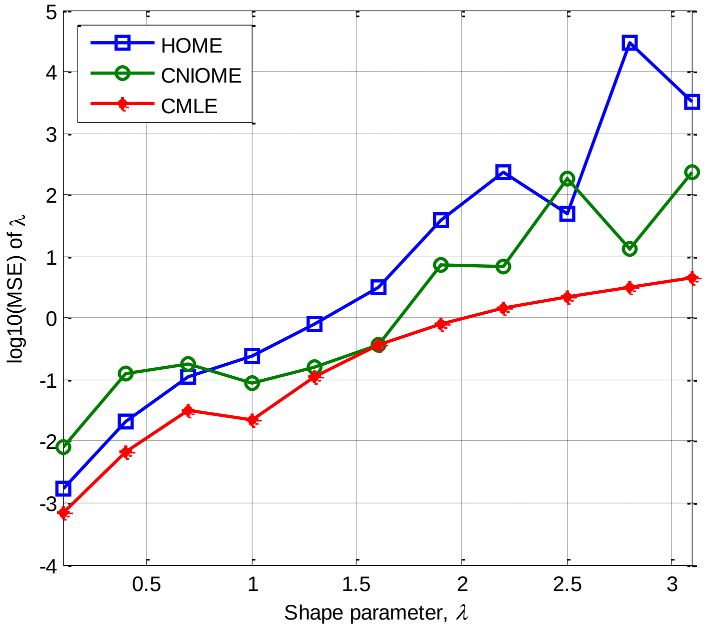

(b)

Figure III. 5: Estimation performance of HOME, CNIOME and CMLE methods for the shape parameter of CGIG clutter plus noise with known *CNR* = 0dB, *N*=1 and *n* = 100 trials
(a) *M* = 1000 samples; (b) *M* = 2000 samples

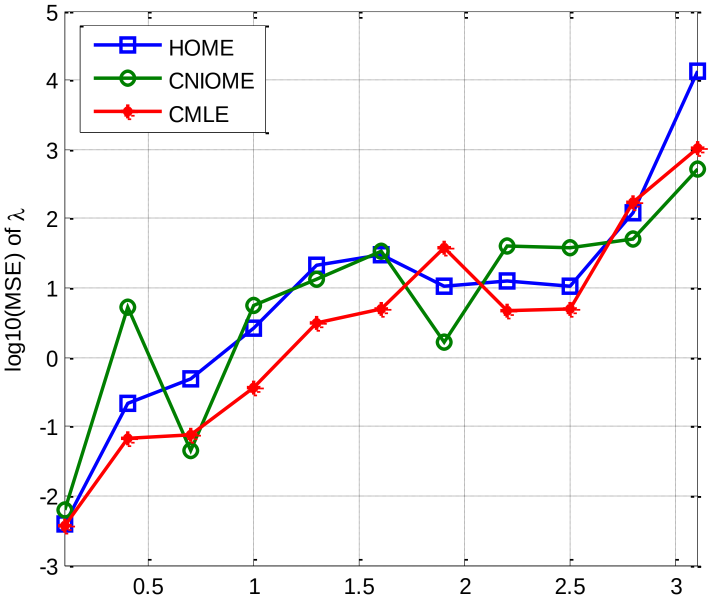

(a)

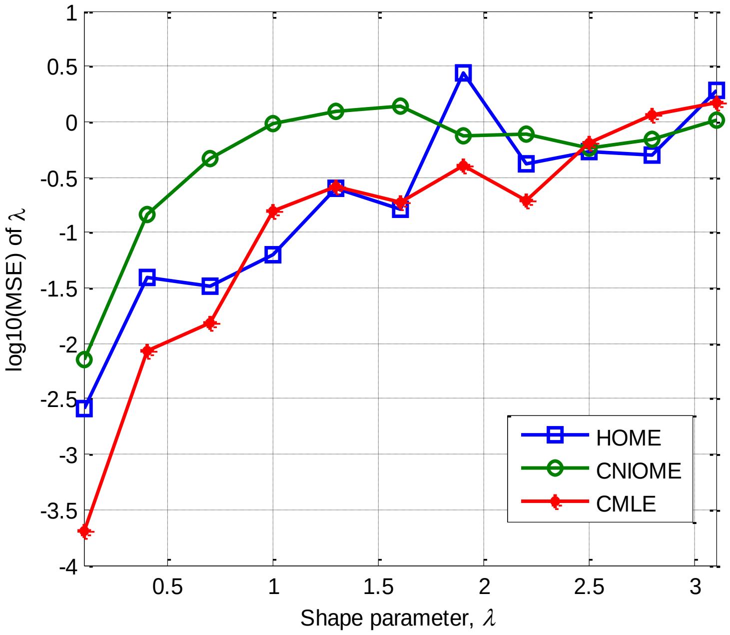

(b)

Figure III. 6: Estimation performance of HOME, CNIOME and CMLE methods for the shape parameter of CGIG clutter plus noise with known *CNR*, $N = 1$, $M = 1000$ and $n = 100$ trials
(a) *CNR* = -3dB; (b) *CNR* = 10dB

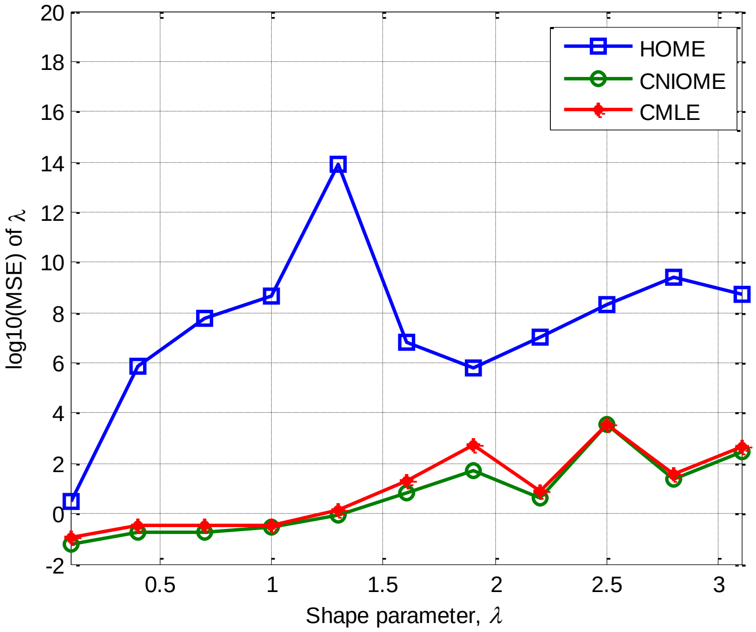

(a)

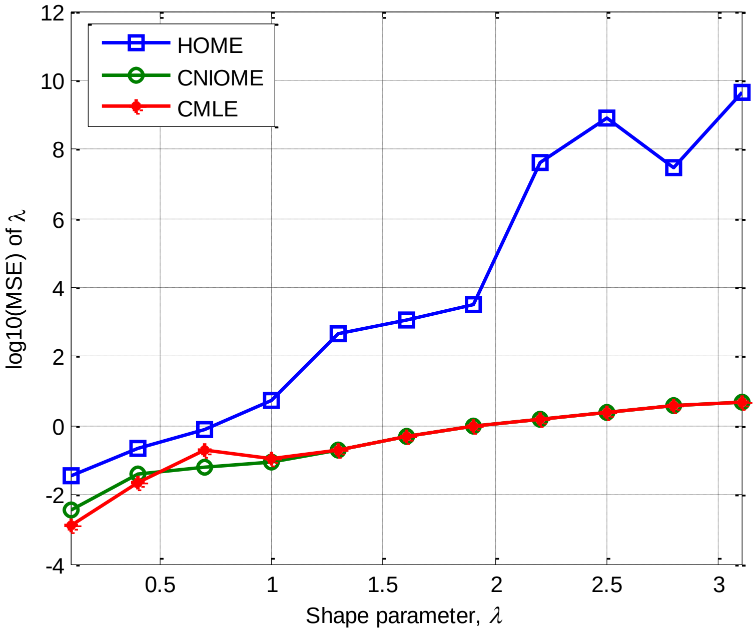

(b)

Figure III. 7: Estimation performance of HOME, CNIOME and CMLE methods for the shape parameter of CGIG clutter plus noise with unknown CNR = 0dB, M = 1000 and n = 100 trials (a) N = 1; (b) N = 10

Compared to the results given in Figures III. 7a and 7b respectively, there is an improvement in the MSE values as shown in Figures. III. 8a and III. 8b. In this situation, the estimation precision of HOME method is dependent on the number of samples. Typically, increasing M is not always practical since real radar may have a very limited data to train on, especially if it is on an airborne platform or scanning in azimuth. For high sample size as before (M = 2000), Figures. III. 9a and 9b show a set of MSE estimation curves of λ for the case of CNR = -3 and 5dB with equal integrated pulses number (N = 10). It is clearly seen that the estimates based on the CMLE method are also the most accurate, followed by those obtained by the CNIOME and HOME methods. In the case of low CNR, the shape parameter is not estimated accurately by any of three methods due to small effect of clutter. Figures III. 10a and 10b illustrate the effect of varying M on the accuracy of λ (MSE values) and CNR (bias values). Here the CMLE method is not used since it gives approximate results better then the CNIOME method. It is worth noting that the estimation bias of CNR at high sample size is reduced. If λ is greater than 1, both the bias of CNR and the MSE of λ are fluctuating when the HOME method is employed. In this interval, the estimation of CNR is difficult, which would be expected since clutter and noise have approximately the same distribution. As an aside, the noise power can be estimated at the radar receiver (electronic system). However, we can not quantify the power of Rayleigh clutter (Gaussian clutter) embedded in non Gaussian clutter. To determine the CNR in this case, a theoretical CG model with noise (e.g., K+noise, Pareto+noise, CGIG+noise,…etc) must be selected firstly and CNR values can be then determined from the estimated shape and scale parameters.

As discussed in the introduction section, noise and clutter are always present in the received data. Low, medium or high CNR values can be considered at each data measurement. This happens when the overall power of Rayleigh clutter plus thermal noise is varying. To validate the CGIG clutter plus noise distribution using IPIX database, Figures III. 11a-11d show fitting comparisons of CGIG PDFs and CCDFs with and without noise against empirical data. They are obtained for the cases of cell resolution of 3m, 17th cells range with VV polarization and 6th cells range with HH polarization where the parameters are estimated using the CMLE method. It can be noticed that the CGIG plus noise distribution provides the best tail fitting to real data. This is due to the presence of a considerable amount of noise power in the data ($C\hat{N}R$ = -1.0229dB and $C\hat{N}R$ = -4.8764 dB are found for VV polarization and HH polarizations respectively).

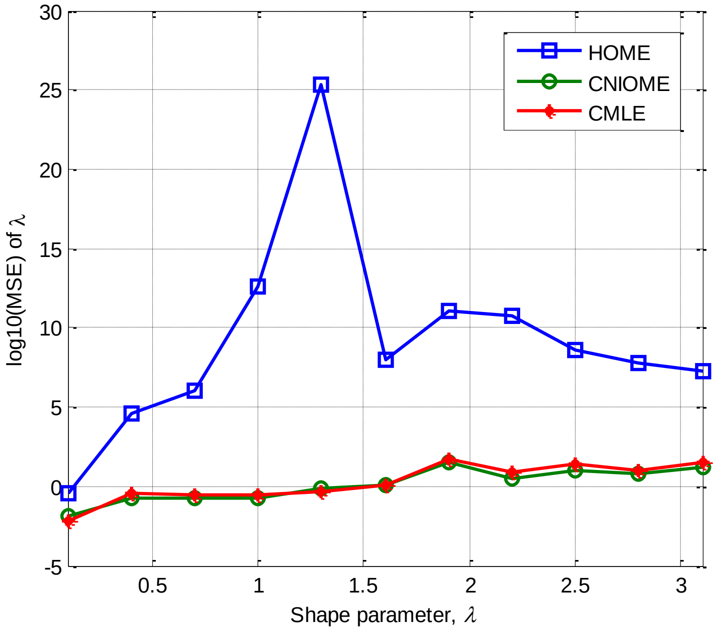

(a)

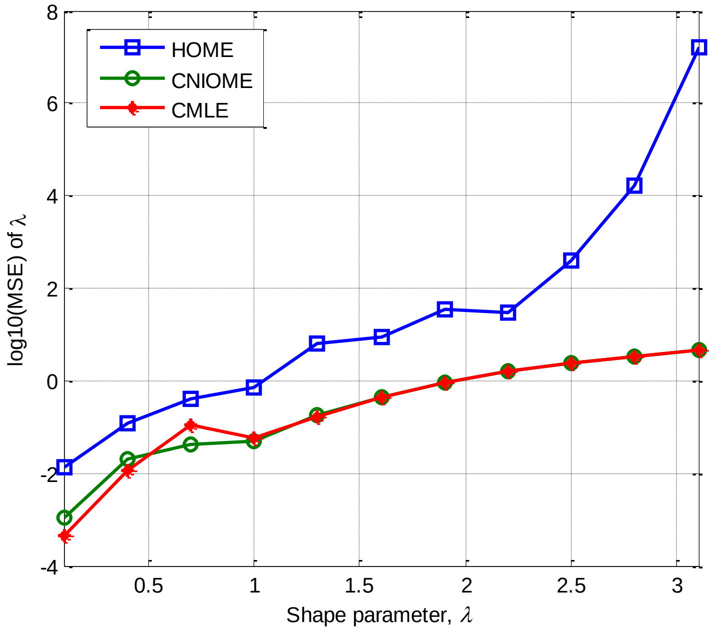

(b)

Figure III. 8: Estimation performance of HOME, CNIOME and CMLE methods for the shape parameter of CGIG clutter plus noise with unknown *CNR* = 0dB, *M* = 2000 and *n* = 100 trials (a) *N* = 1; (b) *N* = 10

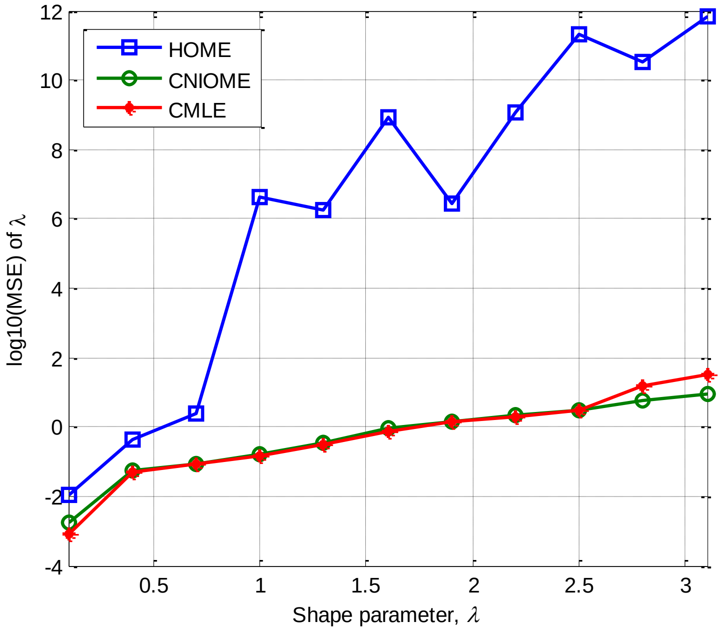

(a)

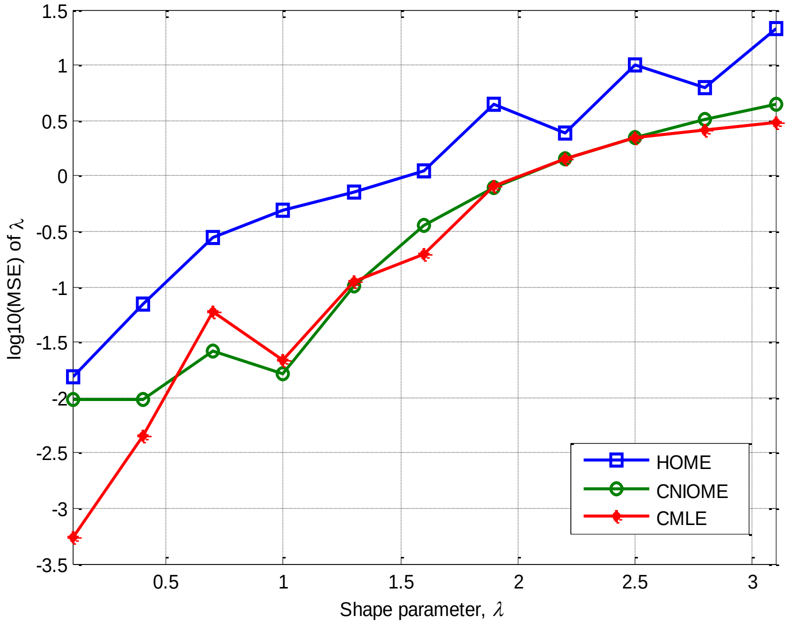

(b)

Figure III. 9: Estimation performance of HOME, CNIOME and CMLE methods for the shape parameter of CGIG clutter plus noise with unknown *CNR*, *N*=10, *M* = 2000 and *n* = 100 trials (a) *CNR* = -3dB; (b) *CNR* = 5dB

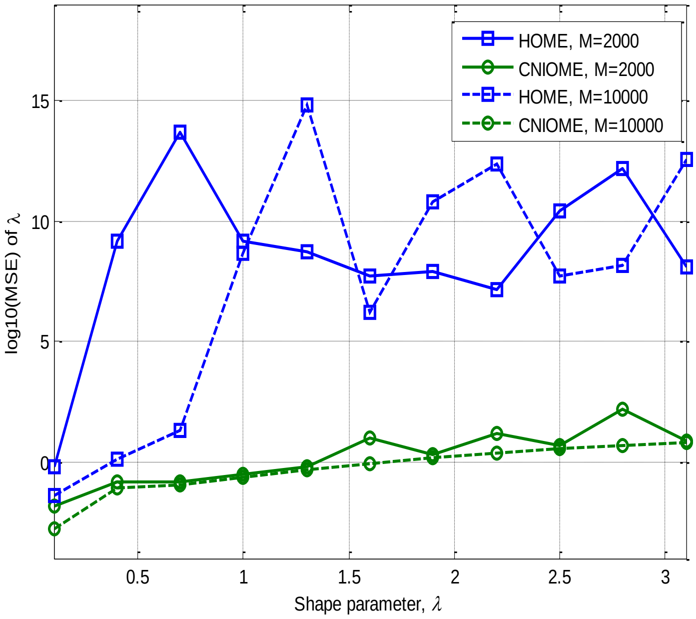

(a)

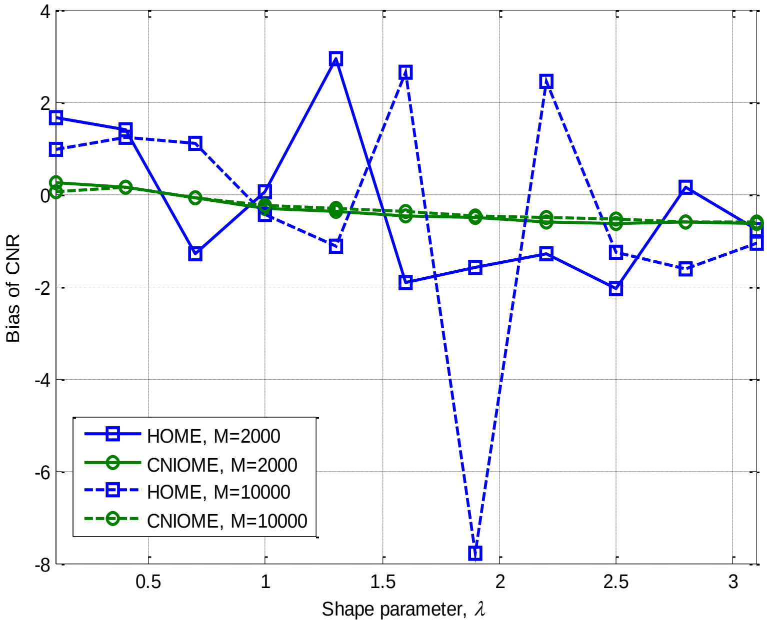

(b)

Figure III. 10: Estimation performance of HOME and CNIOME methods for the shape parameter of CGIG clutter plus noise with unknown *CNR* = 0dB
(a) MSE estimation of λ ; (b) Bias estimation of *CNR*

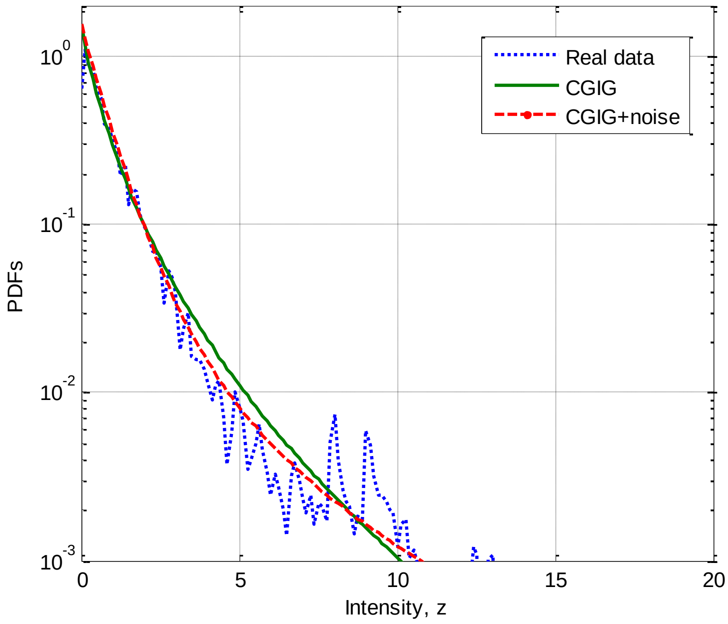
PDFs
Intensity, z
10^0
10^-1
10^-2
10^-3
0
5
10
15
20
Real data
CGIG
CGIG+noise

(a)

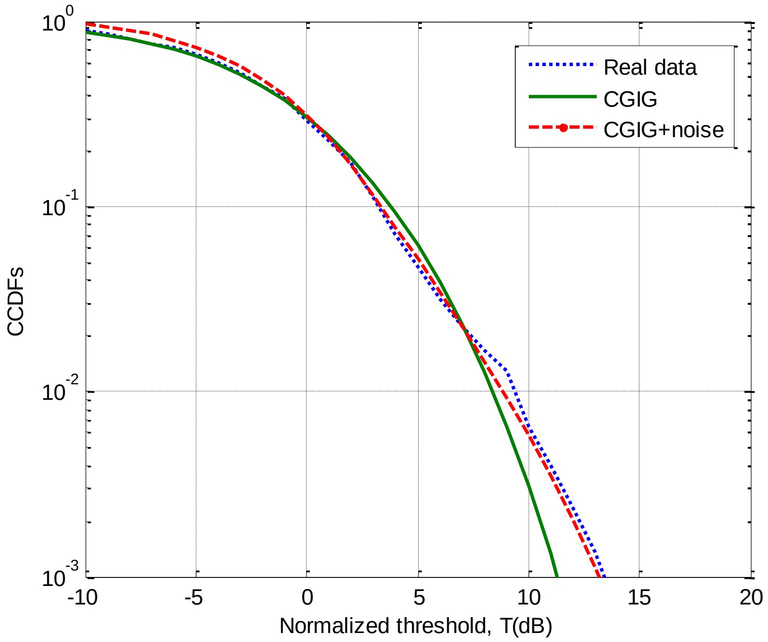
CCDFs
Normalized threshold, T(dB)
10^0
10^-1
10^-2
10^-3
-10
-5
0
5
10
15
20
Real data
CGIG
CGIG+noise

(b)

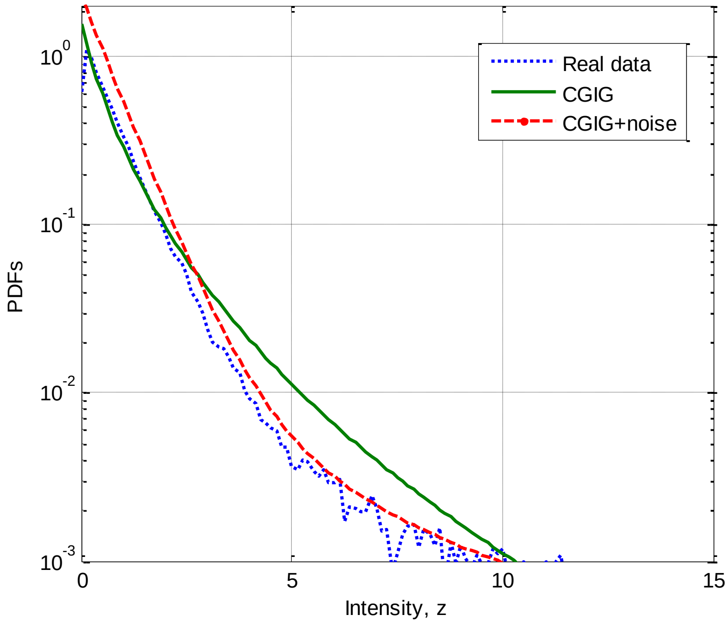

(c)

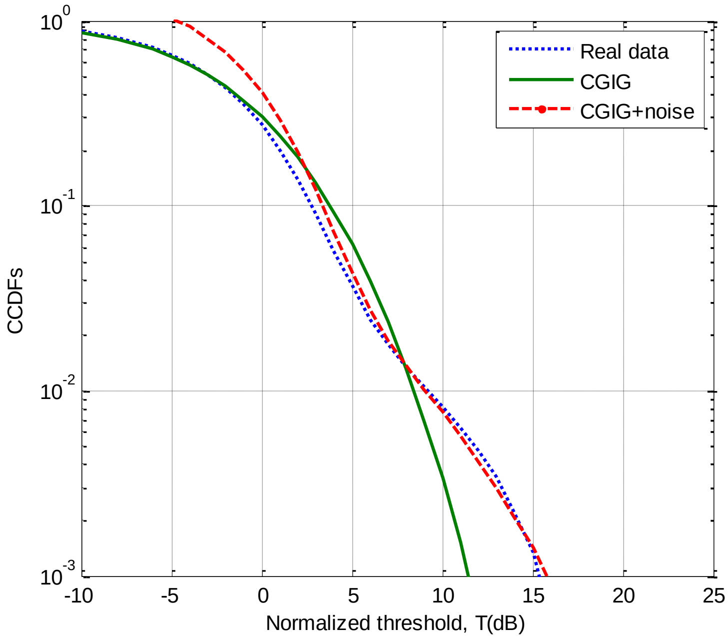

(d)

Figure III. 11: Modeling performance of CGIG models with and without noise using CMLE method and IPIX data for a cell resolution of 3m, N = 1 and M = 60000
(a) Fitted PDFs for VV polarisation and 17th cell range.
(b) Fitted CCDFs for VV polarisation and 17th cell range.
(c) Fitted PDFs for HH polarisation and 6th cell range.
(d) Fitted CCDFs for HH polarisation and 6th cell range.

For comparison purposes, we conduct bias of estimation of the proposed approaches as shown in Table III. 3. For instance, we simulate CGIG clutter plus noise data for λ = 0.1, 0.5 and 1 (spiky clutter situations), M = 1000, N = 10 and three values of CNR (-3, 0 and 5dB). By investigating the obtained results, we emphasize that the CMLE method provides the best bias values of λ, μ, p_n and CNR . As far as real-time applications are crucial, the time requirements of each estimator should be a challenging factor. Simulated data with CNR = 0dB, M = 1000 and different values of λ are considered using a PC with 'Intel®Pentium®, CPU G645@2.90GHzand 1.89GO of RAM'.

Table III. 3: Bias of estimation of HOME, CNIOME and CMLE approaches for CGIG clutter plus noise parameters with M = 1000, N = 10 and n = 100 trials

	True values				Bias of estimation			
Methods	λ	CNR (dB)	μ	p_n	$E[\hat{\lambda}-\lambda]$	$E[\hat{\mu}-\mu]$	$E[\hat{p}_n-p_n]$	$E[\hat{CNR}-CNR]$
HOME	0.1	-3	0.3339	0.6661	0.0942	-0.0527	0.0546	0.1497
CNIOME					0.0277	-0.0104	0.0123	0.0295
CMLE					0.0145	-0.0015	0.0033	0.0069
HOME	0.5				0.9566	-0.0549	0.0557	0.1688
CNIOME					0.0538	0.0073	-0.0066	-0.0045
CMLE					0.0391	0.0114	-0.0107	-0.0130
HOME	1				242.3712	-0.2026	0.2045	-0.1602
CNIOME					-0.2793	0.0474	-0.0455	-0.0884
CMLE					-0.2629	0.0456	-0.0437	-0.0848
HOME	0.1	0	0.5	0.5	0.1523	-0.1265	0.1209	0.9709
CNIOME					0.0344	-0.0276	0.0220	0.1266
CMLE					0.0186	-0.0139	0.0083	0.0506
HOME	0.5				0.3018	-0.0596	0.0580	0.4708
CNIOME					0.0482	-0.0088	0.0072	0.0574
CMLE					0.0073	0.0006	-0.0021	0.0070
HOME	1				0.9847	-0.0658	0.0637	1.2694
CNIOME					-0.1514	0.0356	-0.0377	-0.1234
CMLE					-0.1328	0.0311	-0.0331	-0.1066
HOME	0.1	5	0.7597	0.2403	0.1527	-0.1754	0.1809	22.5781
CNIOME					-0.0598	0.4531	-0.4477	-2.0065
CMLE					0.0137	0.0007	0.0047	0.0794
HOME	0.5				0.3122	-0.0838	0.0836	1.8136
CNIOME					0.0643	-0.0134	0.0133	0.5201
CMLE					0.0394	-0.0073	0.0072	0.2890
HOME	1				0.6974	-0.0919	0.0929	-0.7997
CNIOME					-0.0695	0.0288	-0.0279	-0.3829
CMLE					-0.0441	0.0223	-0.0214	-0.2374

As shown in Table III. 4, compared to the CNIOME and CMLE approaches, the HOME method which is given in a closed-form with no special functions, achieves a better calculation time. The latter is useful for high sample sizes, but in the case of limited amounts of data, the CNIOME with acceptable calculation time can be applied. Finally, a small chart is presented in Table III. 5 summarizing relative performances of underlying estimators. Time requirements of HOME and CNIOME based approaches are much lower than the CMLE method. To sum up and according to the estimation results given here, the method of moments is certainly chosen for known *CNR* with $M \geq 1000$ particularly when it comes to applications where both efficiency and fast processing time are required. In the case of unknown *CNR*, the CNIOME approach is well suited in real time applications with approximated results as for the CMLE method. Estimation outcomes show that the CMLE constitutes the best choice if accuracy is necessary.

Table III. 4: Average Time consuming in seconds of HOME, CNIOME and CMLE methods for *CNR*=0dB, *M*=1000 and *n*=100 trials

λ	**HOME**	**CNIOME (*r*=0.1)**	**CMLE**
0.1	4.6875e-4	0.0023	2.8767
0.5	1.5625e-4	0.0034	3.4462
1.0	9.3750e-4	0.0028	2.4095
1.5	3.1250e-4	0.0037	2.3895

Table III.5: Relative performances in terms of MSE of HOME, CNIOME and CMLE methods for CGIG clutter plus noise parameters

Operating conditions	**HOME**	**CNIOME**	**CMLE**
Low sample size	poor	good	acceptable
High sample size	good	moderate	acceptable
Low *CNR*	poor	acceptable	good
High *CNR*	moderate	good	acceptable
Low shape parameter	moderate	acceptable	good
High shape parameter	poor	good	acceptable
Time-consuming	low	moderate	high
Complexity in real time applications	good	acceptable	poor

III. 6 Conclusion

For single and multilook data, three estimators based on integer order moments, non-integer order moments and ML were derived for CGIG clutter plus noise parameters. These methods are referred to as HOME, CNIOME and CMLE approaches. The HOME method was given in closed-forms for both known and unknown *CNR*. Analytic expressions of the CNIOME and the CMLE are difficult to obtain and hence were calculated using Legendre and Laguerre polynomials of Gauss quadrature integration method to achieve the estimates of the CGIG clutter plus noise parameters. In the case of known *CNR*, simulations results showed that the method of moments and the CMLE method can produce the same estimates of the shape parameter at high sample sizes. For unknown *CNR*, both the CNIOME and CMLE methods present approximate results. In this situation, the HOME exhibits poor estimation results for all values of the shape parameter. Finally, when the number of integrated pulses and *CNR* are high, the CMLE method outperforms always the CNIOME and the HOME methods. IPIX real data were used to show the applicability of estimators of CGIG clutter plus noise model parameters.

4

Radar CFAR Detection in Weibull Clutter based on zlog (z) Estimator

Chapter outline:

IV.1 Introduction

In radar detection, many types of sea and land clutter distributions have been proposed [23]. The Weibull, Log-normal, *K* and GP pdf are good examples describing high resolution radar echoes [23, 14, 32, 33]. Parameter estimation is required in many radar and sonar signal processing procedures. Specifically, numerous CFAR algorithms can not be constructed without parameter estimation of the clutter which is referred to as 'clutter level/power estimation'. In this context, the purpose is to decide whether or not a target is present in a clutter environment so that maximizing the P_{D} and maintaining the P_{FA} are desired. Methods based on non-integer order moments and log-moments have already been applied to solve the estimation problem of compound Gaussian distributed parameters [14]. These techniques named NIOME and zlog(z) were proposed to avoid numerical calculation with considerable computing requirements associated to the MLE approach. On the other hand, CFAR schemes are usually designed for targets embedded in homogeneous and heterogonous environments which are caused by the presence of clutter edge and/or interfering targets (outliers). In each situation, the CFAR algorithm has a specific formula in terms of samples for the evaluation of the background level from the data [32]. To this effect, several CFAR detectors operating in homogeneous CA-CFAR and ML-CFAR [32, 68] and heterogeneous environment (OS-CFAR, SO-CFAR, GO-CFAR and CMLD-CFAR [34, 69] were developed. In the case of Weibull clutter, WH-CFAR, logt-CFAR, ML-CFAR, CML-CFAR detectors have been suggested in the past [32, 33, 34, 68, 69]. It has been demonstrated that the CFAR loss is related to the variance of the estimated parameters. To reduce the CFAR loss, the ML-CFAR detection is developed and has more computational-intensive than the others [32].

The objective of this chapter is the use of modified estimation method based on log-moments that provide rapid calculation of CFAR detection in Weibull clutter with unknown parameters. To this end, the zlog(z) method is developed in terms of the digamma function whereas the estimates of the shape parameter are given by the interpolation method [73]. The NIOME approach is also given and matches the zlog(z) estimation results for low fractional order values. Via Monte-Carlo simulations, it is shown that the CFAR detection performances based on the zlog(z) estimator have approximately the same results than the existing ML-CFAR detector, but with low time-consuming which is essential in real time applications.

This chapter is organized as follow. Section IV.2 presents different steps for the construction of the MLE, zlog(z) and NIOME based estimators of Weibull clutter parameters. Section IV.3 describes the ML-CFAR and logt-CFAR detectors with unknown parameters of the Weibull distribution and proposes the CFAR detection based on zlog(z) estimator. Section IV.4 illustrates estimation and detection comparisons of logt-CFAR, ML-CFAR and zlog(z) CFAR algorithms. Finally, some conclusions are drawn in Section IV.5.

IV.2 Parameter estimation

The Weibull distribution is known as the generalized compound model and can be inspired from the generalized *K* pdf with particular values of the speckle and the texture components parameters [17]. The pdf of Weibull clutter is given by [32, 17]

$$p(x) = \frac{c}{b}\left(\frac{x}{b}\right)^{c-1} \exp\left(-\left(\frac{x}{b}\right)^{c}\right) \tag{IV. 1}$$

where b is the scale parameter and c is the shape parameter. Below, estimators based on the MLE, zlog(z) and NIOME approaches are presented under the assumption of M iid Weibull samples, $x_1, x_2, \ldots, x_M$.

IV.2. 1 MLE method

This procedure is obtained after the calculation of partial derivatives with respect to b and c of the log-likelihood function and let them equal to zeros. Using the MLE method, the estimates of b and c denoted by $\hat{b}$ and $\hat{c}$ are given by [32]

$$\begin{cases} \dfrac{\sum_{i=1}^{M} (x_i)^{\hat{c}} \ln x_i}{\sum_{i=1}^{M} x_i^{\hat{c}}} - \dfrac{1}{M} \sum_{i=1}^{M} \ln x_i = \dfrac{1}{\hat{c}} \\ \hat{b} = \left(\dfrac{1}{M} \sum_{i=1}^{M} (x_i)^{\hat{c}} \right)^{\frac{1}{\hat{c}}} \end{cases} \tag{IV. 2}$$

Note that, $\hat{c}$ can not be obtained straightforwardly in which iterative methods are required.

IV.2. 2 Proposed zlog(z) method

This technique is based on the evaluation of log-moments from the data. To do this, we start by giving the expression of moment of order r

$$\langle x^r \rangle = \int_0^\infty x^r p(x) dx = b^r \Gamma\left(1 + \frac{r}{c}\right) \tag{IV. 3}$$

Using the fact that $\dfrac{\mathrm{d}\Gamma(x)}{\mathrm{d}x} = \Gamma(x)\psi(x)$ [64], the derivative of (IV. 3) with respect to r is

$$\begin{aligned} \frac{d\langle x^r \rangle}{dr} &= \langle x^r \ln x \rangle \\ &= \frac{db^r}{dr} \Gamma\left(1 + \frac{r}{c}\right) + b^r \frac{d\Gamma\left(1 + \frac{r}{c}\right)}{dr} \\ &= b^r \ln(b) \Gamma\left(1 + \frac{r}{c}\right) + b^r \frac{1}{c} \Gamma\left(1 + \frac{r}{c}\right) \psi\left(1 + \frac{r}{c}\right) \end{aligned} \tag{IV. 4}$$

where $\psi(.)$ is the Psi function [64]. For r=0, (IV.4) becomes

$$\langle \ln x \rangle = \log b + \frac{1}{c}\psi(1) \tag{IV. 5}$$

For *r*=1, (IV. 4) will be

$$\langle x \ln x \rangle = b \log b \Gamma\left(1+\frac{1}{c}\right) + b\frac{1}{c}\Gamma\left(1+\frac{1}{c}\right)\psi\left(1+\frac{1}{c}\right) \tag{IV. 6}$$

Combining (IV. 5) and (IV. 6) with $\langle x \rangle = b\Gamma(1+1/c)$ and using the recurrence formula $\psi(x+1) = \psi(x) + 1/x$, the zlog(z) based estimator is finally yields the following formula [73]

$$\frac{\langle x \ln x \rangle}{\langle x \rangle} - \langle \ln x \rangle - 1 = \frac{1}{\hat{c}}\left(\psi(1/\hat{c}) - \psi(1)\right) \tag{IV. 7}$$

where $\psi(1) = 0.57721566490153$ and the left hand side of (IV.7) is calculated from the data.

IV.2. 3 Proposed NIOME method

This approach is also constructed when non-integer order moments given by (IV. 3) are used. In order to eliminate the scale parameter *b*, the statistical ratio $\langle x^{r+1} \rangle / \langle x^r \rangle \langle x \rangle$ is considered. Hence [73]

$$\frac{\langle x^{r+1} \rangle}{\langle x^r \rangle \langle x \rangle} = \frac{\Gamma\left(1+\frac{r+1}{\hat{c}}\right)}{\Gamma\left(1+\frac{r}{\hat{c}}\right)\Gamma\left(1+\frac{1}{\hat{c}}\right)} \tag{IV. 8}$$

when $r \to 0$, it shown in (Mezache et al. 2017; Sahed and Mezache 2017) that the NIOME method provides similar results best than the zlog(z) method. From Figure IV.1, it is observed that the right hand sides of (IV. 7) and (IV. 8) are monotonic functions where the look-up table or the interpolation method can be applied instead of numerical routines as the case of the MLE method. This is crucial in real time applications especially when CFAR target detection is considered. After the evaluation of $\hat{c}$ using (IV. 7) or (IV. 8), *b* is simply estimated by using either the first order moment or the ML method.

$$\hat{b} = \frac{\frac{1}{M}\sum_{i=1}^{M} x_i}{\Gamma(1+1/\hat{c})} \text{ or } \hat{b} = \left(\frac{1}{M}\sum_{i=1}^{M} x_i^{\hat{c}}\right)^{1/\hat{c}} \tag{IV. 9}$$

Equations (IV. 7) and (IV. 8) are derived in terms of Psi and gamma functions respectively. Recurrence relations of these functions with fractional variables (i.e., 1/c, r/c and (r+1)/c) are not available. Thus, the well known recurrence relations, $\psi(x+1)=\frac{1}{x}+\psi(x)$ and $\Gamma(x+1)=x\Gamma(x)$ can not be applied.

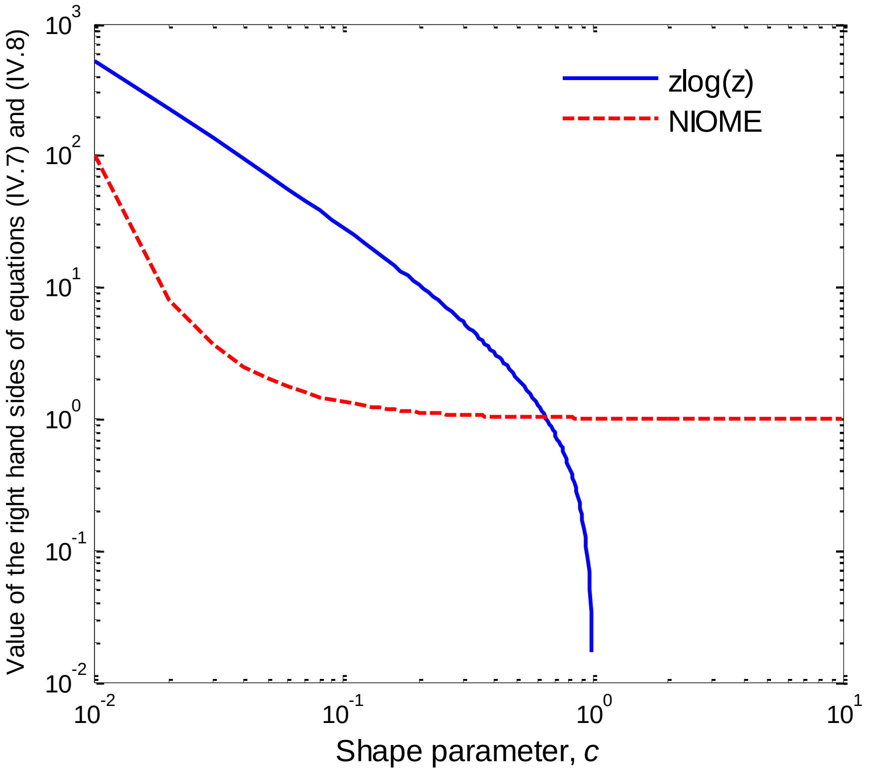

Figure IV.1: Monotonic characteristics of zlog(z) and NIOME based estimators.

IV.3 CFAR detection

Radar target detection is usually modeled by binary hypothesis test. The observed signal under the two hypotheses, H_1 for target present and H_0 for target absent (clutter only), is given by [29]

$$\begin{cases} \mathrm{H}_1 : \ y = s + c \\ \mathrm{H}_0 : \ y = \quad \mathrm{c} \end{cases} \qquad \text{(IV. 10)}$$

where y, s and c are complex numbers and the received envelop is modeled by

$$x = \begin{cases} \mathrm{H}_1 : y = \sqrt{|s|^2 + |c|^2 + 2|s||c|\cos\varphi} \\ \mathrm{H}_0 : y = |\mathrm{c}| \end{cases} \tag{IV. 11}$$

where φ has a uniform distribution between 0 and 2π. As mentioned above, compound Gaussian models are well adapted for sea radar clutter [23, 70]. Unfortunately, it is difficult to obtain appropriate decision rules with CFAR behavior due to the mathematical complexity. Recently, Weinberg used in [70] the Bayesian approach for the development of a new test statistic in the presence of Pareto type II clutter with unknown parameters. In [32], the ML-CFAR detector for the Weibull background has been derived and its performance has been obtained. In this case, the adaptive detection threshold, *T* for the ML-CFAR algorithm with unknown parameters as shown in Figure IV.2, is expressed by

$$T = \hat{b}\alpha^{1/\hat{c}} \tag{IV. 12}$$

where α is the threshold multiplier used to change the desired value of the P_{FA}, $\hat{b}$ and $\hat{c}$ are computed from the data coming from *M* range cells (clutter samples) adjacent to the CUT. In the case of known shape parameter, a closed-form expression of the P_{FA} is obtained [32].

$$P_{\mathrm{FA}} = \left(1 + \frac{\alpha^c}{M}\right)^{-M} \tag{IV. 13}$$

when both *b* and, *c* are unknown, they need to be estimated simultaneously using (IV. 2). The threshold described in Figure IV.2, is indeed CFAR, but we could not find an analytic formula for the relationship between α and P_{FA}. Therefore, the results will be expressed in graphs obtained by Monte-Carlo simulations. The target is declared if the content of the CUT is greater than *T* value. On the other hand, the detection threshold related to the logt-CFAR algorithm in presence of Weibull clutter is given in terms of the mean ($\hat{\mu}$) and the standard deviation ($\hat{\sigma}$) of the random variables, $z_i = \ln x_i$, $i = 1, 2\ldots, M$ [33].

$$T = \hat{\mu} + \alpha\hat{\sigma} \tag{IV. 14}$$

In this case, analytic expressions of P_{FA} and P_{D} are also difficult to obtain. Compared to the logt-CFAR and WH-CFAR algorithms, it has been discussed that the ML-CFAR detector provides a low-loss CFAR with considerable calculation time [32]. In the following, the zlog(z) estimator is used in Figure IV.2 as an alternative of the MLE approach for the evaluation of $\hat{b}$ and $\hat{c}$ which provides a low computation time.

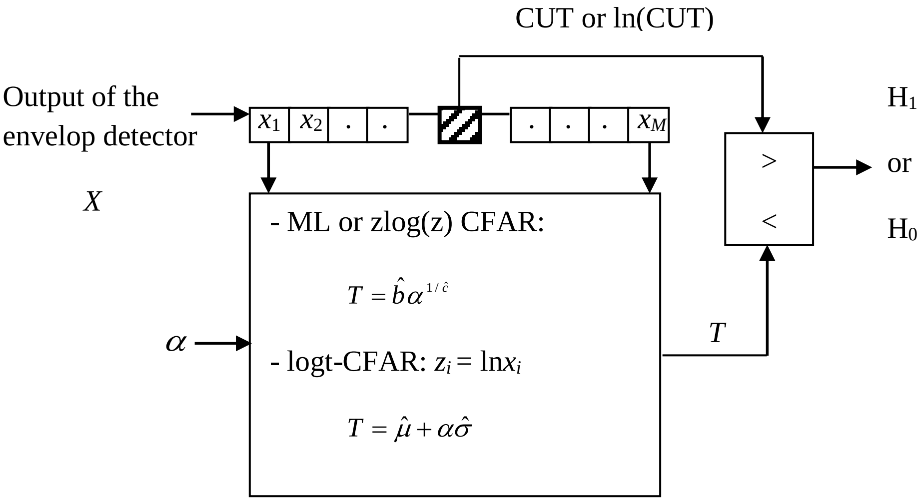

Figure IV.2: CFAR detectors in Weibull clutter with unknown parameters for homogenous environment

IV.4 Detection results

In this section, we carry out some Monte-Carlo simulations in order to compare the proposed zlog(z) CFAR detection results with those obtained by the existing logt-CFAR and ML-CFAR algorithms. First, the estimation accuracy of methods evoked in Section IV. 3 performed by the mean square error of estimation (MSE) and bias of estimation is compared for values of the shape parameter, $c \in [0.5\ 2]$. Besides, simulations are given in terms of M = 16, 24 and 32 samples, the scale parameter $b = \Gamma(1+2/c)^{-1/2}$ (i.e., clutter power is normalized to 1) and n=1000 trials. Figures IV. 3 , a-b depict MSE and bias curves against true values of the shape parameter for M = 16, 24 and 32. It is observed that when c is around 0.5, the MLE approach exhibits the best results. For other values of c, we notice that the zlog(z) and NIOME methods remain slightly better. In general, the estimates of the shape parameter are very close using the three estimation approaches. Furthermore, for a small value of the non-integer order (r = 0.01), curves obtained by the proposed estimation methods are almost overlap. As radar target detection is accomplished in real-time processing, the consuming-times of estimators are compared. To do this, we simulate Weibull samples for c = 0.5, b = 0.2041 and M = 32 using a PC with ‘Intel®Pentium®, CPU G645@2.90GHz and

4GO of RAM. The calculation time values in seconds of the MLE, zlog(z) and NIOME are averaged over n=1000 trials to be 0.0026 s, 0.0005 s and 0.0004 s respectively. These improvements in computational requirements of the proposed approaches are due to the use of the interpolation technique (look-up table method).

It is now of interest to examine the performance of the new zlog(z) CFAR detector relative to that of logt-CFAR and ML-CFAR procedures. In order to compute the scale factor α for any values of b and c, Figure IV.4 .a, illustrates P_{FA} values of each CFAR detector for M = 32 samples. Obviously, the CFAR property is remarkable by the similarity of different curves. Partial enlargement of P_{FA} curves is highlighted in Figure IV. 4 . b. For consistency, the desired value of the P_{FA} is set to 10^{-3} throughout, with $\alpha = 3.616$ dB, $\alpha = 9.843$ dB and $\alpha = 10$ dB corresponding to the logt-CFAR, ML-CFAR and zlog(z) CFAR respectively. The detection performance comparisons are presented in Figure IV.5 .a, for M=32 and two different values of c = 0.5 and c = 2. The target signal is generated from Swerling I model. It is clear that the ML-CFAR and the zlog(z) CFAR provide the best results for both spiky and Gaussian clutter situations. In addition, the zlog(z) CFAR detector exhibits a lower calculation time which is important in real-time processing.

To provide the CFAR detector with immunity against interfering targets, we resort Weibull clutter amplitudes in an increasing order and then the highest M-k samples are censored where k is the ranked order. The modified ML estimators of b and c for the censored case are given in [32, 71]. As noted in Section IV. 2, the proposed zlog(z) estimator is derived for iid Weibull samples. In order to show the performance degradation of ML-CFAR and zlog(z) CFAR detectors against interfering targets and clutter edge situations, Figure IV.5 ,b shows P_{FA} curves versus the scale factor α for two interfering targets inserted in leading and lagging windows with ICR = 0 dB (Interfering-to-Clutter Ratio) and ICR = 10 dB. The clutter transition is also tested with CCR = 0dB (Clutter-to-Clutter Ratio) which is injected for instance from 18th cell to 32nd cell. It is noticed that the P_{FA} is not maintained due the estimation errors of c and b. As shown in Table IV. 1, the scale factor α related to each CFAR detector is not maintained for P_{FA} = 10^{-3} and decreasing of the P_D values is another observation in presence of non homogeneous clutter.

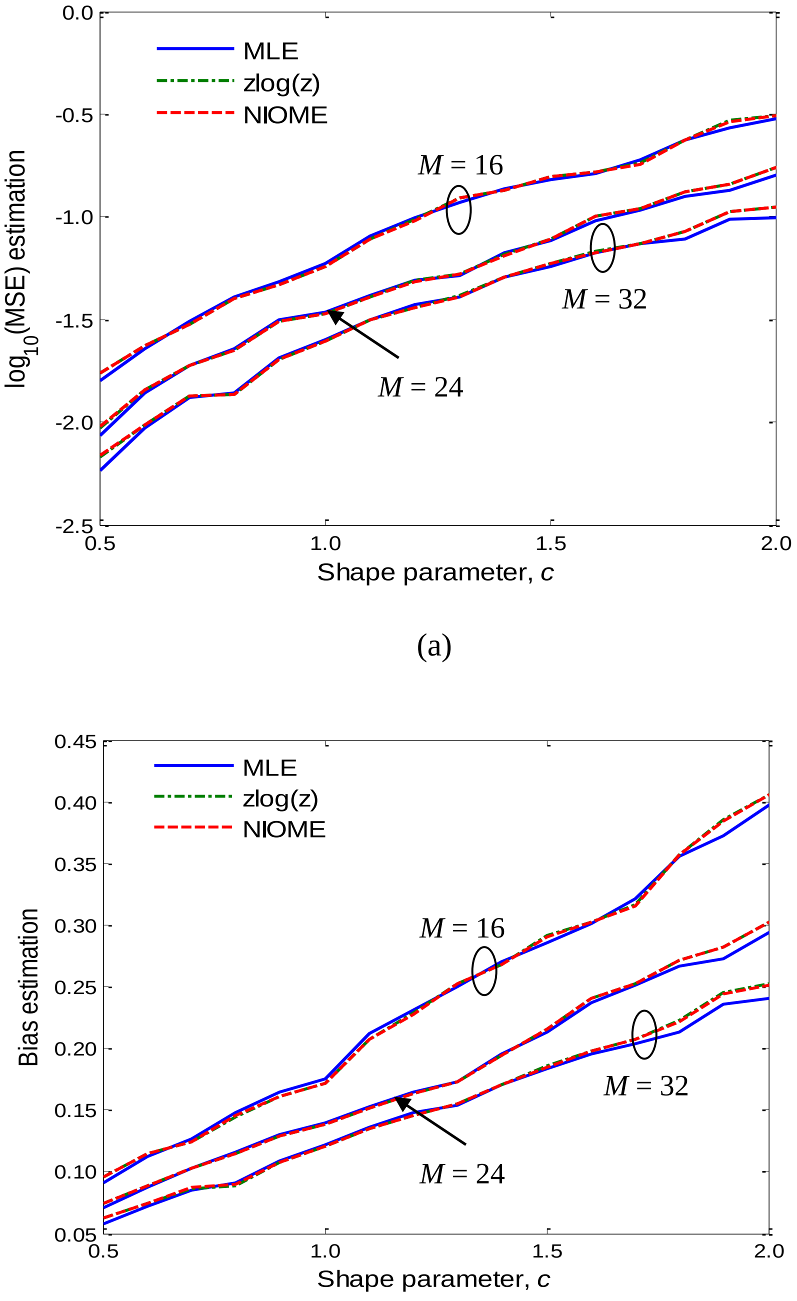

(a)

(b)

Figure IV.3: Estimation performances of the shape parameter, c using MLE, zlog(z) and NIOME (r = 0.01) methods.

(a) MSE of estimates, $E[(c-\hat{c})^2]$; (b) Bias of estimates, $E[|c-\hat{c}|]$.

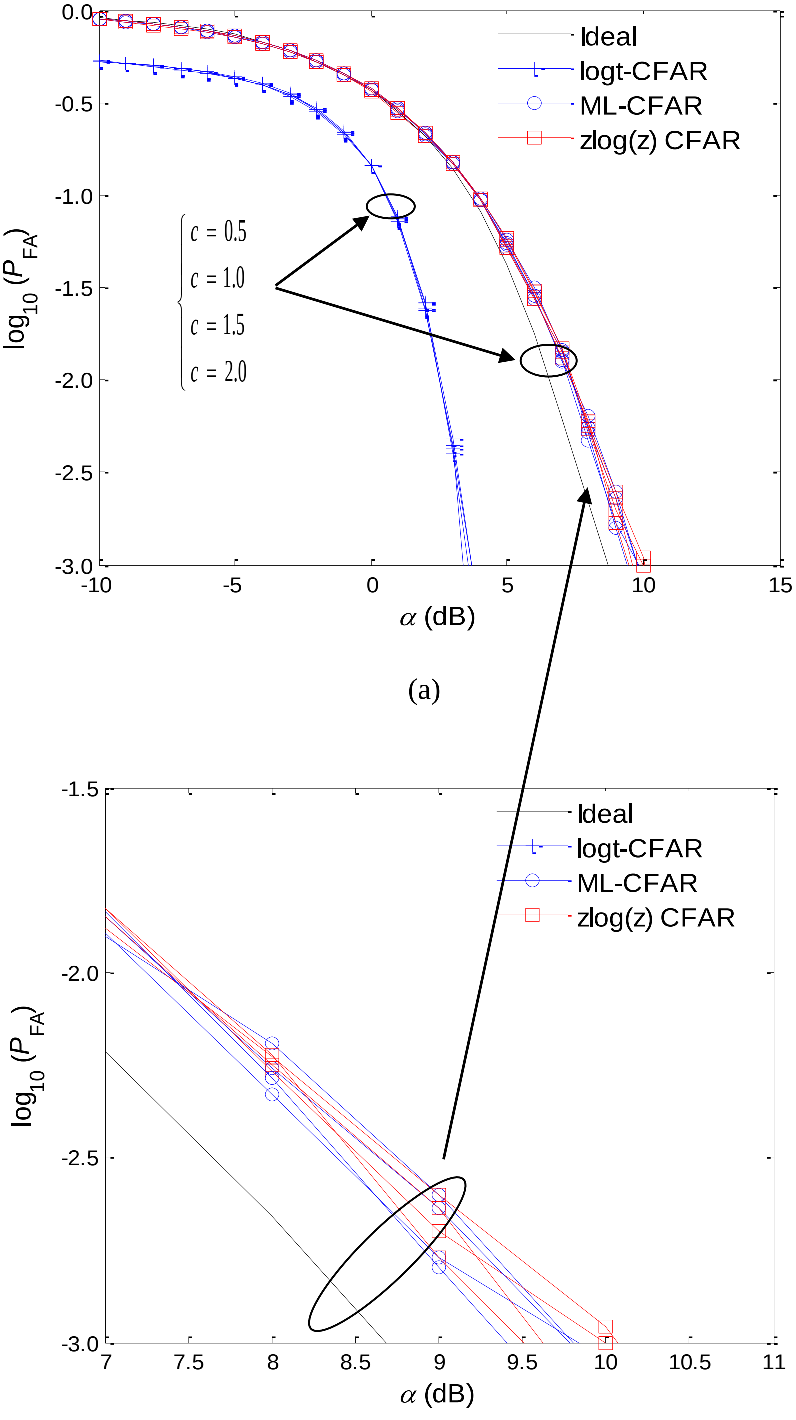

(a)

(b)

Figure IV.4: CFAR property of logt-CFAR, ML-CFAR and zlog(z) CFAR algorithms in terms of *c* with $M = 32$.

(a) Full CFAR property; (b) Partial enlargement of P_{FA} curves.

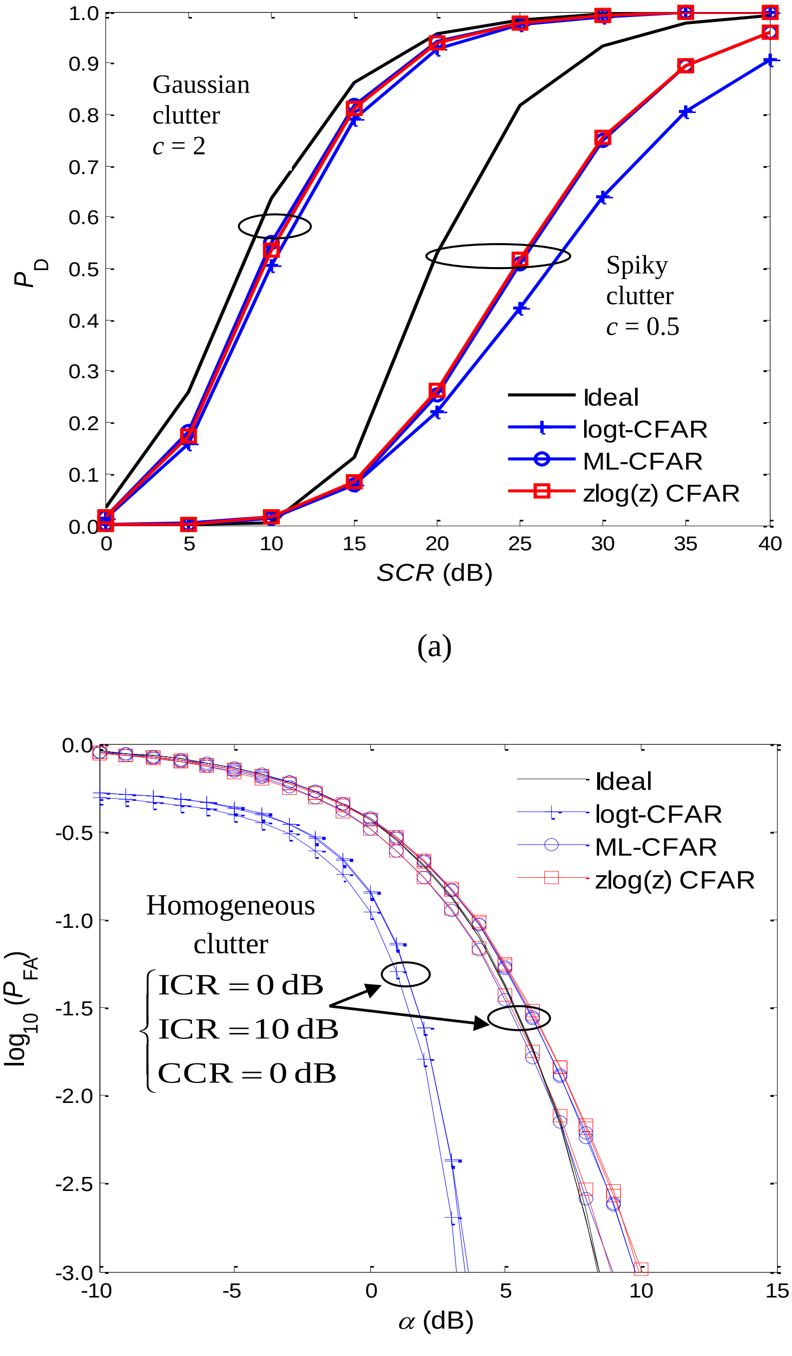

(a)

(b)

Figure IV.5: Detection performances of logt-CFAR, ML-CFAR and zlog(z) CFAR algorithms for $M = 32$ and $P_{FA} = 10^{-3}$.

(a) P_D versus SCR (homogeneous clutter); (b) P_{FA} versus α (heterogeneous clutter) with c=0.5.

Table IV.1: Performance indicator of CFAR detectors for homogeneous and heterogeneous Weibull clutter with $P_{FA} = 10^{-3}$, ICR = 0dB, ICR = 10 dB and CCR = 0 dB

Environment	Detection performance	Ideal detector	logt-CFAR detector	ML-CFAR detector	zlog(z) CFAR detector
Homogeneous	P_D	0.813	0.423	0.502	0.509
	α (dB)	8.350	3.616	9.843	10.000
Heterogeneous (2 interfering targets)	P_D	0.813	0.318	0.369	0.387
	α (dB)	8.350	3.300	9.000	9.000
Heterogeneous (clutter edge)	P_D	0.813	0.421	0.508	0.517
	α (dB)	8.250	3.549	9.130	9.250

IV.5 Conclusion

In this chapter, two estimation techniques named zlog(z) and NIOME have been proposed to estimate the parameters of the Weibull distribution. The proposed estimates were computed by the interpolation method. On the basis of Monte-Carlo simulations, the derived estimators provide almost the same results, but with low-computational requirements compared to the MLE approach. CFAR detection of Swerling I targets has been analyzed using the ML-CFAR, zlog(z) CFAR and logt-CFAR algorithms. The detection results showed the degradation of logt-CFAR detector and the similarity of the ML-CFAR and the zlog(z) CFAR. The above results confirm that the latter is undoubtedly preferred in real-time applications for homogeneous Weibull clutter.

Conclusions

1. Conclusion

Contributions presented in this thesis are essentially delaying with radar sea-clutter modeling using mixtures of compound Gaussian distributions, parameter estimation of CGIG clutter model plus thermal noise and CFAR detection in homogeneous weibull clutter using an alternative approach based upon zlog (z) estimator.

Firstly, main components of monostatic radar were presented firstly. Then, different statistical models describing surface and volume radar clutter were cited. Targets fluctuating models are also given using Rayleigh and non-Rayleigh distributions. In addition, decision theory was introduced by means of three conventional decision rules like Bayes, Minimax and Neyman-Pearson criteria. Finally, related CFAR detection algorithms that are usually used in homogeneous and heterogeneous environments are discussed and described for a Gaussian clutter at the end of this chapter.

Then, the modeling of high resolution sea clutter has been discussed and the mixture distribution with different random textures has been proposed. as well as, the additive thermal noise was incorporated to provide an appropriate model for real sea clutter statistics collected by IPIX, X-band radar. The proposed models are based on the sum/mixture of two different compound Gaussian distributions with thermal noise. For this, the CGIG the *K* and the Pareto plus noise distributions were combined to achieve goodness of fit to real data. The least squares method based on the N-M algorithm was used to estimate the parameters of underling mixture models. Experimental results showed that the proposed models achieve the best tail fitting in most cases compared with the standard *K* plus noise, Pareto plus noise and KK plus noise models.

After that, three estimators based on integer order moments, non-integer order moments and ML were derived for CGIG clutter plus noise parameters. For single and multilook data, these methods are labeled HOME, CNIOME and CMLE approaches. as well, The HOME method was given in a closed-form for both known and unknown CNR. Compact expressions of the CNIOME and the CMLE are difficult to obtain where Legendre and Laguerre polynomials of Gauss quadrature integration method were executed to achieve the estimates of the CGIG clutter plus noise parameters. In the case of known CNR, simulations results showed that the method of moments and the CMLE method can produce the same estimates of the shape parameter at high sample sizes. For unknown CNR, both the CNIOME and CMLE methods present approximate results. In this situation, the HOME exhibits poor estimation results for all values of the shape parameter. When the number of integrated pulses and CNR are high, the CMLE method performs always the CNIOME and the HOME methods. IPIX real data were also considered to show the effectiveness of CGIG clutter plus noise model. In most cases, the CMLE approach is accurate, but relatively slow due to the calculation of the numerical integration of log likelihood functions.

Finally, two alternative estimation techniques named zlog(z) and NIOME have been proposed to estimate the parameters of the Weibull distribution. The proposed estimates were computed by the interpolation method. Under Monte-Carlo simulations, the derived estimators provide almost the same results, but with low-computational requirements compared to the MLE approach. CFAR detection of Swerling I targets have been analyzed using the ML-CFAR, zlog(z) CFAR and logt-CFAR algorithms. Via simulated data, it is shown that the CFAR detection performances based on the zlog(z) estimator have almost similar results better than the existing maximum likelihood (ML) CFAR detector, but with low time-consuming which is very important in real time applications.

2. Suggestions

During research progresses, some interesting suggestions and extensions of this dissertation can be outlined as follows for the future:

- In order to obtain the best fit to empirical data in the majority of cases, it is desired to use a compound Gaussian model with a new texture component. Also, a model selection technique should be used to switch between statistical models.
- Numerical estimation methods may cause errors of parameter estimates with high computational requirements and hence estimation performances are sub-optimal. For this, development of closed form estimators of CIG clutter plus noise parameters is crucial.
- From the open literature, CFAR schemes with known shape parameter and scale parameter have been developed for *K* and Pareto type II clutter respectively. It is desired to construct non-coherent CFAR detection in presence of CGIG clutter without noise using for instance the deep learning technique.

References

[1] M. A. Richards, J. A. Scheer, W. A. Holm, "*Principles of Modern Radar*", SciTech Publishing-An Imprint of the IET, USA, 2010.

[2] B. L. Lewis, F. F. Kretschmer, Jr. W. Shelton, "*Aspects of Radar Signal Processing*", Artech Hous, INC, USA, 1986.

[3] D. K. Barton, "*Radar clutter*", Artech .Hous, INC, USA, Vol. 5, 1975.

[4] L. A. Prastitis, "*On adaptive censored CFAR detection*", Phd Thesis, New Jersey Institute of Technology, University of Heights Newark, 1993.

[5] J. B. Billingsley, A. Farina, F. Gini, M. V. Greco , L. Verrazzani, *"Statistical analyses of measured radar ground clutter data",* IEEE Transactions on Aerospace and Electronic Systems, Vol. 35, no. 2, pp. 597-593, 1999.

[6] M. Jahangir, D. Blacknell, R. G. White, *"Accurate approximation to the optimum parameter estimate for K-distributed clutter",* IEE Proc-Radar, Sonar & Navigation, Vol. 143, no. 6, pp. 383-390, 1996.

[7] A. Balleri, A. Nehorai, J. Wang, *"Maximum likelihood estimation for compound-Gaussian clutter with inverse gamma texture",* IEEE Transactions on Aerospace and Electronic Systems, Vol. 43, no. 2, pp. 775-779, 2007.

[8] E. Ollila, D. E. Tyler, V. Koivunen, V. Poor, *"Compound-Gaussian clutter modeling with an Inverse Gaussian texture distribution",* IEEE Transaction. Signal Processing Letters, Vol. 19, no. 12, pp. 876-879, 2012.

[9] A. Mezache, I. Chalabi, F. Soltani, M. Sahed, *"Estimating the Pareto plus noise distribution parameters using non-integer order moments and [zlog (z)] approaches",* IET Radar. Sonar & Navigation, Vol. 10, no. 1, pp. 192-204, 2016.

[10] A. Mezache, M. Sahed, F. Soltani, I. Chalabi, *"Model for non Rayleigh clutter amplitudes using compound inverse Gaussian distribution: an experimental analysis",* IEEE Transactions on Aerospace and Electronic Systems, Vol. 51, no. 1, pp. 142-153, 2015.

[11] L. Rosenberg, D. J. Crisp, N. J. Stacy, "*Analysis of the KK-distribution with medium grazing angle sea-clutter*", IET Radar. Sonar & Navigation, Vol. 4, no. 2, pp. 209-222, 2010.

[12] D. A. Abraham, J. M. Gelb, A. W. Oldag, "*K-Rayleigh mixture model for sparse active sonar clutter*", OCEANS '10 IEEE Conference, 24-27 May 2010, Sydney, NSW.

[13] X. Zhou, R. Peng, C. Wang, "*A Two-Component K–Lognormal mixture model and its parameter estimation method*", IEEE Transaction on Geosciences and Remote Sensing, Vol. 53, no. 5, pp. 2640-2651, 2015.

[14] M. Sahed, A. Mezache, "*Closed-form fractional moments-based estimators for K-distributed clutter plus noise parameters*", IEEE Transactions on Aerospace and Electronic Systems, Vol. 53, no. 4, pp. 2094-2100, 2017.

[15] S. Watts, "*Radar detection prediction in K-distributed sea clutter and thermal noise",* IEEE Transactions on Aerospace and Electronic Systems, Vol. 23, no. 1, pp. 40-45, 1987.

[16] A. Mezache, M. Sahed, F. Soltani, I. Chalabi, "*Estimation of the K-distributed clutter plus thermal noise parameters using higher order and fractional moments*", IEEE Transactions on Aerospace and Electronic Systems, Vol. 51, no. 1, pp. 733-738, 2015.

[17] V. Anastassopoulos, G. A. Lampropoulos, A. Drosopoulos, M. Rey, "*High resolution radar clutter statistics*", IEEE Transactions on Aerospace and Electronic Systems, Vol. 35, no. 1, pp. 43-60, 1999.

[18] C. W. Helstrom, "*Distribution of the sum of clutter and thermal noise*", IEEE Transactions on Aerospace and Electronic Systems, Vol. 36, no. 2, pp. 709-713, 2000.

[19] L. Rosenberg, S. Watts, S. Bocquet, "*Application of the K+Rayleigh distribution to high grazing angle sea-clutter*", IEEE International Radar Conference, 13-17 October 2014, Lille France.

[20] S. Bocquet, "*Parameter estimation for Pareto and K distributed clutter with noise*", IET Radar. Sonar & Navigation, Vol. 9, no. 1, pp. 104-113, 2015.

[21] M. Sahed, A. Mezache, "*Closed-form estimators for the Pareto clutter plus noise parameters based on non-integer positive and negative order moments*", IET Radar. Sonar & Navigation, Vol. 11, no. 2, pp. 359-369, 2017.

[22] A. Mezache, M. Sahed, F. Soltani, I. Chalabi, "*Model for non-Rayleigh clutter amplitudes using compound inverse Gaussian distribution: An experimental analysis*", IEEE Transactions on Aerospace and Electronic Systems, Vol. 51, no. 1, pp. 142-153, 2015.

[23] A. Mezache, A. Bentoumi, M, Sahed, "*Parameter estimation for compound-Gaussian clutter with inverse-Gaussian texture*", IET Radar. Sonar & Navigation, Vol. 11, no. 4, pp. 586-596, 2017.

[24] H. Yu, P. L. Shui, Y. T. Huang, "*Low-order moment-based estimation of shape parameter of CGIG clutter model",* Electronic Letters, Vol. 52, no. 18, pp. 1561-1563, 2016.

[25] P-L. Shui, L. X. Shi, H. Yu, Yu-T. Huang, "*Iterative maximum likelihood and outlier-robust bipercentile estimation of parameters of compound-Gaussian clutter with inverse Gaussian texture*", IEEE Signal Processing Letters, Vol. 23, no. 11, pp. 1572 – 1576, 2016.

[26] H. M. Finn, R. S. Johson, "*Adaptive detection mode with threshold control as a function of spatially sampled clutter estimates*'', RCA Reveiew, Vol. 29, no. 3, pp. 414-464, 1968.

[27] A. Mezache, F. Soltani, "*Threshold optimization of decentralized CFAR detection in Weibull clutter using genetic algorithms*", Signal Image and Video Processing, Springer, Vol. 2, pp. 1-7, 2008.

[28] R. S. Blum, J. Qiao, "*Threshold optimization for distributed order-statistic CFAR signal detection* ", IEEE Transactions on Aerospace and Electronic Systems, Vol. 32, no. 1, pp. 368-377, 1996.

[29] F. Gini, F. Lombardini, "*Decentralized CFAR detection with binary integration in Weibull clutter*", IEEE Transactions on Aerospace and Electronic Systems, Vol. 33, no. 2, pp. 396-407, 1997.

[30] M. Sekine, Y. Mao, "*Weibull Radar Clutter* ", Peter Peregrinus Ltd., London, UK, 1988.

[31] A. Jakubiak, "*False Alarm Probability for a Log-t detector in K-distributed clutter* ", Electronics letters, Vol. 19, no. 18, pp. 725-726, 1983.

[32] R. Ravid, N. Levanon, "*Maximum likelihood CFAR for Weibull background*", IEE Proceedings, Vol. 139, no.3, pp. 256-264, June 1992.

[33] G. B. Goldstein, "*False-alarm regulation in log-normal and Weibull clutter*", IEEE Transactions on Aerospace and Slectronic Systems, Vol. 9, no. 1, pp. 84-92, 1973.

[34] P. Weber, S. Haykin,"*Ordered Statistic CFAR Processing for Two-Parameter Distributions with Variable Skewness*'', IEEE Transactions on Aerospace and Electronic Systems , Vol AES-21, pp. 819-821, 1985.

[35] G. V. Weinberg, L. Bateman and P. Hayden, "*Development of non-coherent CFAR detction processes in Weibull background*", Gigital Signal Processing, Vol. 75,

pp. 96-106, 2018.

[36] A. Gouri, A. Mezache, H. Oudira, A. Bentoumi, "*Mixture of compound-Gaussian distributions for radar sea-clutter modeling* ", Conference on Control Engineering & Information Technology , December 16-18, 2016, Hammamet, Tunisia.

[37] A. Mezache, M. Sahed, T. Laroussi, D. Chicouche, "*Two novel methods for estimating the compound K-clutter parameters in presence of thermal noise*", IET Radar. Sonar & Navigation, Vol. 5, no. 9, pp. 934-942, 2011.

[38] Radar: https://en.wikipedia.org/wiki/Radar.

[39] H. Meiklme, "*Modern Radar Systems*", Artech Hous, Boston, USA, 2001.

[40] B. R. Mahafza, "*Radar Systems Analysis and Design Using MATLAB*", CHAPMAN & HALL/CRC, USA, 2000.

[41] M. Barkat, "*Signal Detection and Estimation*", Artech Hous, 2nd edition, Boston, USA, 2005.

[42] P. P. Gandhi, S. A. Kassam, "*Analysis of CFAR processors in non homogeneous background*", IEEE Transactions on Aerospace and Electronic Systems, Vol. 24, pp. 427-445, 1988.

[43] V. G. Hansen, "Constant false alarm rate processing in search radars", IEE Conference Publication 105, 23rd-25th October 1973, pp. 325-332 Savoy Place, London, England.

[44] V. G. Hansen, J. H. Sawyers , " *Detectability loss due to greatest-of selection in a cell averaging CFAR*", IEEE Transactions on Aerospace and Electronic Systems, Vol. AES-16, pp. 115-118, 1980.

[45] M. Weiss, "*Analysis of some modified cell-averaging processors in multiple target situations*", IEEE Transactions on Aerospace and Electronic Systems, Vol. AES-18, no. 1, pp. 102-114, 1982.

[46] G. V. Trunk, "Radar resolution of targets using automatic detection", IEEE Transaction on Aerospace and Electronic Systems, Vol. AES-14, no. 5, pp. 750-755. 1978.

[47] J. T. Rickard, G. M. Dillard, "*Adaptive detection algorithms for multiple target situations*", IEEE Transactions on Aerospace and Electronic Systems, Vol. AES-13, pp. 338-343, 1977.

[48] H. Rohling, "*Radar CFAR thresholding in clutter and multiple target situations",* IEEE Transactions on Aerospace and Electronic Systems, Vol. AES-19, pp. 608-621,

1983.

[49] A. Mezache, I. Chalabi, T. Laroussi, M. Sahed "*K-clutter plus noise parameter estimation using fractional positive and negative moments*", IEEE Transactions on Aerospace and Electronic Systems, Vol. 52, no. 2, pp. 960-967, 2016.

[50] L. Rosenberg, S. Bocquet , "*The Pareto distribution for high grazing angle sea-clutter*", IEEE Int. Geoscience and Remote Sensing Conference, 21-26 July 2013, Melbourne, Australia

[51] K. D. Ward, RJ. A. Tough, S. Watts, "*Sea Clutter: Scattering, the K-distribution and Radar Performance*", Second Edition IET, London, UK, 2013.

[52] V. Seshadri, "*The Inverse Gaussian Distribution-Statistical Theory and Applications*", Springer-Verlag, New York, USA, 1999.

[53] A. Mezache, A. Gouri, H. Oudira, "*Parameter estimation of CGIG clutter plus noise using constrained NIOME and MLE approaches*", IET Radar. Sonar & Navigation, Vol. 12, no. 2, pp. 176 – 185, 2018.

[54] J. A. Nelder , R. Mead, "*A simplex method for function minimization*", Computer Journal, Vol. 7, no. 4, pp. 308–313, 1965.

[55] A. Ren, Y. Wang, F. Jia, " *A Hybrid estimation of distribution algorithm and Nelder-Mead simplex method for solving a class of nonlinear bilevel programming problems* ", Hindawi Publishing Corporation Journal of Applied Mathematics, Vol. 10, pp.10, 2013.

[56] R. B, Bakker, B. Currie, "*The McMaster IPIX radar sea clutter database*", Online available: http://soma.crl.mcmaster.ca/ipix/

[57] J. C. Lagarias, J. A. Reeds, M. H. Wright, P. E. Wright, "*Convergence properties of the Nelder–Mead simplex method in low dimensions*", SIAM J. Optim, Vol. 9, no. 1, pp. 112–147, 1998.

[58] E. Walter, L. Pronzato, "*Identification of Parametric Models from Experimental Data*", London, Spronger Verlag, UK, 1997.

[59] J. R. Nicholas, "*Estimating the parameters of the K distribution in the intensity domain",* DSTO-TR-0839 Electronics and Surveillance Research Laboratory, pp. 1-76, 1999.

[60] K. J. Sangston, F. Gini, and M. S. Greco, "*Coherent radar target detection in heavy-tailed compound-Gaussian clutter*", IEEE Transactions on Aerospace and Electronic

Systems, Vol. 48, no. 1, pp. 64-77, 2012.

[61] W. H. Press, Teukolsky, W. T. Vetterling, B.P .Flannery, “*Numerical Recipes in Fortran*”, Second Edition Cambridge University Press, 1992.

[62] W. Gautschi, “*Orthogonal polynomials (in Matlab)*”, Journal Computational and Applied. Mathematics, Vol. 178, pp. 215-234, 2005.

[63] J. Spanier, K. B. Oldham, “*An Atlas of Functions*”, Springer-Verlag, New York, USA, 1987.

[64] M. Abramowitz, I. A. Stegun, “*Handbook of Mathematical Functions*”, Dover, New York, 1965.

[65] Numerical Integration:
Online available: http://www.cs.rpi.edu/~flaherje/pdf/fea6.pdf

[66] R. Z. Iqbal, “*Computation of nodes and weights of Gaussian quadrature rule by using Jacobi's method*”, Master thesis, Birmingham University, 2008.

[67] R. John, W. Michael, R. Schucany, W. Haas Roy, “*Generating random variates using transformations with multiple roots*”, American statistician, Vol. 30, no. 2, pp. 88-90, 1976.

[68] M. Miguel Vela, J. A. Besada Portas, and J. R. Casar Corredera ,“*Probability of False Alarm of CA-CFAR Detector in Weibull Clutter*” , Electronics Letters , Vol. 34 , no. 8, pp. 806-807, 1998.

[69] N. Levanon, M. Shor, “*Order Statistics CFAR for Weibull Background*”, IEE Proceedings- F, Vol. 137 , no. 3, pp. 157-162, 1990.

[70] V. G. Weinberg, S. D. Howard, and C. Tran, “*Bayesian Framework for Detector Development in Pareto Distributed Clutter*”, *IET Radar Sonar & Navigation*, Vol. 13, no. 9, pp. 1548-1555, 2019.

[71] H. L. Harter, A. H. Moore, “*Maximum-Likelihood Estimation of the Parameters of Gamma and Weibull Populations from Complete and from Censored Samples*”, Technometrics, Vol. 7, no. 4, pp. 639-643, 1965.

[72] M. Sahed, A. Mezache, T. *Laroussi, “A Novel [z log(z)]-Based Closed Form Approach to Parameter Estimation of K-Distributed Clutter Plus Noise for Radar Detection*”, EEE Transactions on Aerospace and Electronic Systems, Vol. 51, no. 1, pp. 492-505, 2015.

[73] A. Gouri, A. Mezache, H. Oudira, “*Radar CFAR detection in Weibull clutter based on zlog(z) estimator*”, Remote Sensing Letters (Francis & Taylor), Vol. 11, no. 6, pp. 581-589, 2020.

[74] J. Cody, “*An Overview Of Software Development For Special Functions*”, Lecture Notes in Mathematics, 506, Numerical Analysis Dundee, G.A. Watson (ed.), Springer Verlag, Berlin, 1976.